

HEATPIPES

FOR GEOTHERMAL HEAT EXTRACTION



A STUDY ON FILM HEAT TRANSFER IN HEATPIPES

M. Draškić

Heatpipes for geothermal heat extraction

A study on liquid film heat transfer in heatpipes

by

Marko Draškić

to obtain the degree of:

Master of Science
in Mechanical Engineering

at the **Delft University of Technology**

to be publicly defended on Tuesday October 13th, 2020 at 14:00.



Student: M. Draškić
Student number: 4431790
Contact: markodraskic@outlook.com

Dept. doc. nr.: PE-3032

Thesis committee:	dr. R. Delfos (ET)	TU Delft, supervisor
	prof.dr.ir. B.J. Boersma (ET)	TU Delft, supervisor
	dr.ir. R. Pecnik (ET)	TU Delft
	dr.ir. J.W. Haverkort (ET)	TU Delft
	dr. A. Twerda	TNO

An electronic version of this thesis is available at <http://repository.tudelft.nl/>

Abstract

Large quantities of heat stored in geothermal aquifers can be of interest to satisfy above-ground heating demands. With the use of heatpipes, placed into the aquifers, heat may be passively extracted. Vertical two-phase thermosiphons are considered in this study. As a result of a local increase in the saturation temperature in liquid pools, heat can only be transferred in the falling liquid film. The aim of this work is to investigate film heat transfer and its limitations at varying boundary conditions in the evaporator of a vertical experimental setup. An initially homogenized film is studied in a separate film heating section, in which a specific distribution of controlled band heaters and temperature transmitters enables the sensing of local film heat removal behaviour in the heatpipe.

With increasing degrees of wall superheating, the mean film heat removal rate has been found to increase. Locally, beyond some degree of superheating, the heat transfer rate stagnates with increasing Jakob numbers, possibly as a result of film dry-out. As a result of such local behaviour, the slope of the mean heat transfer rate curve decreases with increasing Jakob numbers. The onset of dry-out, characterized by an increase in the intermittency of the results, has been studied by varying the initial liquid flow rate to the heated section. Both the initial film flow rate and the degree of superheating have been found to be of significance for the onset of film dry-out. Film dry-out takes place at flow rates less than some critical flow rate. The local heat removal rate decreases significantly if the initial film flow rate is decreased beyond the critical flow rate. The critical flow rate has been found to increase with increasing rates of superheating. The significance of the saturation temperature on the film heat transfer rate has also been studied in this work. The film heat transfer rate has been found to decrease with decreasing saturation temperature, for all in this study considered degrees of superheating. The steepest decline in heat transfer rates with decreasing saturation temperature is found for the smallest degree of superheating in the analysis. At last, the possibility of film re-distribution following dry-out has been considered. Melamine foam homogenizer rings, inserted in the film flow path, have been found to decrease the degree of film thickness variation in initially inhomogeneous films to some extent. Homogenized films were found to be able to transfer a greater amount of heat than films that had not been re-distributed.

Keywords: *film dry-out, film heat transfer, film homogenization, annular films, geothermal heat extraction, heat pipe limits, experimental thesis*

Acknowledgements

Hereby I would like to express my sincere gratitude to all who have contributed in making this study possible, and without whom I would not have been able to complete this project.

Firstly, I would like to thank my supervisors dr. R. Delfos and dr. B.J. Boersma, whose expertise and insightfulness was invaluable, for providing me with constructive criticism throughout the project. René, thank you for giving me the freedom, a luxury which I first thought was limiting, to pursue my own choices and make mistakes. This freedom eventually provided me with a critical attitude towards any of the paths chosen, steps taken, and results found in this thesis, and with future projects.

Thank you Gerard, Bas, Daniël, Sjaak and most notably Martijn, for providing me with the the practical help and knowledge needed to adjust the experimental setup to my needs. You've shown me that even somebody with two left hands can turn theory into practice with the right tools and help.

Furthermore, I would like to thank dr. A. Twerda and P.S. Omrani of TNO for providing me with much needed additional context on aquifers, and information on other heat transfer device concepts used to extract heat from such aquifers.

I'm grateful to have friends that besides just providing me with the right amount of distractions, have also accompanied me while reading and studying in the past few months. Thank you also for still reaching out to hang out and remind me that I need breaks, even when I forgot to do so myself. In addition, I would like to thank my parents, Radomir and Zorica, for their unconditional and well-needed support. Thank you for always being a listening ear, and for making sure that I had very little to worry about besides studying. At last, I want to thank Lisanne for her endless patience and understanding in the past months, and for continuously putting up with me the countless times that my mind was absent.

Contents

1	Introduction	12
1.1	Background	12
1.2	Two-phase thermosiphon heatpipes	12
1.3	Rationale and structure of study	14
2	Theoretical background	15
2.1	Heat transfer in heatpipe	15
2.1.1	Film condensation	16
2.1.2	Film evaporation	18
2.1.2.1	Nucleate boiling	19
2.1.2.2	Bubble growth & frequency	21
2.1.2.3	Empirical approximations	23
2.1.3	Interfacial shear forces	25
2.1.4	Thermal interfacial resistance	25
2.2	Dry-patches in liquid film	26
2.2.1	Dry-patches in isothermal films	26
2.2.2	Dry-patches in heated films	28
2.2.3	Rewetting	30
2.2.4	Contact angle	30
2.2.4.1	Surface roughness	31
2.2.4.2	Contact angle hysteresis	31
2.2.5	Prevention & mitigation of dry-out	32
2.2.5.1	Increase in film thickness	32
2.2.5.2	Coatings and liners	33
2.2.5.3	Local homogenization	34
2.3	Porous media	34
2.3.1	Darcy's law	34
2.3.2	Flow through unsaturated porous media	35
2.3.2.1	Porous scale flow	35
2.3.2.2	Saturation & capillary pressure	36
2.3.3	Foams	37
2.4	Liquid entrainment & falling films	38
2.4.1	Vertical flow regimes	38
2.4.2	Wave propagation	39
2.4.3	Onset of entrainment	40
2.5	Vapour pressure	41
2.5.1	Viscous limit	41
2.5.2	Sonic limit	42
3	Methodology	43
3.1	Experimental setup	43
3.1.1	Fluid selection	43
3.1.2	Heat flow limits	47
3.1.2.1	Overview of operating limits	47
3.1.2.2	Limits & tube sizing	48
3.1.3	Experimental evaporator	51
3.1.3.1	Heating	51
3.1.3.2	Heater inhomogeneity	51
3.1.3.3	Heater placement & control	53
3.1.3.4	Heater thermocouples	54
3.1.4	Highlighted components	57

3.1.4.1	Experimental condenser	57
3.1.4.2	Insulation	57
3.1.4.3	Tube connectors	60
3.1.4.4	Optical access	60
3.1.4.5	Liquid column height	61
3.1.5	Homogenizer	62
3.2	Setup overview	64
3.3	Measurements	65
3.3.1	Increasing ΔT	65
3.3.2	increasing initial flow rate	65
3.3.3	Increasing saturation temperature	66
3.3.4	Saturation temperature development	66
3.3.5	Heat extraction	66
3.3.6	Homogenizer effectiveness	66
4	Results & Discussion	67
4.1	Increasing ΔT	67
4.2	increasing initial flow rate	72
4.3	Increasing saturation temperature	74
4.4	Saturation temperature development	77
4.5	Heat extraction	78
4.6	Homogenizer effectiveness	80
5	Conclusions	84
6	Recommendations	85
A	Appendix I: Purchased part-list	86
B	Appendix II: Experimental data & Error propagation	87
B.1	Error propagation	87
B.2	Data: Increasing ΔT	88
B.3	Data: increasing initial flow rate	89
B.4	Data: Increasing saturation temperature	91
B.5	Data: Increasing ΔT , excluding homogenizer	93
B.6	Data: Saturation temperature development	93
C	Appendix III: Sensor calibration	95
C.1	Calibration: Thermocouple temperature transmitters	95
C.2	Calibration: Resistance temperature transmitters	95
C.3	Calibration: Flowmeter	98
D	Appendix IV: Heatpipe materials & stress analysis	99
E	Appendix V: Numerical model	101
E.1	Assumptions	101
E.2	Finite difference & governing equations	103
E.3	Boundary conditions	104
E.4	Convective boundary	105
E.4.1	Temperature iteration	105
E.4.2	Heat transfer coefficient iteration	106
E.5	Mesh sizing	107
F	Appendix VI: Auxiliary figures	110

List of Figures

1	Simplified heatpipe schematic.	12
2	Development of pool height h_{pool} , figure shows cross-section of cylindrical heatpipe.	13
3	Increase in saturation temperature with increasing pool depth h_{pool} , fluid data taken from NIST database.[6] Figure includes fluid saturation pressures at top pool interface for $T_{\text{int}} = 70^\circ\text{C}$	14
4	Generalized heatpipe heat transfer resistance scheme.	15
5	Evaporating microlayer at bubble nucleation location. [14].	20
6	Approximation of bubble departure diameter for various saturation temperatures as a function of ΔT for water, as per [18]–[20].	21
7	Bubble trajectory at low liquid mass flux (left), moderate liquid mass flow (middle), large liquid mass flux (right). [24].	23
8	Solid-solid interface schematic.	25
9	Breakup of continuous liquid film, from Genk et al.[35], simplified.	26
10	Required heat flow \dot{Q}_{in} [W] for continuous liquid film, for various inner heatpipe diameters.	27
11	Dependency of $\Delta_{\text{min,ie}}$ and $\gamma_{\text{min,ie}}$ on evaporation parameter ξ	30
12	Liquid droplet on vertical wall, bottom and top interface contact angles at the critical advancing angle θ_a and the critical receding angle θ_r , from [46].	32
13	Theoretical schematic of additional liquid bypass.	33
14	Spatial configurations of fluids f_1 (white) and f_2 (blue), of which f_2 is preferentially attracted to the matrix: (a) absorbed configuration, (b) liquid bridges between individual particles, only in granular media, (c) onset of f_2 mobility, (d) occluded bubble regime, (e) fully saturated configuration.[52].	36
15	Typical curve form relationship capillary pressure- f_2 saturation. Here, f_2 is the preferentially attracted fluid in two-phase porous flow. Taken from [52] and simplified.	37
16	Air/water flow regime map with shaded transition regions, for a vertical pipe, deduced from the results of Weisman et al.[57], [58].	38
17	Propagation of interfacial waves in falling films, as per Park et al.[59].	39
18	Various entrainment mechanisms.[60].	40
19	Figure of merit, maximization of heat transfer coefficient (Nusselt film evaporation).	44
20	Figure of merit, maximization of nucleate boiling heat transfer coefficient as per Shiraiishi [29].	45
21	Figure of merit, maximization of entrainment heat transfer limit.	46
22	Figure of merit, maximization of film boiling heat transfer limit.	46
23	Limit to heat flow, combined from section 3.1.2.1, at various nominal tube sizes for a water-filled heatpipe, using $L_h = 10D_i$. All lines within the shaded area in the figure meet the requirement for the relevant geothermal temperature range.	48
24	Limit to heat flow, combined from section 3.1.2.1, at various nominal tube sizes for an ammonia-filled heatpipe, using $L_h = 10D_i$. All lines within the shaded area in the figure meet the requirement for the relevant geothermal temperature range.	49
25	Limit to heat flow, as found in section 3.1.2.1, for a 2 inch water-filled copper tube, using $L_h = 10D_i$, and $L = 9$ m.	50
26	Limit to heat flow, as found in section 3.1.2.1, for a 2 inch water-filled copper tube, using $L_h = 25$ m, and $L = 2000$ m.	51
27	Schematic view of unfolded band heater. [A4] Heater depicted in grey, cable and cable attachment depicted in black. Heater homogeneity measurements indicated with red dotted lines.	52
28	inhomogeneity measurements for band heaters, along lines indicated in figure 27. For all measurements, $T_{\text{set}} = 50^\circ\text{C}$	53
29	Schematic top view of film section of evaporator. Figure indicates temperature transmitter placement and height x with respect to the top heater, with distance x increasing towards the bottom of the evaporator.	54

30	Approximation of energy balance over unheated section of evaporator wall section during nucleate boiling.	55
31	Temperature decrease of copper evaporator wall with increasing distance from heating element, assuming the Shiraishi[29] nucleate boiling heat transfer coefficient within its applicable range.	56
32	Exploded view of heater and temperature probe assembly, not to scale. Thermal paste depicted in white.	56
33	Cross-sectional view of experimental condenser, not to scale.	57
34	Resistance to heat transfer in insulation, with increasing interior surface temperature.	59
35	Loss of heat heat flow through insulation per unit height of heat pipe, with increasing interior surface temperature.	59
36	Cross-sectional view of tube connector.	60
37	Glass visor assembly bottom of heatpipe, including side bore for transparent bypass.	61
38	Transparent tube with insert, black dotted lines indicative of local shortening of tube in figure.	62
39	Schematic front view of foam suction experiment. Foam blocks are placed on top of a body of water, resting on top of cylindrical pillars. Figure is not to scale.	62
40	Schematic depiction of foam removal during laser cutting, intended cut indicated with dotted line, removed volume indicated in red, laser beam indicated with black arrow. Figure is not to scale.	63
41	Process & instrumentation diagram of experimental setup. The location of figure 33 is indicated in orange. The location of figure 36 is indicated in red. The location of figure 32 is indicated in purple. The location of figure 37 is indicated in green. The location of figure 38 is indicated in blue.	64
42	Heater heat removal rate for film heaters, as a function of the degree of superheating, expressed with the Jakob number ($Ja [-]$). Here, $T_{sat} = 69.1^{\circ}C$ and $\Gamma = 13.3 \cdot 10^{-3} \frac{kg}{ms}$. The gray area indicates the degree of spreading between the greatest ($\dot{Q}_{i,in} + u_{\dot{Q}}$) and the lowest ($\dot{Q}_{i,in} - u_{\dot{Q}}$) film heater output for some value of Ja . Data shown in figure includes 68% ($t_{v,p}=1$) confidence interval.	67
43	Comparison between data shown in figure 42 and the model discussed in Appendix V: Numerical model.	68
44	Comparison between data shown in figure 42 and the expected average heat flow rate for the specified Jakob number.	69
45	Film heater output at decreasing initial liquid film flow rate, for various Jakob numbers. $T_{sat} = 69.1^{\circ}C$, $Ja = 36.5 \cdot 10^{-3}$. The gray area indicates the degree of spreading between the greatest ($\dot{Q}_{i,in} + u_{\dot{Q}}$) and the lowest ($\dot{Q}_{i,in} - u_{\dot{Q}}$) film heater output for some value of Ja . Data shown in figure includes 68% ($t_{v,p}=1$) confidence interval.	72
46	Theoretical minimum wetting rate[35], [40], for heat flow rates of the seemingly homogeneous films of figure 45.	73
47	Film heater output at increasing saturation temperature T_{sat} , for various Jakob numbers. The gray area indicates the degree of spreading between the greatest ($\dot{Q}_{i,in} + u_{\dot{Q}}$) and the lowest ($\dot{Q}_{i,in} - u_{\dot{Q}}$) film heater output for some value of Ja . Data shown in figure includes 68% ($t_{v,p}=1$) confidence interval.	75
48	Evolution of heat transfer coefficient figures of merit, with increasing saturation temperature.	76
49	Heatpipe saturation temperature at varying heat flow rates, for various cooling flow rates. Data shown in figure includes 68% ($t_{v,p}=1$) confidence interval.	77
50	Heatpipe saturation temperature at varying cooling flow rates, for various heat flow rates. Data shown in figure stems from the linear interpolation of the values shown in figure 49.	78
51	Heatpipe heat extraction rate with respect to the evaporator heat flow at varying evaporator heat flow rates, for various cooling flow rates. Data shown in figure includes 68% ($t_{v,p}=1$) confidence interval.	79
52	Modeled evaporator interior wall temperature, at maximum heat throughput.	80

53	Visual comparison of system equipped with- (right) and without (left) homogenizer, for $\Gamma = 7.7 \cdot 10^{-3} \frac{\text{kg}}{\text{ms}}$. The position of a single interfacial wave has been indicated with the red dotted line. The interval between consecutive equidistant lines is 10.1 mm.	81
54	Heater heat removal rate for film heaters, as a function of the degree of superheating, expressed with the Jakob number (Ja [-]), excluding homogenizer. Here, $T_{\text{sat}} = 69.1^\circ\text{C}$ and $\Gamma = 13.3 \cdot 10^{-3} \frac{\text{kg}}{\text{ms}}$. The gray area indicates the degree of spreading between the greatest ($\dot{Q}_{i,\text{in}} + u_{\dot{Q}}$) and the lowest ($\dot{Q}_{i,\text{in}} - u_{\dot{Q}}$) film heater output for some value of Ja. Data shown in figure includes 68% ($t_{v,p}=1$) confidence interval	82
55	Calibration of TT ₀₁ -TT ₀₈ against more accurate thermometer in dry block calibrator for relevant temperature range. The linear fit through the calibration results (found from equation (59)) is shown in orange.	95
56	Calibration of TT _{top} against more accurate thermometer thermometer in dry block calibrator for relevant temperature range. The linear fit through the calibration results (found from equation (61)) is shown in orange.	96
57	Calibration of TT _{sat} against more accurate thermometer thermometer in dry block calibrator for relevant temperature range. The linear fit through the calibration results (found from equation (63)) is shown in orange.	97
58	Calibration of TT _{out} against TT _{in} for relevant temperature range. The linear fit through the calibration results (found from equation (65)) is shown in orange.	98
59	Schematic of numerical model domain, depicting a slice of the heatpipe evaporator. Numerical domain depicted with shaded region evaporator wall.	101
60	Evaporator heat flow at transition to turbulent film flow, as per [11]	102
61	Simplified grid schematic, nodes depicted in white, boundary cells in dark grey, interior cells in light grey.	103
62	Schematic of three distinct boundary configurations. (a) top boundary, imposed heat flux \dot{q} . (b) left boundary, subject to convection with film at $T = T_e$. (c) top left corner, subject to convection with film at $T = T_e$ and imposed heat flux.	104
63	Expression selection for $T_{b,i}$ and $T_{e,i}$ for iteration k	106
64	Expression selection for h_i for iteration k	107
65	Estimated temperature profile at height of heater for various cell heights, $T_{\text{sat}} = 70^\circ\text{C}$, $\dot{q}_h = 1.5 \cdot 10^5 \frac{\text{W}}{\text{m}^2}$	108
66	Evolution of variance in script output with varying mesh coarseness, with $T_{\text{sat}} = 70^\circ\text{C}$, $\dot{q}_h = 1.5 \cdot 10^5 \frac{\text{W}}{\text{m}^2}$ per heater (maximum throughput of experimental setup) and 8 heaters throughout the domain.	108
67	Film heater output at decreasing initial liquid film flow rate, for various Jakob numbers. Data shown in figure includes 68% ($t_{v,p}=1$) confidence interval. Auxiliary figure to figure 45.112	
68	Comparison of heat removal rate for film heaters, as a function of the degree of superheating, expressed with the Jakob number (Ja [-]), in the absence of a homogenizer (left) with a similar set of measurements with a homogenizer (right, figure 42). Auxiliary figure to figure 54.	112

List of Tables

1	Expressions of the figures of merit discussed in section 3.1.1	47
2	Overview of limits to heat transfer heatpipe.	47
3	Overview of (sub)component dimensions of heatpipe assembly.	65
4	General specifications of heatpipe assembly.	65
5	Overview of purchased parts for experimental setup.	86
6	Dataset: Film heater heat removal rate $\dot{Q}_{i,in}$, as a function of the degree of superheating, expressed with the Jakob number (Ja [-]). Experimental set-up includes homogenizer. Data from 301 measurements points.	88
7	Dataset: Film heater heat removal rate $\dot{Q}_{i,in}$ at decreasing initial liquid film flow rate. Experimental set-up includes homogenizer. Data from 241 measurements points.	89
8	Dataset: Film heater heat removal rate $\dot{Q}_{i,in}$ at decreasing initial liquid film flow rate. Experimental set-up includes homogenizer. Data from 241 measurements points.	89
9	Dataset: Film heater heat removal rate $\dot{Q}_{i,in}$ at decreasing initial liquid film flow rate. Experimental set-up includes homogenizer. Data from 241 measurements points.	90
10	Dataset: Film heater heat removal rate $\dot{Q}_{i,in}$ at decreasing initial liquid film flow rate. Experimental set-up includes homogenizer. Data from 241 measurements points.	90
11	Dataset: Film heater heat removal rate $\dot{Q}_{i,in}$ at decreasing initial liquid film flow rate. Experimental set-up includes homogenizer. Data from 241 measurements points.	91
12	Dataset: Film heater heat removal rate $\dot{Q}_{i,in}$ at varying saturation conditions. Experimental set-up includes homogenizer. Data from 181 measurements points.	91
13	Dataset: Film heater heat removal rate $\dot{Q}_{i,in}$ at varying saturation conditions. Experimental set-up includes homogenizer. Data from 181 measurements points.	92
14	Dataset: Film heater heat removal rate $\dot{Q}_{i,in}$ at varying saturation conditions. Experimental set-up includes homogenizer. Data from 181 measurements points.	92
15	Dataset: Film heater heat removal rate $\dot{Q}_{i,in}$, as a function of the degree of superheating, expressed with the Jakob number (Ja [-]). Experimental set-up does not include homogenizer. Data from 241 measurements points.	93
16	Dataset: Variation of saturation conditions and measured heat extraction rate with varying heat flow rate. Experimental set-up includes homogenizer. Data from 181 measurements points.	94

Nomenclature list

Symbol	Property	Units	Symbol	Property	Units
A	Surface area	[m ²]	p	Pressure	[Pa]
A_{cs}	Cross-sectional area of annulus	[m ²]	p_{atm}	Atmospheric pressure	[Pa]
A_e	External heatpipe area	[m ²]	p_{bubble}	Bubble gas pressure	[Pa]
A_h	Interior heater area	[m ²]	p_c	Capillary pressure difference	[Pa]
c	Velocity of sound	[$\frac{m}{s}$]	p_{ce}	Critical external pressure	[Pa]
c_p	Specific heat capacity	[$\frac{J}{kg \cdot K}$]	p_e	Evaporator pressure	[Pa]
D_e	Outer tube diameter	[m]	p_i	Internal tube pressure	[Pa]
D_h	Hydraulic diameter	[m]	p_{∞}	Pressure of surrounding liquid	[Pa]
D_i	Inner tube diameter	[m]	Pr	Prandtl number ($\frac{\nu}{\alpha}$)	[-]
D_n	Nominal tube diameter	[m]	q	Heat flux rate	[$\frac{W}{m^2}$]
E	Young's modulus	[Pa]	q_{fin}	Evaporator heat flux rate	[$\frac{W}{m^2}$]
Eo	Eötvös number ($\frac{(\rho_l - \rho_v)g l_s}{\sigma}$)	[-]	Q	Heat flow rate	[W]
f	Fanning friction factor	[-]	\dot{Q}_{in}	Evaporator heat flow rate	[W]
f_b	Bubble nucleation frequency	[$\frac{1}{s}$]	r	Surface roughness factor	[-]
g	Gravitational acceleration	[$\frac{m}{s^2}$]	r_p	Foam pore radius	[m]
\bar{G}	Modified Re ($(\frac{q_{fin} \delta^*}{h_{fg} \mu_l})^{\frac{5}{4}} (\frac{\rho_l}{\rho_v})$)	[-]	R_c	Nucleation cavity radius	[m]
h	Heat transfer coefficient	[$\frac{W}{m^2 \cdot K}$]	R	Thermal resistance	[$\frac{K}{W}$]
h_{fg}	Enthalpy of vaporization	[$\frac{J}{kg}$]	R_{eq}	Equivalent thermal resistance	[$\frac{K}{W}$]
h_{pool}	Height of liquid pool	[m]	Ra_L	Rayleigh number ($\frac{g \beta (T_a - T_{\infty}) L^3}{\nu_{air} \alpha_{air}}$)	[-]
$h_{pool,0}$	Initial height of liquid pool	[m]	Re_f	Film Reynolds number ($\frac{4 \dot{L}}{\mu_l}$)	[-]
Ja	Jakob number ($\frac{c_{p,l}(T_w - T_{sat})}{h_{fg}}$)	[-]	Re_{tr}	Transitional Reynolds number	[-]
k	Thermal conductivity	[$\frac{W}{m \cdot K}$]	S_f	Phase saturation	[-]
\mathbf{k}	Permeability tensor	[m ²]	S_{ef}	Normalized effective saturation	[-]
$k, (50)$	Specific heat ratio	[-]	t	Cylinder wall thickness	[m]
k_{rf}	Relative permeability coefficient	[-]	t_b	Bubble growth time	[s]
K_{Ic}	Fracture toughness	[Pa · m ^{1/2}]	t_w	Liquid heating time	[s]
L	Heatpipe length	[m]	T_0	Stagnation temperature	[K]
$L_{ad.}$	Length of adiabatic section	[m]	T_a	Outer insulation temperature	[K]
$L_{evap.}$	Length of evaporator	[m]	T_{int}	T_{sat} at top liquid pool	[K]
$L_{cond.}$	Length of condenser	[m]	T_{sat}	Saturation temperature	[K]
L_c	Capillary length ($\sqrt{\frac{\sigma}{\Delta \rho g}}$)	[m]	T_w	Evaporator wall temperature	[K]
L_{eff}	Effective length ($\frac{1}{2}(L_{cond} + L_{evap.}) + L_{ad.}$)	[m]	u	Axial liquid velocity	[$\frac{m}{s}$]
L_{fin}	Total cooling fin length	[m]	u_s	Liquid interface velocity	[$\frac{m}{s}$]
L_h	Total heated/heater height	[m]	v	Axial vapour velocity	[$\frac{m}{s}$]
l_s	Characteristic length ($\frac{\mu_l^2}{\rho_l \sigma}$)	[m]	v_r	Radial vapour velocity	[$\frac{m}{s}$]
l	(Dummy) length scale	[m]	V^*	Shear velocity ($\frac{\nu \eta}{g(\frac{15 \mu_l \sigma}{\rho_l^3 g^2})^{0.4}}$)	[$\frac{m}{s}$]
Ma	Mach number ($\frac{v}{c}$)	[-]	V	Total porous medium volume	[m ³]
\bar{Ma}	Marangoni number ($(\frac{-d\sigma_{lv}}{dT})(\frac{q_{fin}}{k_l})(\frac{\delta^* c_{p,l}}{\eta_l k_l})$)	[-]	V_p	Total pore volume	[m ³]
\dot{m}	Mass flow rate	[$\frac{kg}{s}$]	We	Weber number ($\frac{\rho_v \delta v^2}{\sigma}$)	[-]
\dot{m}''	Mass flux rate	[$\frac{kg}{m^2 \cdot s}$]	x	Vertical/axial distance	[m]
Nu	Nusselt number ($\frac{h l_s}{k}$)	[-]	y	Horizontal/radial distance	[m]
			y^+	Dimensionless wall distance	[-]

Symbol list, common symbols.

List of Tables

Symbol	Property	Units	Symbol	Property	Units
α	Thermal diffusivity	$[\frac{m^2}{s}]$	θ_f	Fluid fraction of fluid "f"	[-]
β	Volumetric coefficient of expansion	$[\frac{1}{K}]$	θ_i	Intrinsic contact angle	[deg]
β (53)	Fin parameter	$[\frac{1}{m}]$	θ_p	Projected contact angle	[deg]
Γ	Mass flow rate per unit width	$[\frac{kg}{ms}]$	θ_r	Receding contact angle	[deg]
γ_{min}	Min. wetting rate	[-]	μ	Dynamic viscosity	[Pa·s]
$\gamma_{min,s}$	γ_{min} , including vapour shear	[-]	ν	Kinematic viscosity	$[\frac{m^2}{s}]$
$\gamma_{min,ie}$	γ_{min} , including evaporation	[-]	ν , (73)	Poisson's ratio	[-]
$\gamma_{min,w}$	Rewetting flowrate	[-]	ξ	Evaporation number, eq. (25)	[-]
δ	Liquid film thickness	[m]	ρ	Mass density	$[\frac{kg}{m^3}]$
δ^*	Dimensionless length ($(\frac{15\mu_f^2\sigma}{\rho_l^3g^2})^{0.2}$)	[-]	σ	Surface tension	$[\frac{N}{m}]$
Δ_{min}	Min. film thickness	[-]	σ_a	Axial stress	[Pa]
$\Delta_{min,s}$	Δ_{min} , including vapour shear	[-]	σ_{lg}	Liquid-gas surface tension	$[\frac{N}{m}]$
$\Delta_{min,ie}$	Δ_{min} , including evaporation	[-]	σ_{sg}	Solid-gas surface tension	$[\frac{N}{m}]$
$\Delta_{min,w}$	Rewetting thickness	[-]	σ_{sl}	Solid-liquid surface tension	$[\frac{N}{m}]$
ϵ_a	Axial elongation	[-]	σ_{ult}	Ultimate tensile strength	[Pa]
θ_0	Equilibrium contact angle	[deg]	σ_y	Yield strength	[Pa]
θ_a	Apparent or advancing contact angle	[deg]	τ_i	Interfacial shear stress	[Pa]
			Φ	Coolant flowrate	$[\frac{1}{h}]$

Symbol list, greek symbols.

Symbol	Description	Symbol	Description
\square_0	Stagnation value	\square_i	Index
\square_{air}	Value for air	\square_l	Liquid parameter
\square_b	Parameter concerns bubble	\square_{sat}	Parameter at saturated conditions
\square_{bulk}	Value of bulk flow	\square_v	Vapour parameter
\square_c	Critical state or value	$\bar{\square}$	Mean value
\square_f	Value for fluid "f"	\square^*	Value in converging-diverging nozzle

Symbol list, sub- and superscripts, shown using dummy parameter \square .

1 Introduction

1.1 Background

In the present, a large fraction of the world's heat demand is satisfied using fossil sources. In the Netherlands, four fifths of all heat was generated directly from natural gas and oil in 2018.[1] Great potential however lies in geothermal aquifers situated in areas with large soil temperature gradients. Heat, stored in aquifers in the earth's subsurface, can be exploited in above-ground heating systems. In the aquifers, fluid is contained within layers of permeable rocks.[2] As the aquifer liquids are often either stationary or at creep velocities when unforced, heat transfer is mostly limited to conduction within the porous layers.

In order for aquifers to be of interest for heating use, the temperature of the product is to be of sufficient magnitude. In the Netherlands, temperatures in heating systems have decreased over time, but generally remain above 60°C. Hot tapwater is to be supplied at above 60° at all times.[3] Assuming a soil temperature gradient of $30 \frac{^{\circ}\text{C}}{\text{km}}$ in the Netherlands, and an average surface temperature of 10°C, aquifers at a depth of almost 2000m are of interest for the extraction of heat.[4] Please note that heat supplied at insufficient temperatures as a result of decreases in the local aquifer temperature can be upgraded, possibly with the use of heat pumps. The porosity of the aquifer matrix decreases with depth, decreasing the permeability of the aquifer.[2] With decreasing permeability, the resistance to flow and the efforts of drilling increase, making the aquifer less suitable for possible forcing of the aquifer liquid and heat extraction.

Heat can be directly extracted from the low caloric aquifers. For direct extraction, hot liquid from the aquifer is pumped upwards and returned at lower temperatures after having been used for heating purposes. Water extracted from aquifers may be contaminated when reaching the surface, requiring for additional processing steps prior to utilization above ground. Furthermore, liquid in the aquifers may deplete as a result of the direct extraction of heat. Heat can be more sustainably extracted through indirect heat transport. Here, some heat transfer device is placed into the aquifer, transferring heat towards the end-user. In this work, the applicability of heatpipes for such geothermal heat transport is discussed.

1.2 Two-phase thermosiphon heatpipes

In heat pipes, heat is transported through evaporation and condensation of the medium. As such, the medium is present in both the liquid and the vapour phase. A vertical configuration is considered, in which an evaporator is placed beneath a condenser, connected by an adiabatic section in which liquid and vapour are transported, as schematically shown in figure 1. As a result of the density difference between the two phases, vapour is transported upwards towards the condenser. The structure through which liquid flows downward varies for different vertical heatpipe types. Condensate is either transported in a single tube along with the upward rising vapour, through a separate annulus, or through a wick- or groove structure.[5]

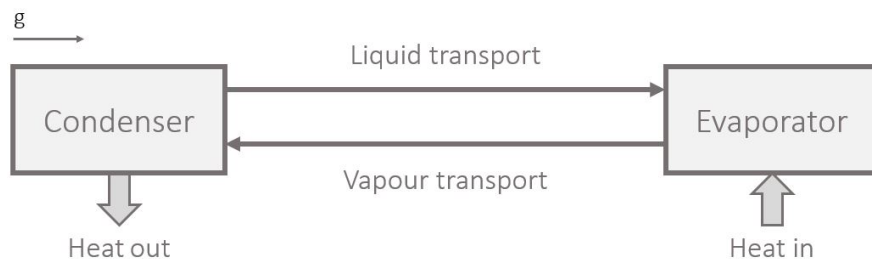


Figure 1: Simplified heatpipe schematic.

In this study, two-phase thermosiphon heatpipes are considered. Here, liquid is present in the same cylinder as the vapour, whilst unaided by a wick-structure. Ideally, liquid flows down the heatpipe walls

in a thin, annular film. Initially, the apparatus is filled with liquid at some liquid height $h_{\text{pool},0}$, see figure 2. During operation, the height of the liquid pool h_{pool} is less than initial height $h_{\text{pool},0}$, as some liquid is continuously being evaporated and is in transit through the heatpipe.

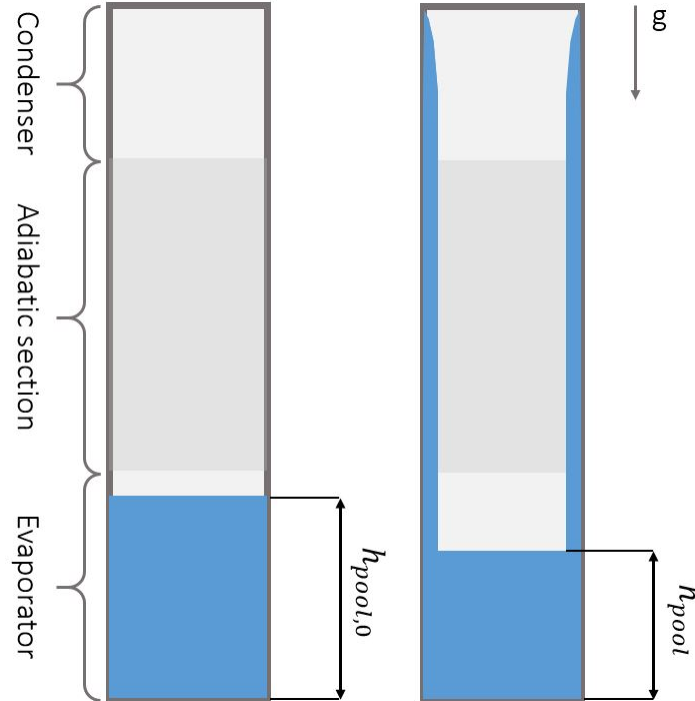


Figure 2: Development of pool height h_{pool} , figure shows cross-section of cylindrical heatpipe.

The liquid pool, however, complicates the operation of the above discussed heatpipe type for geothermal heat transport. As a result of hydrostatic pressure build-up, the pressure in the liquid pool increases with increasing distance from the horizontal vapour-liquid interface. With this, the saturation temperature of the heatpipe medium in the liquid pool increases with increasing distance from the vapour-liquid pool interface. The increase of T_{sat} with increasing pool depth for several possibly suitable fluids is depicted in figure 3. Here, with respect to the intended application of the heatpipe, a reasonable temperature of $T_{\text{int}} = 70^\circ\text{C}$ is assumed at the top interface of the pool.

As geothermal aquifers used for geothermal heating applications in which aquifer liquid is forced exceed an aquifer height of 20 meters,[4] and heat can also be extracted from a larger aquifer region in the absence of forcing, the liquid pool height may be in the order of $10^1 - 10^2\text{m}$. Please note that, with regard to figure 3, the boiling temperature increases significantly throughout the liquid pool with most fluids shown in figure 3 for such pool heights. With the exception of ammonia, the boiling temperature gradient greatly exceeds the soil temperature gradient in the aquifer (approximately $\frac{1.5^\circ\text{C}}{50\text{m}}$ [4]). As the aquifer temperature does not exceed the increased boiling temperature in the liquid pool, liquid in the pool will not boil due to aquifer heat in the absence of an external heat source. Ideally, the heatpipe transports aquifer heat during regular operation without the necessity for an external heat source (passive heat transfer device). As such, for most heatpipe media, operation in the absence of a large liquid pool is desired. As a result, film evaporation will be the dominant form of heat transfer in the evaporator. Unfortunately, the evaporation of thin liquid films is generally more complicated than pool boiling as a result of the risk for film dry-out, possibly limiting the amount of heat that can be extracted from the source.

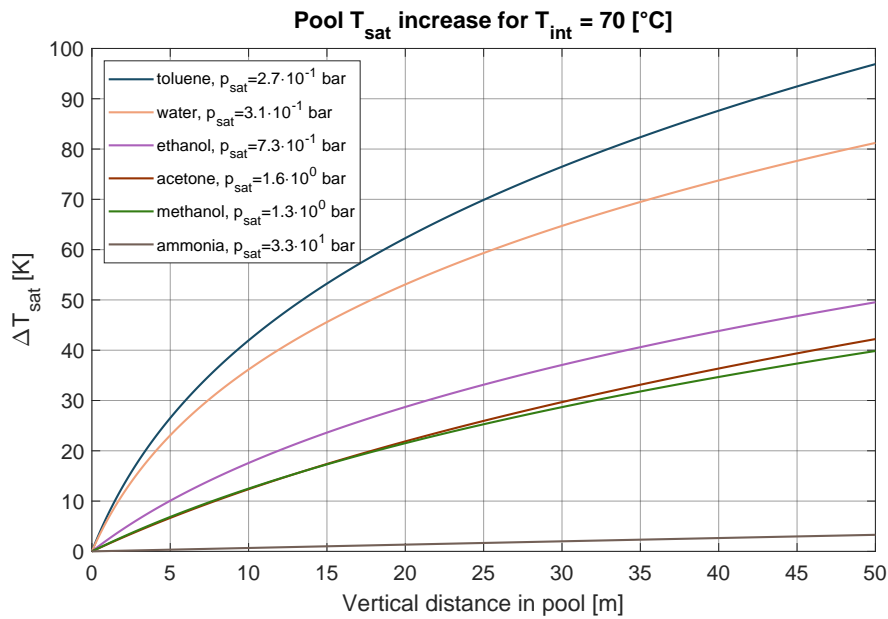


Figure 3: Increase in saturation temperature with increasing pool depth h_{pool} , fluid data taken from NIST database.[6] Figure includes fluid saturation pressures at top pool interface for $T_{\text{int}} = 70^\circ\text{C}$.

1.3 Rationale and structure of study

In this work, the extraction of aquifer heat using heatpipes is discussed. Limits to the heat flow in the apparatus are presented and, if possible, quantified. The study will lay additional emphasis on the evaporator, in which heat is to be removed by a falling liquid film during geothermal use. As will be discussed, film dry-out will be of significant importance to evaporator performance. The influence of varying boundary conditions or operating conditions on dry-out and the evaporator heat removal rate is investigated experimentally in this work. Furthermore, the concept of re-homogenization of highly heterogeneous liquid films using porous media in order to mitigate the resulting effects of film dry-out is presented and discussed.

In section 2, a theoretical overview is given of any mechanisms underlying or relevant to film heating in heatpipes, or the operation of heatpipes in general. Additionally, the flow through porous media is discussed. The experimental methodology of this study is discussed in section 3. Furthermore, section 3 contains an overview of the experimental setup, and a list of measurements to the setup and their rationale. Results are presented, discussed and compared to the expectations deduced from the theory of section 2 in section 4. The study is concluded in section 5, and a set of recommendations for future work are included in section 6.

2 Theoretical background

The following sections will aim to provide the reader with a theoretical basis of the physics underlying heatpipe operation and film heat transfer. Sections 2.1 and 2.2 discuss heat removal in liquid films, any phenomena associated with film heat transfer and boiling, and dry-out in liquid films. With this, estimations regarding the evaporator heat extraction rate can be made, and the evaporator can be modeled. There are however limits to the heat transport rate in two-phase thermosiphon heatpipes. The limits to heat flow are discussed in sections 2.4 and 2.5, and are of importance for the selection of a medium suitable for either experimental or large-scale use. A brief overview of the flow characteristics of vertically falling films is given in sections 2.4.1 and 2.4.2. Literature on the spreading of liquids in porous media is presented in section 2.3.

2.1 Heat transfer in heatpipe

In order for heatpipes to be commercially interesting for geothermal operation, heat originating from such systems is to be offered at temperatures approximating the source temperature. The system temperature drop can be characterized using a system of thermal resistances.

$$\Delta T = R_{eq} \cdot \dot{Q}_{in} \quad (1)$$

As can be seen in equation (1), the system temperature drop is proportional to the heat supplied to the system \dot{Q}_{in} multiplied with some equivalent system heat flow resistance R_{eq} . The temperature difference between the source and the sink is the driving force for heat transport. In order for heat to flow through some structure or interface, driving force is needed. As the heat flow through a structure is increasingly restricted, more driving force is needed to accommodate the intended heat flow. The amount of driving force, embodied by a difference in temperature, needed to supply an amount of heat flow \dot{Q}_{in} in the defined system is characterized by resistance R_{eq} . The equivalent resistance is the resulting resistance for heat transport through the heatpipe assembly, taking into account the resistance to heat flow from all subcomponents of the system.

The value of R_{eq} can be approximated by considering an equivalent thermal circuit, listing all resistances to heat flow on the path from heatpipe source to sink.[5]

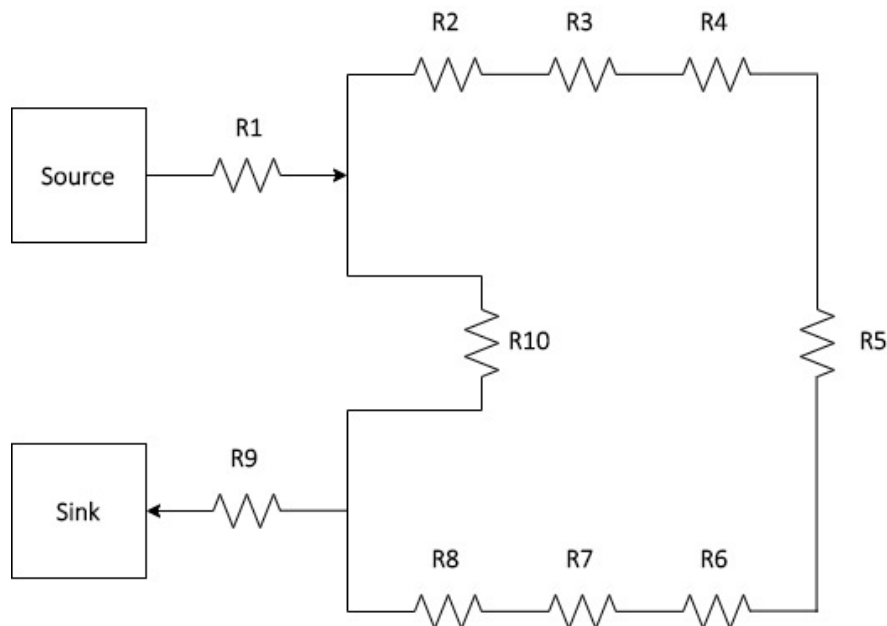


Figure 4: Generalized heatpipe heat transfer resistance scheme.

Figure 4 depicts some generic heat pipe resistance scheme, including the possible heat flow paths from the heat source - the aquifer - to the intended heat sink, the consumer. Heat is fed to the evaporator wall through the source-wall interface. The interfacial heat transfer resistance R_1 will most often describe heat flow through solid-liquid (aquifer heat) or solid-solid (electrical heater) interfaces, depending on the heatpipe setting. Similarly, resistance R_9 describes the interfacial resistance for heat removal from the heatpipe at the sink. Heat can flow to the sink either longitudinally through the pipe wall, captured with resistance R_{10} , or through the interior of the heatpipe, described with resistances R_2 to R_8 . Here, heat passes through the pipe wall per conduction, described with conduction resistance R_2 . Heat is removed from the evaporator wall through evaporation or boiling of the internal medium. The effectiveness of this heat removal is captured with R_3 . Similarly, heat is removed from the stream through condensation, the resistance of which is expressed in R_8 . If the vapour and liquid phases are considered to be in equilibrium, the respective pressures would be equal. However, as there is a net nonzero massflux through the boundary, there is no equilibrium in the evaporator. With this, the vapour-liquid interface holds a finite pressure drop, accompanied by a change in temperature between the two phases.[5] Equivalently, a finite temperature drop is found for the vapour-liquid interface in the condenser. The heat transfer resistances of the vapour-liquid interface of the evaporator and the condenser are described with R_4 and R_6 respectively. The vapour annulus is slowed by interfacial shear at the vapour-liquid interface (as per section 2.1.3), resulting in pressure loss along the heatpipe. As the vapour is at the saturation pressure, a decrease in pressure results in a decrease in temperature. The temperature drop can be expressed as a thermal resistance through R_5 .

Please note that figure 4 considers an ideal configuration, in which no heat is leaked to the surroundings of the heatpipe walls. Realistically, the surroundings will act as an additional heat sink for heat originating from the source, to which heat will flow. Losses to the surroundings limit the fraction of heat flow that is transported to the intended heat sink. Insulating the heatpipe walls will increase the resistance to heat flow towards the surroundings, and decrease the fraction of heat that is lost.

The analysis of the system can be greatly simplified with order of magnitude estimations of all resistances. As such, one will find that R_2 , R_4 , R_5 , R_6 and R_8 are many orders of magnitude smaller than the other resistances for systems filled with water.[5], [7] As such, their restriction on heat flow will be of little significance. The magnitude of resistances R_1 and R_9 can be significant for solid-solid interfaces, and may vary significantly. Thermal interfacial resistances are qualitatively discussed in section 2.1.4. The resistance to conduction in the longitudinal direction of the heatpipe wall is of such magnitude that all heat will be transported through the interior of the pipe. As such, the resistance to heat flow through a heatpipe is most dependent on the heat transfer through evaporation and condensation at the solid-liquid interfaces in the system. As such, thorough understanding of both condensation and evaporation are of importance in the design and operation of heatpipes.

2.1.1 Film condensation

The wetting ability of a wall defines the mode of liquid deposition on the condenser wall. Condensate droplets are formed on non-wetting walls, sliding in the direction of gravity when sufficiently large.[8] A complete film of condensate is formed when the condenser wall is wetting. Droplet condensation, however, yields significantly larger heat transfer coefficients than film condensation. Due to the increased complexity of creating long-lasting non-wetting surfaces (either non-permanent surface agents, or additional thermal resistance from permanent coatings are needed), this study will only consider film condensation.

Film condensation heat transfer is often approximated using a Nusselt approximation. Several assumptions underlie such approximations, as has been described by Mills et al.[8] Energy is only assumed to be exchanged through conduction. Enthalpy convection by the film is neglected as the velocity of liquid films is generally low, and the flow remains laminar. With this, the film temperature profile is assumed to be linear. The surface temperature and any fluid properties are assumed to remain constant in the

direction of the flow. Vapour is assumed to exert no drag on the film interface. As a result, the film thickness is underestimated. Vapour drag is further discussed in section 2.1.3. The heat transfer coefficient for conductive heat transfer can be expressed as per equation (2).

$$h = \frac{k_1}{\delta} \quad (2)$$

Here, the film thickness δ is to be determined. An approximation of the velocity profile of a liquid film can be found when considering a unidirectional flow, in which buoyancy forces and viscous forces are balanced. Equation (3) lists the resulting equation and the to be applied boundary conditions. As a result of the no-slip condition at the wall, the liquid is stationary when at the wall ($y = 0$). For now, the shear at the vapour-liquid interface τ_i is ignored, as per the previously discussed assumptions. The configurations in which τ_i attains a nonzero value are discussed in section 2.1.3.

$$\begin{aligned} \mu_1 \frac{\partial^2 u}{\partial y^2} + (\rho_l - \rho_v)g &= 0 \\ y = 0: \quad u &= 0 \\ y = \delta: \quad \mu_1 \frac{\partial u}{\partial y} &= \tau_i \end{aligned} \quad (3)$$

With this, an expression for the film velocity u (velocity component in the axial direction) as a function of distance y in the radial direction can be found. In equation (3), μ_1 is the local liquid viscosity of the film and ρ_l and ρ_v are the liquid and vapour densities, respectively. By integrating this expression over the film height δ , the film thickness can be expressed as a function of the film flow rate.

$$\Gamma = \int_0^\delta \rho_l u \, dy = \int_0^\delta \rho_l \frac{(\rho_l - \rho_v)g\delta^2}{2\mu_1} \left(\frac{y}{\delta} - \frac{1}{2} \left(\frac{y}{\delta} \right)^{\frac{1}{2}} \right) dy = \frac{g\delta^3(\rho_l - \rho_v)}{3\nu_1} \quad (4)$$

Equation (4) shows the mass flow rate per unit width, Γ , as a function of film thickness δ . In equation (4), ν_1 is the kinematic viscosity of the liquid. An expression for the film thickness as a function of the vertical distance x can be found from an energy balance of an infinitesimal control volume in the condensate, denoted in equation (5).[8] Please note that x attains a zero value at the top of the condenser, and increases along the condenser wall.

$$\delta = \left(\frac{4x(T_{\text{sat}} - T_w)\nu_1}{h_{\text{fg}}^*g(\rho_l - \rho_v)} \right)^{\frac{1}{4}} \quad (5)$$

From equation (5), the film thickness is found to grow at a rate of $x^{\frac{1}{4}}$. In order for the vapour to condense, the condenser wall is to be kept at some temperature below the saturation temperature of the vapour. Term h_{fg}^* describes the modified latent heat. Here, the latent heat is increased to include the additional transfer of heat that is needed to subcool the vapour to T_w . [8]

A general formulation of the heat transfer coefficient is wanted, preferably as a function of the film Reynolds number, as the Reynolds number is used to describe the flow pattern within the film. The film Reynolds number, as a function of Γ is denoted in equation (6).

$$\text{Re}_f = \frac{\rho_l u_b D_h}{\mu_1} = \frac{4\Gamma}{\mu_1} \quad (6)$$

A Nusselt number as a function of the film Reynolds number can be found using an alternative length scale. By assuming $\rho_v \ll \rho_l$, one may find equation (7). [8]

$$\text{Nu} = \frac{hl}{k_1} = \frac{h(\nu_1^2/g)^{\frac{1}{3}}}{k_1} = \left(\frac{3}{4} \text{Re}_f \right)^{-\frac{1}{3}} \quad (7)$$

A decrease in the heat transfer coefficient is predicted with increasing Reynolds number. The above analysis however considers a smooth vapour-liquid interface. For vertical films, wavy film motions appear as soon as the film flows down the plate, as described in the work of Kalliadasis et al.[9] Thin liquid films have shown the development of long (significantly larger than the film thickness) wavelength deformations on the interface. The local velocity of the film increases away from the solid-liquid interface, as can be seen from the velocity expression in equation (4). The velocity, and with this the flow rate of liquid, in the wave crests is therefore larger than in the troughs. This produces a downward motion of the perturbation without growth, moving at a higher velocity than the theoretical smooth film. Inertial effects prevent fluid at the front face of the perturbation to immediately follow the perturbation velocity profile. Similarly, fluid at the trailing face of the perturbation does not immediately follow the velocity profile of an undisturbed liquid film. As such, liquid accumulates from both the front and rear face of the wave, increasing the amplitude of the perturbation. At constant flow rates, the bulk velocity of the wavy film is larger than the velocity of the smooth film. With this, the average film thickness decreases as waves appear on the vapour-liquid interface. The experimental work of Rajamani [10] confirms this theory, and shows a decrease in average film thickness of up to 15% for a downward water-glycerol film flow. As a result, with reference to equation (2), the heat transfer coefficient of condensation in liquid films increases with wave formation. The experimental corrections to the Nusselt approximation by Chun et al.[11] are often used to approximate heat transfer in wavy laminar and in turbulent film regimes. The wavy film heat transfer coefficient correlation for water can be found in equation (8).

$$\text{Nu} = 0.822\text{Re}_f^{-0.22}; \quad 30 < \text{Re}_f < \text{Re}_{tr} \quad (8)$$

$$\text{Nu} = 3.8 \cdot 10^{-3} \text{Re}_f^{0.4} \text{Pr}_l^{0.65}; \quad \text{Re}_{tr} < \text{Re}_f \quad (9)$$

$$\text{Re}_{tr} = 5800 \text{Pr}_l^{-1.06} \quad (10)$$

Equation (7) is found to provide satisfactory results for $\text{Re}_f < 30$, [8] while equation (8) approximates the Nusselt number for the remainder of the wavy laminar flow regime. [8], [12] With further increasing film Reynolds numbers, the film transitions to a turbulent state. An approximation of the Nusselt number for turbulent films is given in equation (9). In turbulent films, the temperature in the film can be considered to be constant due to turbulent mixing, with a steep temperature drop over a narrow region near the wall. [13] For turbulent film flows, the assumptions for Nusselt approximations do no longer hold, and the heat transfer can no longer be described as such. In such flows, the heat transfer coefficient is found to increase with increasing film massflow. [8] Chun et al. [11] proposed two approximations of the onset of turbulence in falling water films. The transitional Reynolds number (Re_{tr}), denoted in equation (10), describes the Reynolds number at which the heat transfer coefficient was first found to deviate from laminar behaviour as a function of the liquid Prandtl number (Pr_l). As a first departure from laminar performance is described, this first criterion gives relatively low predictions of the transition. The turbulent transition of liquid films is also found to occur at a Weber number ($\text{We} = \frac{\rho_l \bar{u}^2 \delta}{\sigma}$) approximating unity, making for a second onset criterion. [11]

2.1.2 Film evaporation

In the heatpipe evaporator, a liquid film with finite thickness is heated by a wall with $T_w > T_{sat}$. In essence, with exception to the direction of heat flow and phase change, evaporation is similar to condensation for small values of $(T_w - T_{sat})$. [8] As such, the assumptions discussed in section 2.1.1 hold, and heat transfer for water films can be described with the formulae in equations (7), (8) and (9). At low superheating temperatures, phase change occurs on the vapour-liquid interface, once an interface temperature of T_{sat} has been reached.

Once a sufficient degree of superheating is reached, boiling is initiated near the evaporator wall. Surface cavities in the wall surface and (with initial boiling) air departing from the operating liquid with increasing temperature form nucleation spots for vapour bubbles. [8], [14] Heat transfer in the boiling regime associated with bubble growth and departure is no longer solely dependent on the film thickness. As the wall temperature further increases, increasingly smaller nucleation sites are activated. For large

liquid pools heated from below the temperature of the bulk liquid is of importance to the propagation of vapour bubbles. If the bulk temperature of the liquid layer is below T_{sat} , bubbles stop growing and collapse when in contact with the bulk fluid. In case of superheated bulk liquid layers, bubbles detach from the heater wall and rise to the vapour-liquid interface. Bubble dynamics during (film) boiling are further discussed in section 2.1.2.2. The nucleation boiling regime is associated with large heat transfer rates, as is further discussed in section 2.1.2.1.

2.1.2.1 Nucleate boiling

As liquid flows over a wall or fills a container, surface tension forces prevent the liquid from entering small cavities, in which gases are trapped. A large contact angle for the liquid-solid combination will improve the trapping ability of the liquid.[14] The gas-filled cavities will act as nucleation sites for the inception of vapour bubbles during boiling. When ignoring the partial pressure from any trapped gases inside the nucleation crevice, the pressure of a hypothetical spherical bubble in a cavity with radius R_c is found with the Laplace equation, denoted in equation (11).

$$p_b = p_\infty + \sigma \left(\frac{2}{R_c} \right) \quad (11)$$

The pressure in the bubble exceeds p_∞ , the pressure of the surrounding liquid film. As such, the saturation temperature in the bubble exceeds the saturation temperature of the surrounding flow, requiring some degree of superheating for bubble nucleation in the cavity. With increasing wall temperatures, increasingly smaller nucleation sites will be activated. As a result of the presence of trapped gases, the partial pressure of vapour is lower than p_b . As such, the presence of gases will reduce the degree of superheating required for bubble nucleation in the wall cavities. Prolonged boiling of degassed liquids will however remove the trapped gases, deactivating a fraction of the nucleation sites.[8]

The increase in heat transfer associated with the nucleate boiling regime has been the subject of discussion. As a bubble detaches from the evaporator surface, colder fluid is pulled towards the wall and heated until a sufficient degree of superheating is reached. The locally increased convection as a result of bubble growth and departure was assumed to improve the heat transfer for nucleate boiling. However, nucleate boiling heat transfer coefficients significantly surpass convection heat transfer coefficients in magnitude. The increase in heat transfer performance was found to be proportional with the bubble population.[14] Latent heat transport in bubbles detaching from the evaporator wall was found to only convey a minor fraction of the total heat flux in the evaporator. A later hypothesis suggested that an increase in heat transfer performance was a result of the formation of microlayers between the bubble and the evaporator wall.[14] Figure 5 illustrates the formation of such microlayers. Here, thin layers of liquid are subject to large thermal driving forces, with large heat transfer coefficients as a result.

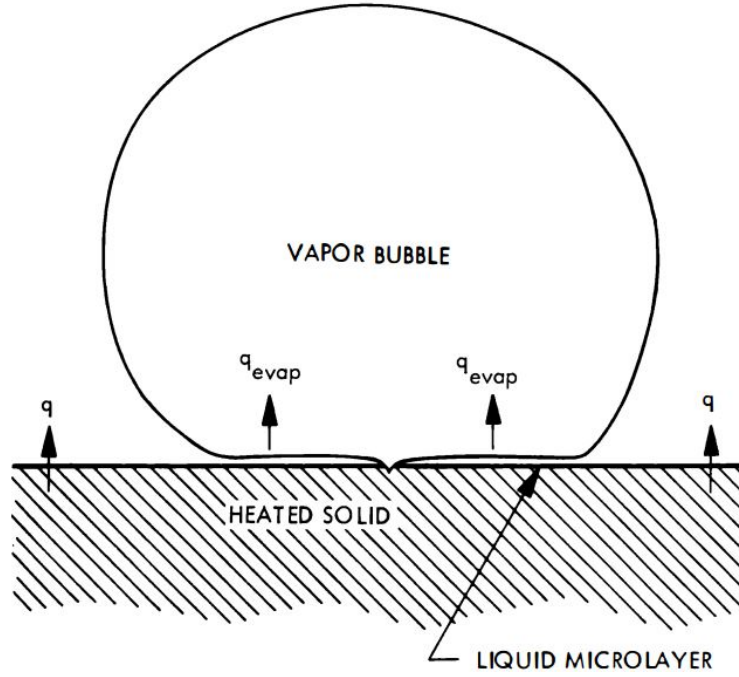


Figure 5: Evaporating microlayer at bubble nucleation location. [14]

With increasing heatflux to the evaporator wall, the bubble generation rate increases, as will be discussed in section 2.1.2.2. At some heat flux, departing bubbles will coalesce into vapour streams, and a further increase in heat flux will cause the bubble streams to become unstable.[14] In the unstable state the liquid flow towards the wall is obstructed, and a vapour film is formed.[8] As vapour poorly conducts heat, the vapour film significantly complicates heat transfer. At constant heat flux to the system, the wall heat removal rate decreases heavily, rapidly increasing the wall temperature. The heat flux at which the nucleate boiling regime initially transitions into a film boiling regime is often referred to as the peak heat flux. A general notation for the critical heat flux as a function of the maximum vapour velocity is denoted in equation (12).[8]

$$q_c = C_{\max} \cdot \rho_v v_{r,\max} h_{fg} \quad (12)$$

A value for $v_{r,\max}$ can be found either with an energy balance (kinetic energy is balanced with work by buoyancy forces) or as a result of stability analysis of the vapour column. In both cases, the expression from equation (13) is found.

$$q_c = C_{\max} h_{fg} \rho_v^{\frac{1}{2}} (\sigma(\rho_l - \rho_v)g)^{\frac{1}{4}} \quad (13)$$

Here, constant C_{\max} is geometry and configuration dependent. The work of Chang et al. [15], in which a force balance between surface tension, buoyancy and tangential inertia is considered for a bubble on a vertical evaporator wall surrounding a stationary liquid pool, finds a similar expression for the critical heat flux.[14].

$$q_c = 0.098 h_{fg} \rho_v^{\frac{1}{2}} (\sigma(\rho_l - \rho_v)g)^{\frac{1}{4}} \quad (14)$$

With their efforts, the result of which is denoted in equation (14), a value for C_{\max} is found. Ultimately, whilst ignoring additional inertia of the bulk film flow, equation (14) can be used to quantify the critical heat flux in the heatpipe exapurator. Please note that constant C_{\max} has significantly lower values for nucleate boiling in vertical heater configurations than for horizontal heaters.[14] The formation of a vapour film may benefit from sliding and vertical coalescence of vapour bubbles found in vertical boiling.

2.1.2.2 Bubble growth & frequency

The size of vapour bubbles formed during nucleate boiling is of influence to the degree of disruption to the liquid film in the heatpipe evaporator. This section will aim to give a brief overview of literature regarding bubble growth, bubble size, and bubble breakup.

Some time t_b is required for bubble growth. Here, bubble growth is a result of a phase change of liquid. In bubble formation, vapour inertia obtained through bubble growth helps detach bubbles from the nucleation surface.[16] As the bubble detaches, the section behind the bubble is filled with cold liquid, touching the heated surface. Some time is required to heat up the new liquid so that nucleation from the same site can occur, expressed with t_w . The frequency for the entire bubble nucleation cycle f_b is then defined as $f_b = \frac{1}{t_b+t_w}$. The effects of an increase in heat flux to a horizontal heater are described by Tong et al.[14] Tomar et al. [17] describe similar findings for bubble generation in film boiling. An increase in heat flux decreases the liquid heating time t_w , and increases the bubble growth rate. As such, the larger bubble growth inertia acting away from the nucleation surface will decrease the time before bubble detachment, and decrease the overall bubble size. Frequency f_b therefore increases with increasing heat flux to the evaporator wall. A decrease in bubble size effectively translates into larger bubble vapour pressures, raising the bubble saturation temperature. Additionally, a larger amount of bubble sites will be activated, further increasing the total bubble population. At sufficiently large heat flux, t_w obtains negligible values compared to t_b . As such, the maximum rate of bubble generation is found, as bubbles are formed continuously with no distance between separate bubbles.

An early effort in quantifying the size of the bubble departure diameter for nucleate boiling from a horizontal plate was found in the work of Fritz et al.[14], [18], [19] The approximation stemmed from a balance in surface forces, relative buoyancy forces, liquid inertial forces as a result of bubble growth and viscous forces. The effects of superheating were not included in their analysis, resulting in a formula only dependent of fluid properties at the saturation temperature. The dependence of the departure diameter of nucleate bubbles on the degree of superheating (expressed through the Jakob number) was later captured in the work of Cole et al.[20] A later approximation by Stephan et al.[19] included a dependency on the degree of superheating, as well on the Archimedes number (a dimensionless measure of the relative significance of buoyancy and viscous forces) and the Prandtl number.

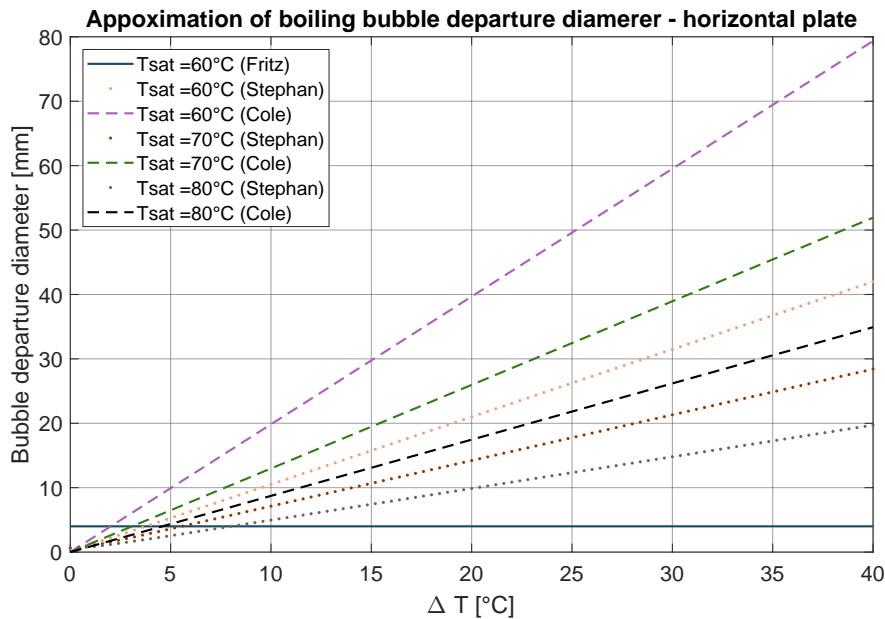


Figure 6: Approximation of bubble departure diameter for various saturation temperatures as a function of ΔT for water, as per [18]–[20].

The approximations discussed above are depicted in figure 6. The results are presented as a function of temperature difference ΔT , with ΔT being the difference between the wall temperature and the saturation temperature of the liquid pool. Please note that for water the difference in predicted departure diameters with varying saturation temperature is significantly less than for the other two discussed approximations. As a result, approximations for saturation temperatures other than $T_{\text{sat}} = 60^\circ\text{C}$ have been omitted from figure 6. Figure 6 shows an upward trend in the departure diameter for increasing degrees of superheating for the approximations of Cole et al. and Stephan et al. Furthermore, with decreasing saturation temperature the bubble departure diameter appears to increase. The rate of diameter increase grows for increasingly lower saturation temperatures. The latter trend has been discussed and confirmed in a comparison of previous experimental work by Kolev et al.[21]

The work of Hamzekhani et al. aimed to verify several approximations, including the three discussed in this section, for the departure diameter of vapour bubbles in horizontal nucleate boiling experimentally.[22] Here, predictions by the formulae of Stephan et al. and of Cole et al. were found to deviate no more than 20% from measurements. The work of Hamzekhani et al. however only draws a comparison for low degrees of wall superheating ($\Delta T \lesssim 10$). Furthermore, the expression for Stephan's approximation in Hamzekhani's work does not match the expression in the work of Stephan et al.[19], [22] There is however no clarity in whether a correct expression was used during the comparison with experiments. In the work of Kolev et al.[21] a comparison similar to the work of Hamzekhani et al. is drawn between experimental results and theoretical predictions of previous works. Above some degree in superheating ($\Delta T \gtrsim 10$) experimentally found departure diameters were found to not further increase. With further increasing ΔT , the departure diameter was found to decrease, nearing a size of approximately a single order of magnitude smaller (at $\Delta T \approx 25$) than the peak departure diameter. According to Kolev et al., the decrease in departure diameter can be attributed to a shear force originating from bubble growth at adjacent bubble nucleation sites. The influence of this shear force becomes increasingly significant for increasing degrees of superheating.[21]

Van Helden et al. [23] aimed to describe the influence of a downward liquid film flow on bubble departure on heated vertical walls. An increase in bulk velocity resulted in a decrease in bubble departure size, possibly as a result of shearing, and a change in the bubble departure angle. The influence of both downflow as upflow on vertical bubble departure was further investigated by Thorncroft et al.[24] For downflow, the downward drag exerted by the liquid film on the growing bubble acts in the direction opposite to the buoyancy force. As such, liquid shear is expected to lift bubbles from the surface. As a result, the bubble departure diameter drops with increasing liquid velocity, as can be seen in figure 7.

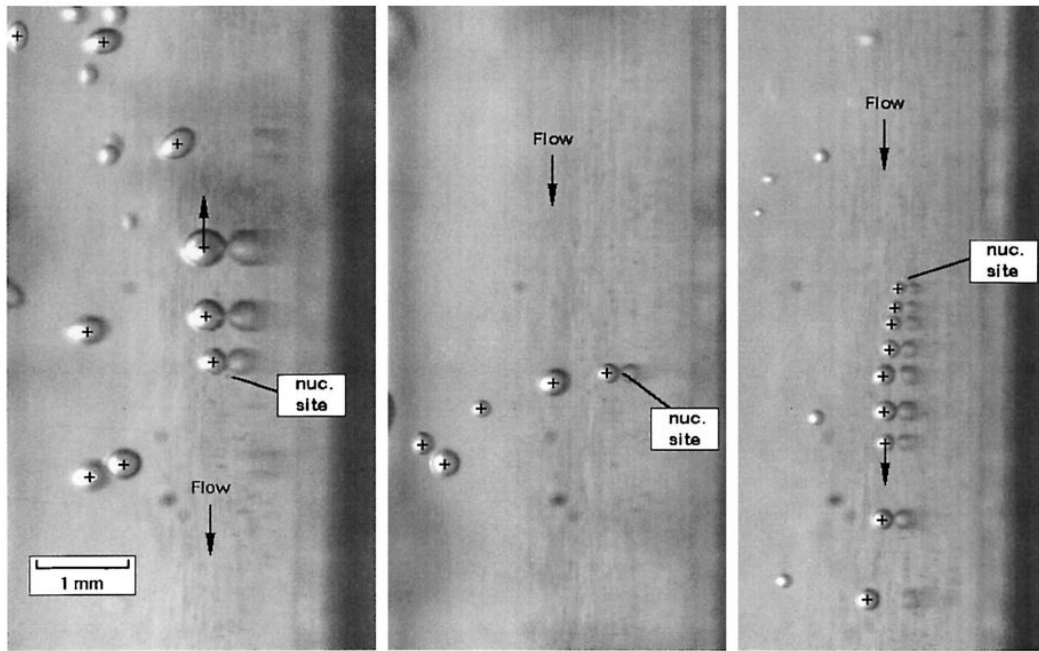


Figure 7: Bubble trajectory at low liquid mass flux (left), moderate liquid mass flow (middle), large liquid mass flux (right). [24]

Figure 7 shows the trajectory of bubbles originating from a single nucleation site at various liquid velocities. At low liquid mass fluxes (left), bubbles slide a limited distance along the heater wall, prior to being lifted-off from the surface into the bulk flow. At large liquid flow rates (right), bubbles are detached from the surface after shortly sliding downward in the direction of the liquid flow. At intermediate liquid velocities (center), sliding will not take place. Instead, bubbles will remain at the initial nucleation site before lifting off the surface. For upward sliding bubbles, as well as for upflow, the departure diameter of bubbles is inversely related with an increase in heat flux. No such clear trend for bubbles in the horizontal plane, or downward moving bubbles amid downflow can however be found.

A bubble will burst when nearing the gas-liquid surface, effectively breaking up the interface. The bursting of bubbles at interfaces is described in the work of Blake et al.[25]. For this, a bubble is considered to be at rest near the gas-liquid interface. As the film between the bubble and the interface is still relatively thick, liquid is drained by gravity. As the film thickness has decreased, Van der Waals forces will pull the film sides together, further increasing the tendency to rupture. At some critical thickness, as experimentally verified by Schelukdo et al.[26], small surface perturbations will continue to grow, resulting in a hole in the liquid film. Surface tension pulls the resulting liquid ring outwards. This liquid ring contracts to a point, and is thrown towards a single liquid jet, propagating in the surface normal direction. The jet will consequently break up into droplets. Such droplets may be entrained by the upward vapour flow in the heatpipe, as will be discussed in section 2.4.3. With increasing bubble diameter, the resulting liquid jet is found to become wider and propagates at lower velocities. The larger internal pressures of smaller bubbles result in larger amounts of energy released during bursting.

2.1.2.3 Empirical approximations

An approximation of the heat transfer coefficient in nucleate boiling is of use for the design of heater systems. Rohsenow [27] suggested that as the degree of superheating increased in boiling any convective heat transfer effects would reduce. At some degree of superheating all effects of forced convection disappear. The heat transfer in nucleate boiling was to be described as a function of the bubble Reynolds number and the Prandtl number, as per equation (15). The bubble Reynolds number (Re_b) can however

be described as a function of the Jakob number, a dimensionless measure of the degree of superheating in a liquid, and the Prandtl number. With this, the Nusselt number for nucleate boiling should be a function of the Prandtl and the Jakob number.

$$\text{Nu} = f(\text{Re}_b, \text{Pr}) = f(\text{Ja}, \text{Pr}) = f\left(\frac{c_{p,l}(T_w - T_{\text{sat}})}{h_{\text{fg}}}, \frac{c_{p,l}\mu_l}{k_l}\right) \quad (15)$$

Using the capillary length ($L_c = \sqrt{\frac{\sigma}{\Delta\rho g}}$), found from a simplified surface tension-buoyancy force balance on a bubble about to depart from its nucleation site, as the characteristic length scale a common notation for Rohsenow's heat transfer coefficient approximation is found.[8]

$$\text{Nu} = \frac{hL_c}{k_l} = \frac{\text{Ja}^2}{C_{\text{nb}}^3 \text{Pr}_l^m} \quad (16)$$

With respect to equation (16), the boiling heat flux is assumed to scale with the degree of superheating as $q \propto \Delta T^3$ and with constant C_{nb} as $q \propto C_{\text{nb}}^{-3}$. Constants C_{nb} and m depend on the fluid-solid pairing and the surface finishing of the evaporator wall.

An application specific heat transfer approximation was found in the work of Imura et al.[28], where the heat transfer coefficient was approximated for open thermosiphons. As a result of the mixing of downward flowing fluid and rising bubbles, the heat transfer coefficient for pool boiling in thermosiphons will be large in comparison with horizontal heating. The heat transfer coefficient was found not to be a function of the channel radius or length, with the exception of very narrow ($< 1.6\text{mm}$) channels, in which the heat transfer coefficient increased significantly as a result of bubble coalescence. The heat transfer coefficient was found to scale with $h \propto q^{0.4}$. Shiraishi et al. [29] suggested a pressure correction to the open thermosiphon heat transfer coefficient approximation for closed systems. Equation (17) denotes their heat transfer coefficient correlation for pool boiling in a two-phase thermosiphon. Please note that equation (17) does not consider the influence of the boiling surface or surface roughness.

$$h_{\text{p,s}} = 0.32 \frac{\rho_l^{0.65} k_l^{0.3} c_{p,l}^{0.7} g^{0.2}}{\rho_v^{0.25} h_{\text{fg}}^{0.4} \mu_l^{0.1}} \left(\frac{p}{p_{\text{atm}}}\right)^{0.23} q^{0.4} \quad (17)$$

For film evaporation, Shiraishi et al. convey finding good agreement of equation (17) with experiments for large heat fluxes. For low heat flux, the use of equation (7) is suggested by Shiraishi et al. As such, the resulting approximation for film evaporation is found in equation (18).

$$h = h_{\text{Nusselt}} = \frac{k_l}{(\nu_l^2/g)^{\frac{1}{3}}} \left(\frac{3}{4}\text{Re}_f\right)^{-\frac{1}{3}}, \quad q < q^* \quad (18)$$

$$h = h_{\text{p,s}}, \quad q \geq q^*$$

Transitional heat flux q^* is found at the intersection of both approximations, i.e. $h_{\text{Nusselt}}(q^*) = h_{\text{p,s}}(q^*)$. Recent experimental work by Jafari et al. [30] aimed to investigate the agreement of the above approximation experimentally. For low heat pipe filling ratio's, as is relevant to this study, equation (18) shows very good ($\pm 10\%$) agreement with experimental data for large heat flux. The heat transfer coefficient is however underpredicted for low heat flux.

This is however in accordance with the underprediction of the heat transfer coefficients of the Nusselt approximation for wavy falling films, as discussed in section 2.1.1. Modification of equation (18) with equation (8) for the heat transfer coefficient approximation below q^* may provide improved performance at low heat flux.

2.1.3 Interfacial shear forces

The vapour-liquid interface shear stress τ_i is of influence on the thickness of the downward propagating condensate film. An upward acting shear stress will slow down the film, as can be deduced from equation (3) with a positive nonzero value of τ_i . With this, the film thickness will increase at constant mass/heat flux through the system, and equations (7) and (8) will yield overestimated heat transfer coefficient values.

The interface shear stress for the adiabatic section of the heatpipe can be approximated using Fanning friction factors. As $\rho_v \ll \rho_l$, the velocity of the vapour annulus greatly exceeds the liquid film velocity. With this, drag on the vapour annulus can be approximated when considering a stationary liquid layer and no-slip at the vapour-liquid interface. As such, the shear stress can be expressed using equation (19), as a function of the average vapour velocity \bar{v} .

$$\tau_i = \frac{1}{2} f \rho_v \bar{v}^2 = \frac{1}{2} f \rho_v \left(\frac{\dot{Q}_{in}}{h_{fg} \rho_v A_{cs}} \right)^2 \quad (19)$$

As the vapour annulus is turbulent, a turbulent prediction for the Fanning friction factor $f = f(\text{Re})$ is required.

In film condensation however, the liquid film has a velocity component normal to its interface as a result of condensation.[8] The vapour-liquid interface is said to experience suction, as vapour is pulled towards the condenser surface. Since vapour is pulled towards the interface, a near-stationary boundary layer decreases in size. Additional shear is exerted on the vapour-liquid interface as momentum is given up to the liquid film by deceleration of the vapour from \bar{v} to interface velocity u_s . With strong suction, the magnitude of deceleration induced shear greatly exceeds the magnitude of vapour drag. In regions with large condensation rates the interface shear stress may be simplified to equation (20).

$$\tau_i = \dot{m}'' (\bar{v} - u_s) \quad (20)$$

In film evaporation however, there is a blowing effect on the vapour boundary layer.[8], [31] In contrary to the effect of condensation, blowing reduces vapour drag. At large evaporation rates, vapour drag on the liquid film can be considered to be negligible.

2.1.4 Thermal interfacial resistance

A solid interface consists of many surface irregularities. With this, solid surfaces will only have a finite amount of contact points when joined. Air, a poor conductor of heat, is trapped in the cavities between the contact points, as depicted in figure 8. In the figure, air is coloured red.

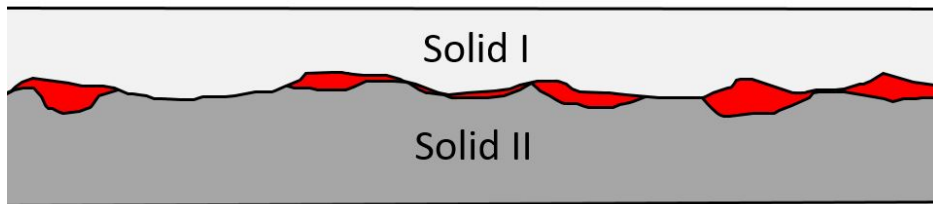


Figure 8: Solid-solid interface schematic.

The effective surface area through which heat is transferred decreases as a result of the interfacial cavities, further resisting heat flow. Heat flows in parallel through a surface area fraction of solid (conduction), and through a surface area fraction of void-trapped fluid (radiation).[8] The increased restriction to heat flow at rough surface connections results in a temperature drop over the interface. Models for the prediction of contact resistances greatly vary in the approximation of the contact point shape distribution

and the mode of deformation.[32] The interfacial resistance was found to greatly limit the heat flow to the system in the heater-wall contact in the experimental study of Hogendoorn.[33] By applying a thin layer of thermal grease (k is in the order of $1 \frac{\text{W}}{\text{mK}}$) onto the surfaces, the interfacial cavities are filled. As the conductivity of the paste significantly exceeds the conductivity of air, the interfacial resistance decreases after the application of such paste.

2.2 Dry-patches in liquid film

Dry-patches are sections on the inner evaporator wall that are not covered with liquid film. Local dry-out of the liquid film in the evaporator effectively decreases the area of heat transfer in the evaporator. With this, less heat can be removed from the evaporator wall, resulting in an increase in wall-temperature at constant heat flux. The increase in temperature is temporary and intermittent of nature for sufficiently thick liquid films, or limited heat flow to the evaporator. When more than half of the evaporator surface gets covered in dry spots, local dry-patches will join and the wall temperature increases sharply at constant heat flux.[34] As such, dry-out is highly unwanted in film evaporation. The formation of dry spots in vertical flat liquid films in the absence of heating is discussed in section 2.2.1. Consequently, section 2.2.2 will describe film thinning mechanisms in heated films, and aim to discuss the influence of heating to the formation of dry-patches.

2.2.1 Dry-patches in isothermal films

As the thickness of a liquid film decreases sufficiently, the film will break up into rivulets. Rivulets carrying the liquid are of greater thickness than a homogeneous film carrying an equivalent amount of liquid. The breakup of liquid films is depicted schematically in figure 9. The breakup of a continuous film in the absence of interfacial shear or heating is considered.

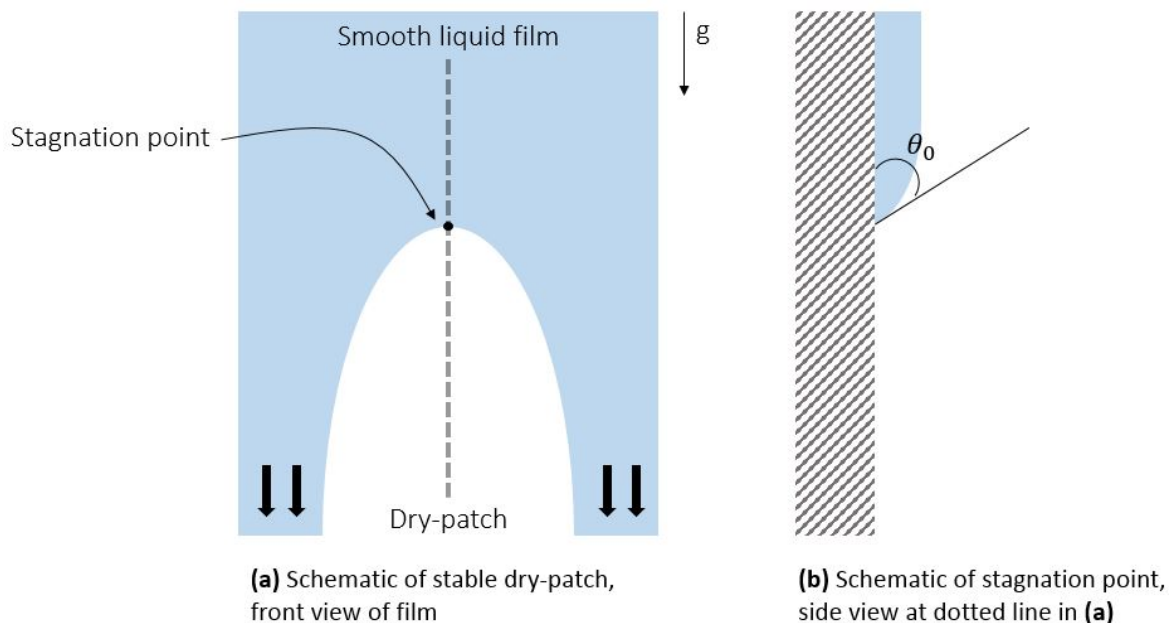


Figure 9: Breakup of continuous liquid film, from Genk et al.[35], simplified.

The flow rate at which the wall will no longer be coated with a continuous liquid film is referred to as the minimum wetting rate. Similarly, the film thickness at which the transition to rivulets takes place is referred to as the minimum liquid film thickness. The critical thickness can be approximated with a force balance at the stagnation point.[35] As a result of such analyses, the resulting minimum liquid film

thickness is found to be only a function of the equilibrium contact angle θ_0 . With this approach, the minimization of the rivulet area and the influence of the vapour-liquid interface are however not considered. When compared with experimental data from Ponter et al.[36], force balance approximations are found to overestimate the minimum liquid film thickness.[35]

As an alternative, analyses of the total mechanical energy in the flow are presented as estimators for the breakup of liquid films. In any case, the total mechanical energy, consisting of an interfacial and a kinetic subcomponent, are considered. In order to accurately capture the kinetic energy of a liquid rivulet, a reliable approximation of the rivulet velocity profile is required. Bankoff et al. approximate the energy states of the continuous liquid film and the smooth liquid rivulets separately.[37] As the mechanical energies of both configurations become equal, the liquid film will transition into a flow through rivulets. In the work of El-Genk et al. the total mechanical energy of a liquid rivulet following the breakup of a liquid film is considered.[35] Following film breakup, the energy in the rivulet is minimal. As such, minimization of the total mechanical energy of the liquid rivulet will yield the minimum liquid film thickness, and the analogous minimum wetting rate for breakup. In contrast to the approximation by Bankoff et al. that significantly underestimates the minimum liquid film thickness, the results of El-Genk et al. satisfactory agree (within 20%) with the experimental results by Ponter et al.[35]–[37]. The results of El-Genk et al. can be captured in the empirical formulae denoted in equations (21) and (22) respectively.

$$\Delta_{\min} = (1 - \cos(\theta_0))^{0.22} \quad (21)$$

$$\gamma_{\min} = 0.67\Delta_{\min}^{2.83} + 0.26\Delta_{\min}^{9.51} \quad (22)$$

Here, the dimensionless minimum liquid film thickness $\Delta_{\min} = \delta_{\min} \left(\frac{\rho_l^3 g^2}{15\mu_l \sigma} \right)^{0.2}$ and the dimensionless minimum wetting rate $\gamma_{\min} = \Gamma_{\min} \left(\frac{\rho_l \mu_l \sigma^3}{g} \right)^{-\frac{1}{5}}$ are considered to only depend on the equilibrium contact angle θ_0 .

Please note that in heatpipes the amount of fluid that is recirculated through the apparatus is solely dependent on the heat flux provided for evaporation of the liquid. Assuming the film is initially at $T = T_{\text{sat}}$, an approximation for the required heat flow to the evaporator to obtain a film thickness sufficient for flow in a continuous film at the evaporator top can be found. Please note that for this heat flow the film thickness will decrease to below the critical threshold in the evaporator.

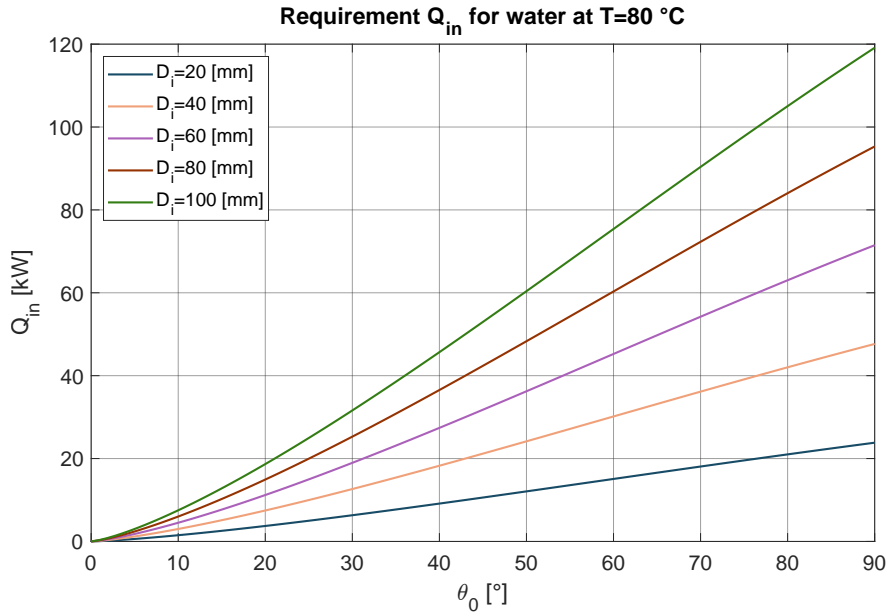


Figure 10: Required heat flow \dot{Q}_{in} [W] for continuous liquid film, for various inner heatpipe diameters.

Within the operating range of geothermal heatpipes, the least amount of heat flow is needed to find a continuous film at an operation temperature of $T = 80^\circ C$. Figure 10 shows the heatflow required to obtain a film thickness that is beyond the minimum liquid film thickness from equation (21), assuming that film break-up in annular films occurs at the same flow rates as film break-up in flat films. As the equilibrium contact angle increases towards $\theta_0 = 90^\circ$ the surface energy decreases with respect to the kinetic energy of the flow, increasing the minimum threshold for breakup. As such, a larger mass flow (and with this a larger heat flow) is needed to form a continuous film at larger equilibrium contact angles.

The influence of shear on the minimum liquid film thickness is investigated in the work of Saber et al.[38] Shear forces are only of importance for film breakup in the adiabatic section and the condenser of the heatpipe. In the evaporator, shear forces are of negligible magnitude for large evaporative fluxes, as discussed in section 2.1.3. The presence of interfacial shear stresses alters the expression for the kinetic energy of a rivulet in the previously discussed work of El-Genk et al.[35] The results of the inclusion of shear into the minimum total energy analysis for countercurrent flow can be captured with the empirical formulae denoted in equations (23) and (24).[38]

$$\frac{\Delta_{\min,s}}{\Delta_{\min}} = 1 + 0.515 V^{*2.27} (1 - \cos(\theta_0))^{0.651} \quad (23)$$

$$\frac{\gamma_{\min,s}}{\gamma_{\min}} = 1 + 0.473 (V^{*1.938} (1 - \cos(\theta_0))^{0.556}) + 1.331 (V^{*9.172} (1 - \cos(\theta_0))^{2.632}) \quad (24)$$

The minimum liquid film thickness with shear $\Delta_{\min,s}$ and the minimum wetting rate with shear $\gamma_{\min,s}$ are expressed as a function of the minimum liquid film thickness in the absence of shear Δ_{\min} and the minimum wetting rate in the absence of shear γ_{\min} , respectively. Results are limited below velocity $V^* = \frac{\nu \eta}{g \left(\frac{15 \mu_1 \sigma}{\rho_1^3 g^2} \right)^{0.4}} \leq 1$, as for V^* above unity the net liquid flow of the film is upward. For a downward film flow with countercurrent annular vapour flow, the ratios in equations (23) and (24) are always equal to or greater than one. With increasing V^* the values for $\frac{\Delta_{\min,s}}{\Delta_{\min}}$ and $\frac{\gamma_{\min,s}}{\gamma_{\min}}$ increase. As a result of the presence of shear forces, an increased amount of mass flow is needed with respect to the results from equations (21) and (22) to maintain a continuous liquid film. Please note that equations (23) and (24) have not been verified experimentally.[38]

2.2.2 Dry-patches in heated films

For heated liquid films, the formation of dry-patches was found to ensue in sections of the film thinner than the bulk thickness of the film,[39] e.g. in wave troughs. Additionally, a local decrease in film thickness may be the result of the presence of a surface tension gradient, or by departure of bubbles during nucleate boiling. The work of Fujita et al.[12], [34] describes the formation of incipient dry-patches in heated falling liquid films. In their experiments, liquid films at an initial thickness greater than the minimum liquid film thickness discussed in section 2.2.1 were investigated.

Generally, the surface tension of a vapour-liquid interface decreases with increasing temperature.[6] If a surface tension gradient is present, Marangoni stresses are induced, acting towards the region with high surface tension.[9] As a result of the surface tension induced stress, liquid is drawn towards the high surface tension region in a liquid body. Liquid films attain wavy interfaces with vertical downward propagation, as previously discussed in section 2.4.2. As a subcooled vertical downward film is heated, the temperature of the interface will increase more rapidly in thin sections (at wave troughs) than for thicker sections of the film.[9], [34] Similarly, a temperature gradient in the film interface can be found through heating with an inhomogeneous evaporator heat source. The Marangoni stresses due to present surface tension gradients in the film, as a consequence of the temperature inhomogeneity, have a tendency to draw liquid from the warmer and thinner parts towards the colder and thicker parts of the film. As a result of surface tension (as per equation (11)), however, the film pressure at the height of wave crests increases with respect to the film pressure at the wave troughs. The stabilizing pressure difference increases with decreasing wave length. For short waves, the stabilization as a result of Laplace pressure is dominant,

and the interface straightens. As waves become increasingly larger the destabilizing effect of Marangoni stresses becomes increasingly significant, and an increasing amount of liquid is drawn towards colder liquid sections.[9] As such, the local film thickness decreases significantly, possibly leading to the formation of incipient dry-patches on the evaporator wall.[34]

The departure and bursting of vapour bubbles in film evaporation, as previously discussed in section 2.1.2.2, may also result in the formation of dry-patches in a liquid film. In their experimental work Fujita et al.[12] found that dry-patches resulting from bubble nucleation were found in the lower section of evaporators. Here, the film velocity has decreased, generating larger vapour bubbles. As the bubbles leaving the film become increasingly large, little liquid remains at the location of departure. As such, an incipient dry-patch may be formed.

With sufficient liquid flow rates surrounding the incipient dry spots, dry-patches are rewetted after some time.[34] As such, the effect of dry-patches on wall temperature is limited and intermittent of nature. As the liquid flow rate however decreases below the threshold discussed in section 2.2.1, the dry-patch is no longer temporary of nature. The dry-patch area extends both downstream and upstream, and the evaporator wall temperature increases significantly at constant heat flux if more than half of the evaporator area is no longer covered with the liquid film.[34]

The theory used to derive equations (21) and (22) was further extended to include the influence of evaporation to the breakup of a continuous liquid film.[40] The rivulet energy balance is altered to include the present thermocapillary effects, and an expression for the thrust generated by vapour leaving the vapour-liquid interface. Any heat is assumed to be transferred through conduction, as the film thickness is small. The resulting minimum liquid film thickness and minimum wetting rate are presented as a function of evaporation parameter ξ , as denoted in equation (25).

$$\xi = \text{Pr}_l^{0.107} \text{Ma}^{0.128} \bar{G}^{0.34} \left(\frac{\delta^*}{l_s} \right)^{0.177} \quad (25)$$

Expressions for the variables and dimensionless numbers in equation (25) can be found in the nomenclature list. Dimensionless parameter ξ is proportional to the heat flux through the evaporator wall. With increasing heat flux, ξ increases. At large values for ξ , i.e. $\xi \geq 125$, the minimum liquid film thickness is exclusively dependent on the applied heat flux q_{evap} . Appropriate expressions for the dimensionless minimum liquid film thickness $\Delta_{\text{min,le}}$ and the dimensionless minimum wetting rate $\gamma_{\text{min,le}}$ at large evaporative flux are denoted in equations (26) and (27).

$$\Delta_{\text{min,le}} = 0.0149 \xi^{0.974} \quad (26)$$

$$\gamma_{\text{min,le}} = 1.565 \cdot 10^{-6} \xi^{3.166} \quad (27)$$

At intermediate heat flux, i.e. $0 \leq \xi < 125$, both the equilibrium contact angle θ_0 and flux q_{evap} are of importance for the breakup of liquid rivulets. The resulting critical film thickness and flow rate can be expressed as a function of equations (26), (27), (21) and (22).

$$\Delta_{\text{min,ie}} = \left[\Delta_{\text{min,le}}^4 + \Delta_{\text{min}}^4 \right]^{\frac{1}{4}} \quad (28)$$

$$\gamma_{\text{min,ie}} = \left[\gamma_{\text{min,le}}^2 + \gamma_{\text{min}}^2 \right]^{\frac{1}{2}} \quad (29)$$

Figure 11 shows the dependence of $\Delta_{\text{min,ie}}$ and $\gamma_{\text{min,ie}}$ on ξ .

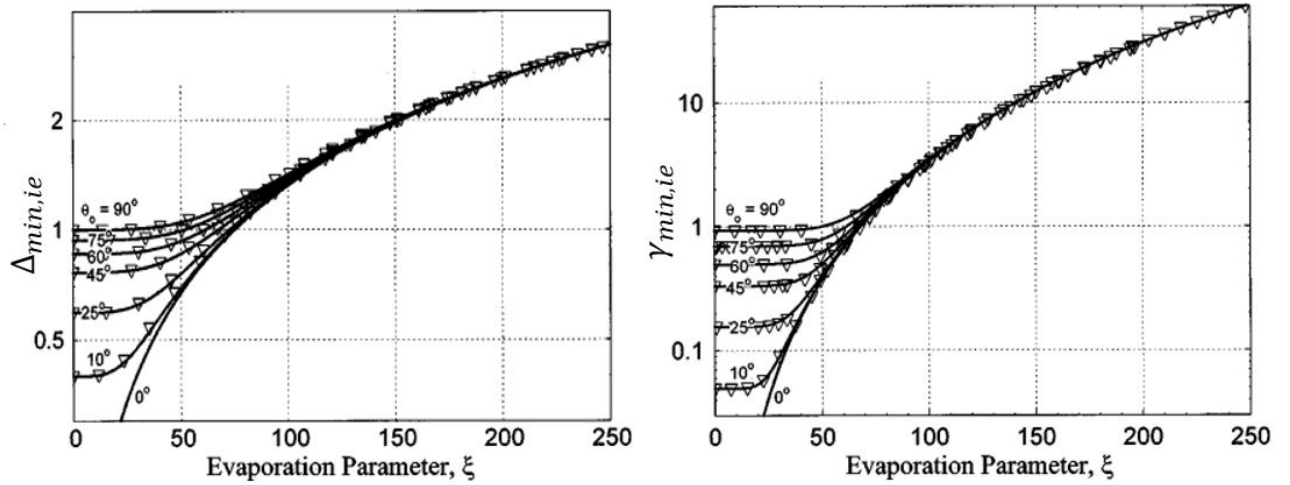


Figure 11: Dependency of $\Delta_{\min,ie}$ and $\gamma_{\min,ie}$ on evaporation parameter ξ .

In figure 11 the lines represent the empirical fit, found in equations (28) and (29) respectively. The triangles represent data points found from the analytical approximation from which the empirical fit is derived. The influence of θ_0 is found to decrease with increasing ξ . As such, according to El-Genk et al.,[40] the minimum liquid film thickness and the minimum wetting rate are both found to increase with respect to their magnitude found in equations (21) and (22) as the heat flux to the evaporator increases. As such, a larger massflow than found in figure 10 is needed to find a continuous liquid film in the heatpipe evaporator.

2.2.3 Rewetting

The analytical approximations for the formation of dry-patches shown in sections 2.2.1 and 2.2.2 are expressed as a function of equilibrium contact angle θ_0 . If the angle of the vapour-liquid-solid contact at the stagnation point is equal to θ_0 , the flow is considered to break up into rivulets. In order to rewet the dry spot on the evaporator wall, the liquid flow rate has to be increased beyond the flow rate of film breakup. As a result of contact angle hysteresis, the contact angle at the stagnation point may increase to the advancing contact angle before rewetting ensues. Contact angle hysteresis is discussed in section 2.2.4.2. An approximation for the minimum liquid film thickness $\Delta_{\min,w}$ and the minimum wetting rate $\gamma_{\min,w}$ at which dry-patches are rewetted after dry-out is found by substituting equilibrium contact angle θ_0 for the advancing contact angle θ_a in equations (21) and (22).[35] The results found from this approximation of the onset of rewetting were found agree acceptably with experimental results.[35]

2.2.4 Contact angle

The equilibrium contact angle of the vapour-liquid-solid contact point θ_0 is of importance for the critical film thickness. The critical film thickness increases with decreasing contact angles for isothermal films, as found from section 2.2.1. At low contact angles flow over a surface is considered wetting, resulting in an lesser tendency for droplet formation or flow in rivulets. The equilibrium contact angle can be approximated from a force balance in the horizontal direction between the surface force originating from solid-gas contact, the surface force from solid-liquid contact and the surface force due to liquid-gas contact of a droplet placed on a horizontal plate. The dependence of the contact angle on the surface forces is captured in Young's relation [41], denoted in equation (30).

$$\cos(\theta_0) = \frac{\sigma_{sg} - \sigma_{sl}}{\sigma_{lg}} \quad (30)$$

A surface is considered hydrophobic for $\theta_0 > 90^\circ$. Liquids will have a tendency to form droplets on such surfaces during equilibrium. Liquid will however not entirely retain its droplet shape and spread on hy-

drophilic surfaces, when $\theta_0 < 90^\circ$. Equation (30) however assumed perfectly smooth, nondeformable and chemically homogeneous surfaces. The equilibrium contact angle for droplets on infinitely smooth horizontal plates is referred to as the intrinsic contact angle, or θ_i . For non-smooth plates, the contact angle with respect to the infinitely smooth horizontal plane will deviate from the intrinsic contact angle, as will be discussed in section 2.2.4.1. With the presence of additional forces, e.g. gravitational forces on a droplet on an inclined plane, the contact angle may also deviate from the equilibrium contact angle. This deviation, contact angle hysteresis, is briefly expanded upon in section 2.2.4.2.

2.2.4.1 Surface roughness

The measured contact angle of a liquid droplet on a surface will deviate from its theoretical value from literature, as the roughness of a true surface plays a role in the physical system. Locally, the normal vector of the solid surfaces deviates from the normal vector of the infinitely smooth hypothetical solid surface. As a result the measured angle with respect to the smooth solid surface, the apparent angle θ_a , will deviate from the intrinsic contact angle.[42] Wenzel suggested that the surface roughness is quantified by parameter r , denoted in equation (31).[43] The relationship between the apparent contact angle θ_a and the projected contact angle θ_p as a function of r is given in equation (32).

$$r = \frac{\text{Actual surface area}}{\text{Idealized surface area}} \quad (31)$$

$$\cos(\theta_a) = r \cdot \cos(\theta_p) \quad (32)$$

As no physical surface is free of roughness, $r > 1$. With this, the actual contact angle deviates from the projected contact angle at all times. As such, the following applies:

$$\theta_p < 90^\circ, \theta_a < \theta_p \quad (33)$$

$$\theta_p > 90^\circ, \theta_a < \theta_p$$

For hydrophilic configurations, surface roughness further decreases the contact angle. In case of hydrophobic surfaces, surface roughness has the opposite effect.

Cassie and Baxter [44] expanded on Wenzel's work, by investigating hydrophobic surfaces in porous media. Due to the hydrophobic nature of such surfaces, fluid did not fully penetrate into all solid cavities, resulting in trapped gas-pockets and a discontinuous solid-liquid contact. In their work, an expression of the net surface energy required to form the liquid-solid interface of rough surfaces is rewritten to equation (34).

$$\cos(\theta_a) = f_1 \cos(\theta_p) - f_2 \quad (34)$$

Here, f_1 and f_2 are the fractional areas of liquid-solid and gas-solid contact, respectively. The $\cos(\theta_a)$ term decreases with an increasing solid-air covered surface fraction.

The work of Kubiak et al. [45] attempts to validate the efforts of Wenzel and Cassie and Baxter experimentally. In their study, sheets with pre-specified amounts of surface roughness were erected from various materials. Contact angle measurements were compared to a combined statement of both equation (31) and equation (34). Wenzel's theory is found to provide good contact angle estimations for wetting surfaces, that is $\theta < 90^\circ$. For each material in the study, the contact angle decreases with increasing surface roughness at intermediate roughness. This decrease is a result of droplet spreading at the intermediate roughness length scale, according to the authors. As the length scale of surface roughness increases beyond the intermediate point, the contact angle increases again for most materials in the study.

2.2.4.2 Contact angle hysteresis

The contact angle for a vapour-liquid-solid connection is not constant at some value θ_0 , but may vary over a set range. Literature on this variation of contact angles is reviewed and discussed in the work of

Eral et al.[46] A difference in contact angles is readily found in droplets attached to vertical walls. Such contact is depicted schematically in figure 12.

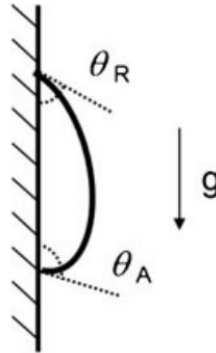


Figure 12: Liquid droplet on vertical wall, bottom and top interface contact angles at the critical advancing angle θ_a and the critical receding angle θ_r , from [46].

While remaining static, the droplet deforms. The angle of the bottom contact line increases, where the top contact angle decreases. As the droplet further increases in size, downward movement is initiated. The difference between the angle of the bottom contact during droplet translation (the advancing contact angle) and the top contact angle (the receding contact angle) is the contact angle hysteresis. Contact angle hysteresis can be regarded as a superposition of static and dynamic hysteresis. A static droplet will remain at any configuration in which the contact angles are between the advancing and the receding contact angles.[46] Please note that the static contact angle is however highly dependent on the local state and roughness of the solid surface, as previously discussed in section 2.2.4.1. As such, no average contact angle for some solid surface can be acceptably approximated. For slow-moving droplets or films, the static component of hysteresis will dominate. At larger velocities, dynamic interplay of the liquid and the solid surface further increases the advancing contact angle, and further decreases the receding contact angle.

The effect of contact angle hysteresis can be reduced by vibrating the liquid contact.[46] Such vibrations can be induced by subjecting a polar liquid to a rapidly changing AC signal, if applicable. In the case of the statically hanging droplet in figure 12, the difference between θ_a and θ_r reduces as a result of the applied vibrations. As a result, the surface forces can no longer hold the droplet against the wall, and the droplet will fall.

2.2.5 Prevention & mitigation of dry-out

In order to combat unwanted transient phenomena in the evaporation section of the heatpipe, it is of great importance to have the ability to either control the homogeneity of the liquid film throughout the evaporator, or to be able to mitigate dry-out by redistribution of the liquid film after dry-out has taken place. The following paragraphs will discuss measures to ensure the liquid film of sufficient thickness, by either altering the contact angle or increasing the flow rate, and measures involving the redistribution of annular films.

2.2.5.1 Increase in film thickness

In order to increase the thickness of the film, the film massflow has to be increased. The heat flow required to form a continuous liquid film, shown in figure 10 for various inner diameters, however often exceeds the heating limits heatpipe assemblies are subject to. As such, an increase in heat flow to the evaporator will not suffice. One could consider increasing the mass flow of the liquid film at a constant heat flow rate by introducing an additional stream of liquid to the system. By feeding an additional stream of liquid to

the condenser, and subsequently removing it from the apparatus at the evaporator, one could increase the mass flow to values sufficiently large to obtain a film thickness surpassing the minimum value for homogeneous distribution.

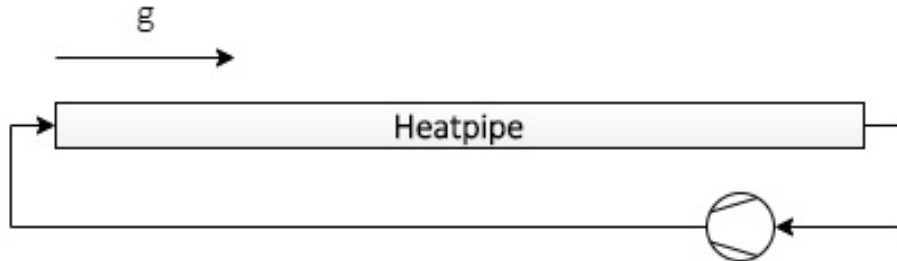


Figure 13: Theoretical schematic of additional liquid bypass.

An example of a liquid bypass is shown schematically in figure 13. By recycling an amount of liquid from the evaporator to the condenser, a sufficient film thickness can be found throughout the heatpipe. Additional complexity and cost is however introduced with the addition of a liquid bypass. A bypass introduces wear and mechanical losses to the heatpipe, inherent to the mechanical components required for pumping. Additionally, a liquid distributor is needed at the bypass entry in the condenser. Heat is no longer only transported through mechanically unforced flow, going against the principle of the gravity-driven heatpipe concept.

2.2.5.2 Coatings and liners

The equilibrium contact angle of the inner evaporator wall can be altered by lining the inner evaporator surface with a hydrophilic coating. Materials from the ceramics and polymer material groups generally have small contact angles compared to metals.[45] As such, a thin liner may significantly improve the wettability of the evaporator wall. It is of great importance to consider the thermal conductivity of possible coating materials, as polymers and ceramics are often thermal insulators. A poorly conducting coating may alter the thermal performance of the heatpipe system, and increase the temperature drop over the evaporator.

Spray-on coatings offer an alternative to solid hydrophilic coatings. Coatings as such are labeled anti-fog agents commercially. Liquid anti-fog agents often contain surface acting agents (surfactants). The degree of surfactant-solvent interaction is of great significance on the surface tension reducing abilities of the surfactant.[47] A surfactant has the ability to reduce the interfacial free energy (quantification of surface tension), if present at low concentrations. Surface acting agents consist of a part that has very little interaction with the solvent, the hydrophobic group, and a part that has strong attraction for the solvent, the hydrophilic group. When interacting with an aqueous solvent in moderate quantities, the surfactant distorts the structure of the water, by breaking hydrogen bonds the water molecules.[47] An array of hydrophobic heads adsorbed onto the liquid interface, reducing the intensity of interaction between the two phases. This results in a decrease of surface tension for the liquid-gas interface. At greater surfactant concentrations, beyond some critical concentration, various aggregates are formed in the aqueous host in addition to the interface monolayer of surfactants.[48] Beyond this onset of surfactant clusters aggregation, the contact angle will no longer change with increasing surfactant concentration. For a slightly hydrophilic surface, yielding a contact angle below 90° , a decrease in the liquid-gas surface tension force will result in a decrease in contact angle, as per equation (30).

With the evaporation of horizontal surfactant covered bodies of water, a non-evaporative layer of surfactant remains on the liquid layer whilst water is evaporating.[48] With this, the surfactant concentration of the solution increases with time during evaporation of the water. In a thermosiphon heatpipe however, the surfactant molecules will not evaporate along with the operating fluid in the evaporator as a result

of the high surfactant boiling point. With this, the surfactant molecules will remain on the upper liquid pool interface or form aggregates in the liquid pool. As a result, the addition of most surfactants will be of limited use in affecting the wetting properties of the liquid film in a heatpipe evaporator.

Additionally, according to El Genk et al.[40], the influence of the contact angle on film dry-out decreases with increasing heating intensities. As such, a decrease in the film contact angle as a result of the application of coatings of liners may be of little significance for films subject to heating.

2.2.5.3 Local homogenization

Preliminary experiments in this study showed the presence of (visually) homogeneous liquid films at the top of the heatpipe, directly below the condenser. At some distance from the top, after having passed a series of tube couplings, the film had been found to break up into a single rivulet. The previous suggests the presence of homogeneous annular films at flow rates significantly below the minimum flow rates as presented in figure 11, that break up when disrupted. An impaired tendency for breakup of the annular film was also found in the experimental study by Hewitt et al.[49] Here, the authors considered the breakup of annular water films into rivulets with the presence of a cocurrent stream of air. When unforced, the annular film did not spontaneously break down. Only when the flow rate was an order of magnitude below the minimum wetting rate (as can be approximated with the methods discussed in section 2.2.1), film break up was observed after an uneven section of the experimental setup.

After breaking up into a rivulet as result of external forcing, the liquid film should be redistributed in order to decrease the area for which there exists dry-out. A similar homogenization device could be used in the redistribution of fluid in the evaporator, at locations at which dry-out as a result of nucleate boiling has occurred. Ideally, a homogenizer redistributes and smoothens liquid over the cylinder perimeter and over time. Ideally the homogenizer outflow should be free of interfacial waves, and be equally distributed over the evaporator wall. A distillation-column-like overflow tray will distribute the liquid over the perimeter if aligned perfectly horizontal, but will not effectively smoothen over time. Ideally, the outflow area of the homogenizer is of smaller magnitude than its inflow area. A funnel-like geometry will allow for the build-up of liquid in the homogenizer. As a result, the outflow velocity will mostly be a function of the liquid height above the outflow, and temporal irregularities in the inflow will have little direct effect on the outflow. Specific porous media, if chosen correctly, may offer a constant outflow over both time and position. The flow and spreading through porous media is further discussed in section 2.3.

2.3 Porous media

The flow through a porous medium that is completely filled with a single fluid greatly differs from the two-phase filling of an initially empty or partially filled porous medium. For the redistribution of a liquid film, both modes of transport through the porous medium are of relevance.

2.3.1 Darcy's law

The flow of a fluid through a porous medium can be described using Darcy's law. The flow of fluid-phase f in control volume V is described. Through volume averaging of the governing equations of motion for all phases (including the solid porous medium) with appropriate boundary conditions, Whitaker et al. were able to theoretically derive Darcy's law.[50] The phase-average velocity vector $\langle \vec{v}_f \rangle$ of fluid f can be found from equation (35). The phase-average velocity is the volume-average velocity over the entire domain, including solid matrix. The local fluid velocity may significantly exceed the phase-average velocity.

$$\langle \vec{v}_f \rangle = -\frac{\mathbf{k}}{\mu_f} \cdot \nabla p \quad \left(= \frac{1}{V} \int_V \vec{v}_f dV \right) \quad (35)$$

The average velocity in direction n as a result of the pressure gradient in direction i , as per equation (36).

$$\langle v_{f,n} \rangle = -\frac{k_{ni}}{\mu_f} \partial_i p \quad (36)$$

During modeling, Stokes- or creeping flow is assumed. In Stokes flow, viscous forces dominate over inertial forces, i.e. $Re \ll 1$. Please note that the above modeling therefore only applies to porous media with sufficiently small pores, in order to satisfy the Reynolds number requirement. Fluid velocity $\langle \vec{v}_f \rangle$ is proportional to pressure gradient ∇p , the driving force of flow. Possible driving forces for fluid motion through porous media include hydrostatic pressure, applied pressure or force fields and molecular diffusion. Diffusion is however only important for very small Reynolds numbers, $Re < 10^{-3}$. [51] Absolute permeability tensor \mathbf{k} depends only on the characteristics of the solid pores. [52] Its values can be either approximated with empirical formulae, or found from experimental measurements on the relevant porous medium. For isotropic porous media, tensor \mathbf{k} reduces to a scalar value.

2.3.2 Flow through unsaturated porous media

During homogenization the porous medium is initially not entirely saturated with liquid. Liquid is fed to the initially dry porous medium and spreading occurs to some degree. The flow of liquid in unsaturated porous media is discussed in the work of Szymkiewicz et al. [52] Their findings are briefly discussed in this section. Here, the isothermal flow of air and water (both single-component fluids) in porous media are considered. The two phases are considered to be immiscible, and deformation of the solid matrix is neglected. Furthermore, the pressure in the air is considered to be constant and equal to the atmospheric pressure, owing to the large mobility of air in comparison with water.

Consider the flow of two fluids in a porous medium. The wetting fluid is preferentially attracted by the matrix surface. The two-fluid interface is characteristically curved, allowing for a Laplace pressure drop over the interface. For the interface in a cylindrical tube, where fluid f_2 is preferentially attracted over fluid f_1 , the pressure drop over the interface is denoted as per equation (37). As such, a driving force for the flow of fluid f_2 through the porous medium is found.

$$p_{r,1} - p_{r,2} = \frac{2\sigma \cos(\theta_0)}{r_p} \quad (37)$$

The above representation of pores as cylindrical entities however presents an upper limit to the driving force for flow at pore radius r_p . The actual driving pressure is highly dependent on the configuration of the pores, and the saturation of the respective phases in the medium. The above is discussed in the following paragraphs.

2.3.2.1 Porous scale flow

The flow at the porous scale is considered. Preferentially attracted fluid f_2 first adsorbs to the solid matrix surface at very low mass fractions (figure 14a). In water-air flows, water molecules from the pore air can be adsorbed to the matrix if the water-surface combination is wetting. At this point, fluid f_2 is immobile. For granular media, an increase in the mass fraction of f_2 will cause for liquid bridging between separate solid particles. At first, with initial bridging, the flow of f_2 is still macroscopically immobile (figure 14b). With more of f_2 , separate bridges coalesce and a continuous thicker film is formed along the matrix, and flow of fluid f_2 is possible (figure 14c). With non-granular porous media, this configuration is found directly after increasing the mass-fraction of f_2 from the adhesion configuration. Smaller pores will fill with phase f_2 with an increasing mass fraction of f_2 , as the pressure differential is larger for smaller pores. At some point, phase f_1 will lose its continuity, and will be occluded by the other phase in the porous medium, as shown in figure 14d. No macroscopic flow of f_1 is possible. As such, when modeling the two fluids as immiscible, complete saturation of the medium with phase f_2 (figure 14e) is not found.

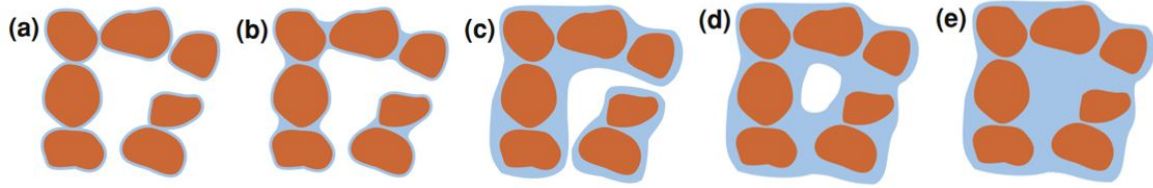


Figure 14: Spatial configurations of fluids f_1 (white) and f_2 (blue), of which f_2 is preferentially attracted to the matrix: (a) absorbed configuration, (b) liquid bridges between individual particles, only in granular media, (c) onset of f_2 mobility, (d) occluded bubble regime, (e) fully saturated configuration.[52]

2.3.2.2 Saturation & capillary pressure

At a larger scale, the flow of a fluid through a porous medium is expected to depend on the fraction of the fluid in the porous medium. The volume of fluid f with respect to the total control volume V is captured with fluid fraction θ_f . The fluid fraction of fluid f with respect to the void volume is expressed through phase saturation S_f , as per equation (39).

$$\theta_f = \frac{V_f}{V} \quad (38)$$

$$S_f = \frac{V_f}{V_p} \quad (39)$$

$$S_{ef} = \frac{S_f - S_f^{\min}}{S_f^{\max} - S_f^{\min}} \quad (40)$$

Saturation S does however not range from 0 to 1 in most common problems. In the absence of external forces or the relative dissolving of phases, S is limited as a result of the discontinuity of one of the phases. With the drainage of phase f_2 , the fluid will lose its continuity as a result of the adhesive forces discussed in the previous paragraph (figure 14a), resulting in residual saturation $S_{rf,2}$. A maximum saturation of phase f_2 ($1 - S_{rf,1}$) is found as phase f_1 is isolated in bubbles at large fractions of phase f_2 (figure 14d). The saturation of phase f can be expressed as a normalised value within the boundaries of attainable saturations. The normalised effective saturation of phase f is denoted in equation (40).

The driving force for the flow of phase f , capillary pressure difference p_c is a function of the saturation, i.e. $p_c(S_f)$. With decreasing saturation of preferential phase f_2 , p_c increases at a constant pressure of phase f_1 . The increase is a result of the large relative amount of f_2 molecules bound by short range adhesive forces at low saturations of f_2 . The capillary pressure potential p_c is however dependent on the history of the flow in the porous medium. Typical hysteresis for p_c is shown in figure 15. Please note that this figure does not include an initial wetting or drainage curve, i.e. curves originating from full saturation of one of the two present fluids in the porous medium. A porous medium, saturated with preferentially attracted fluid f_2 is considered. Fluid f_1 will only be able to invade the porous medium after the pressure of phase f_1 exceeds the pressure of phase f_2 by some margin ($p_{c,d}$ in figure 15). The capillary pressure difference someplace in the porous medium between the two phases has to be overcome by phase f_1 . The capillary pressure difference for the onset of invasion by f_1 is determined by the largest exterior pore size of the medium, as the capillary pressure difference has the smallest magnitude for the largest pores. The slope of the resulting drainage curve depends on the uniformity of the pores: with uniform pores the pressure increase for further drainage beyond the initial onset of drainage is small, as the local capillary pressure difference does not vary much in the porous medium. At some point, the residual saturation of f_2 is reached, and a significant increase in potential difference p_c is needed to further drain the porous medium of f_2 . As such, near $S_{rf,2}$, the slope of the drainage curve increases significantly. The wetting of the porous medium with phase f_2 is however controlled by the largest pore-scale in the medium, as for smaller pores the driving force for flow is largest. At low saturations S_{p2} the driving potential is large, as few f_2 molecules are present on the matrix. With increasing saturation of f_2 , the overall capillary differential decreases. As a result of the above discussed a single average capillary pressure difference state can be found for two saturation values, depending on whether a wetting or a drainage process is considered.

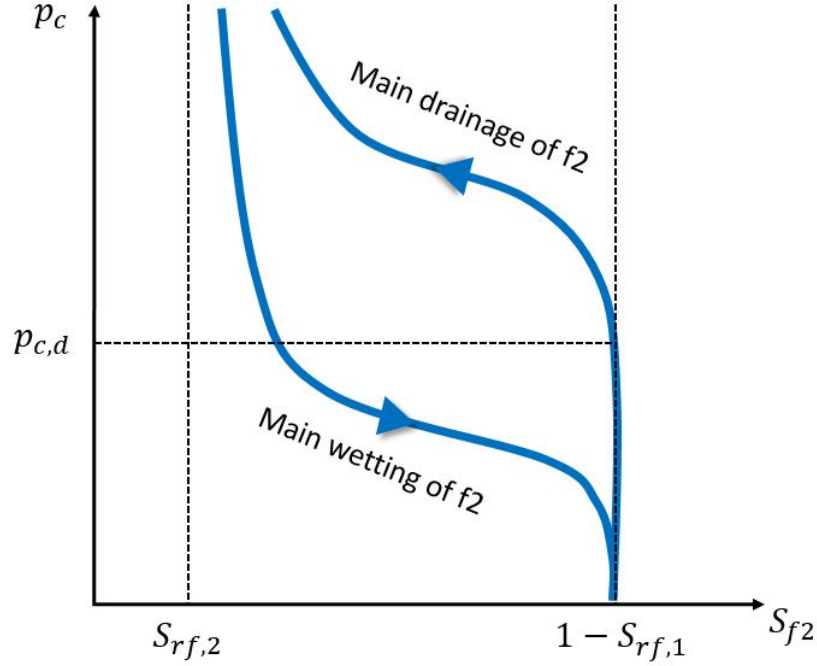


Figure 15: Typical curve form relationship capillary pressure- f_2 saturation. Here, f_2 is the preferentially attracted fluid in two-phase porous flow. Taken from [52] and simplified.

In order to accurately capture the capillary pressure difference in the porous medium, separate expressions are needed for imbibition or drainage of a fluid. During wetting, the driving force for flow decreases with increasing saturation of the considered phase.

Szymkiewicz et al.[52] further suggest that the permeability of the porous medium depends on the saturation of the considered fluid. Their simplified extension to equation (35) yields:

$$\langle \vec{v}_f \rangle = -\frac{\mathbf{k}k_{rf}(S_f)}{\mu_f} \cdot \nabla p = -\mathbf{k}\lambda_f(S_f) \cdot \nabla p \quad (41)$$

Here, k_{rf} is the relative permeability coefficient for fluid f , a function of the saturation S_f . Scalar k_{rf} will obtain a value of $k_{rf} = 0$ for $S_{ef} = 0$, and a value of $k_{rf} = 1$ for $S_{ef} = 1$. As such, the total permeability of fluid f is expected to increase with increasing saturation of f . Parameter $\lambda_f = \frac{k_{rf}}{\mu_f}$ is a measure of the mobility of phase f . The above dictates that at its minimum saturation, some fluid phase f is (almost) immobile. For two-fluid flows in a configuration in which fluid f_2 is wetting, f_2 will be drawn towards smaller pores in the medium. As such, at the same saturation for both phases the resistance to flow for f_2 is larger than the resistance to flow of f_1 .

2.3.3 Foams

In the experiments, as will be discussed in section 3.1, a foam is presented as the porous medium of choice. In the production of foams, a foaming agent is induced in a matrix material, trapping bubbles within the matrix.[53] As a result, a great volume fraction of a foam is comprised of gases. In order for the foam to spread liquid as desired, the matrix-liquid combination should be wetting, and the foam cavities should be sufficiently small. It is of importance that an open-cell foam is chosen for the re-homogenization application, as only then the foam cavities are interconnected, and flow through the foam is possible.

2.4 Liquid entrainment & falling films

In preceding work on the applicability of heatpipes in geothermal settings [33], [54] liquid entrainment was considered to be the most limiting factor to heat flow in heatpipes in the given operating range of this study. The upward inertial force of the vapour annulus may shear off or enclose droplets originating from the liquid film. The conditions at which this first occurs is the onset of entrainment. As the gas velocity is increased beyond the onset of entrainment, the liquid delivery is further reduced, and a large fraction of liquid is carried upwards.[55] Droplets were found to be formed only from larger rolling waves along the film interface.[56] The mechanisms behind rolling wave formation and the onset of rolling wave droplet entrainment will be discussed in the following paragraphs, in order to find an approximation of the limiting effect of entrainment on the heat pipe heat transfer.

2.4.1 Vertical flow regimes

The work of Weisman et al.[57] aimed to distinguish separate flow regimes for vertical pipe flow for air-water mixtures. Figure 16 shows the respective flow regime map.

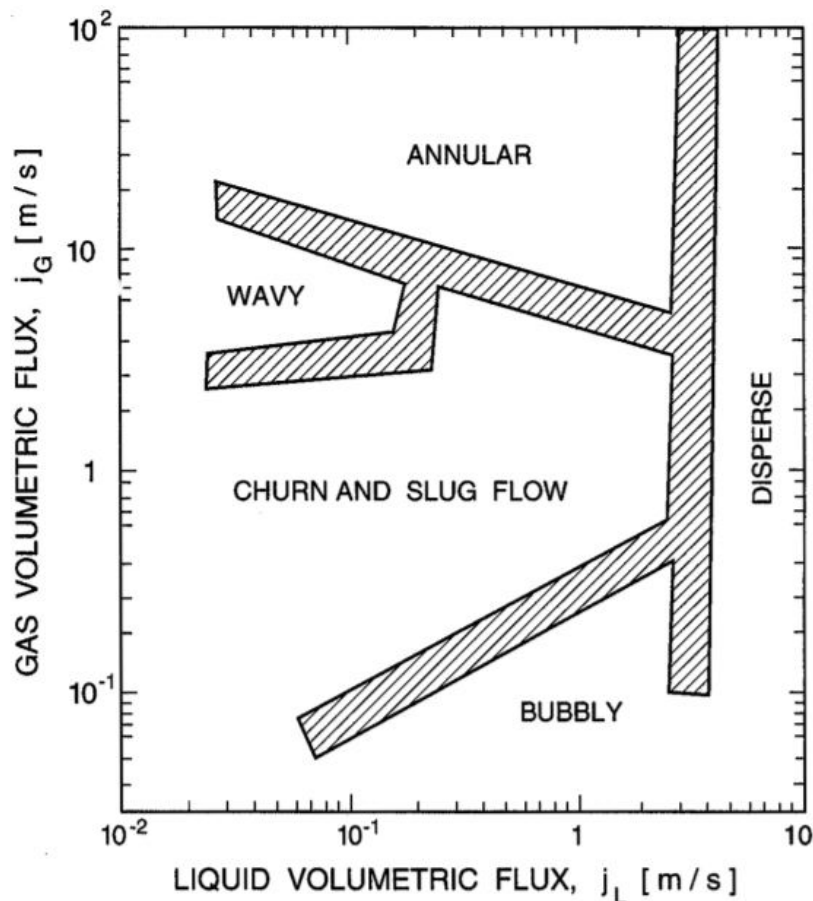


Figure 16: Air/water flow regime map with shaded transition regions, for a vertical pipe, deduced from the results of Weisman et al.[57], [58]

During steady state operation, the liquid mass flow rate in heatpipes is equal to the vapour mass flow rate. As $\rho_v \ll \rho_l$, the gas volumetric flux greatly exceeds the liquid volumetric flux. As such, possible heatpipe flow regimes should be found in the top half of figure 16. As the liquid holdup fraction in the heatpipe is low no liquid bridging will take place, taking away the possibility of slugging and churning.[55]

Weisman et al. [57] distinguish between falling film flow and annular flow. In the former, both phases are separate, and liquid trickles down the wall. The latter is characterized by the transport of a large amount of liquid droplets in the vapour annulus, as a result of the high speed motion of the vapour. In the heatpipe, such entrainment of liquid is unwanted as it directs a fraction of the film away from the evaporator wall, with possible dry-out as a result. As such, the velocity of the vapour annulus is to be kept beneath some threshold. The onset for the transition to entrainment of droplets in the annulus is further discussed in section 2.4.3.

2.4.2 Wave propagation

The presence of interfacial waves is inherent to vertical film flow.[9] Even in unforced configurations, interfacial waves will appear, as a result of the absence of stabilizing gravity forces. The free-surface velocity of the waves exceeds the film velocity. As such, waves will propagate in the direction of the flow. The above mentioned mechanism produces motion of the perturbation in the direction of the flow without perturbation growth. Growth of the perturbations is believed to stem from inertial effects in the film,[9] as has been previously described in section 2.1.1. The velocity of the waves increases with increasing amplitude. Larger amplitude waves may get to smaller amplitude waves, with the merging of waves as the outcome.[10] Further downstream the waves will lose stability, and nonlinear asymmetric waves are formed. The front face of the wave is steep, and is preceded by small ripples.[9] As a result of the continuous transverse interaction of the nonlinear waves, the wavefronts become three-dimensional in shape, as can be seen in the bottom half of figure 17.

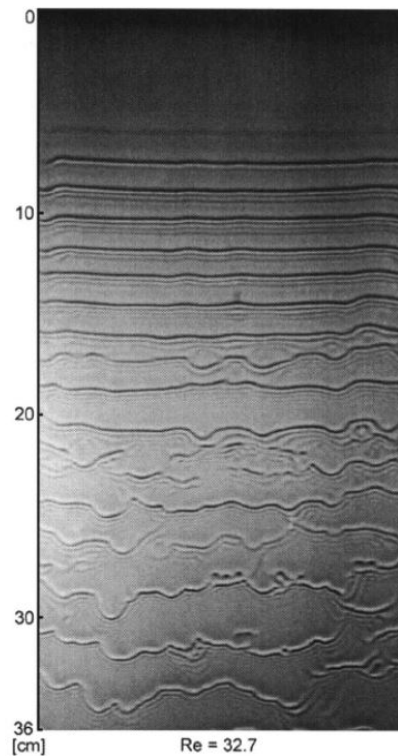


Figure 17: Propagation of interfacial waves in falling films, as per Park et al.[59]

In the work of Hogendoorn[33] the flow in transparent sections of the experimental apparatus was found to form the three-dimensional wave patterns discussed above.

2.4.3 Onset of entrainment

The entrainment of a wavy liquid film into a gas annulus is described in the work of Ishii et al.[60] Both the liquid- and the vapour flow rates are considered to be of importance for the onset of entrainment.

At sufficiently low film velocities, full dynamic interaction between the turbulent gas core and the film is not expected to take place, as the film waves do not penetrate through the gas boundary layer. A critical heat flux, above which liquid will have a sufficient flow rate for the possible onset for entrainment by a vapour annulus in a heatpipe, according to the above theory by Ishii et al., can be found with equation (42).

$$q_{\max} = 1.22 \frac{h_{fg}}{L_h} (y^+)^{\frac{3}{2}} \left(\frac{\rho_l}{\rho_v} \right)^{\frac{1}{3}} \left(\frac{\mu_v}{\mu_l} \right)^{\frac{1}{2}} \quad (42)$$

Please note that equation (42) only considers the liquid film flow rate for the onset of entrainment. It does not consider whether the inertia of the vapour flow is sufficient to entrain liquid droplets. A review of experimental data by Azzopardi et al.[56], however, shows a trend in the onset of entrainment that is not conform the theory by Ishi et al.[60] In a collection of experiments, the limit to entrainment is found to show asymptotic behaviour towards increasingly larger liquid flow rates. Only with large vapour velocities, a criterion based on a minimum liquid flow rate for entrainment can be deployed.[61]

The work of Ishii et al. [60] further covers the influence of vapour velocity on entrainment. Various entrainment mechanisms are described, of which three are depicted in figure 18. The first type of entrainment, in which liquid droplets are sheared off a roll wave crest, is often found for co-current flows with intermediate Reynolds numbers ($Re_f > 2$, for vertical films). Type 2 entrainment is found for either laminar co-current flows, or in counter-current annular flows. The steep fronts of waves in the liquid film are undercut and disintegrated into droplets by gas flow.[55]

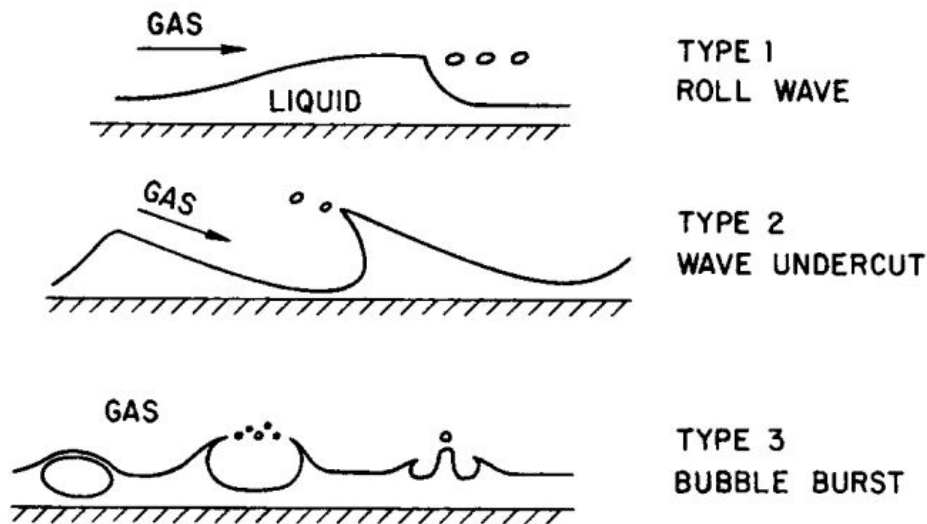


Figure 18: Various entrainment mechanisms.[60]

The bursting of vapour bubbles at the film interface (type 3) has previously been discussed in section 2.1.2.2. As bubbles burst, thinning of the liquid jet will result in droplet formation. Droplet formation as a result of bursting is inherent to nucleate boiling. As the heat flux is increased, the bubble population increases, with an increase in droplet formation as a result.[12] A balance between surface tension, vapour inertial forces and gravitational forces will bring further insight into whether droplets are further torn apart (secondary nucleation), or carried away by the vapour annulus.

The onset of type 2 entrainment is often expressed with the film Weber number. The Weber number is a dimensionless measure of the relative effect of the gas phase inertia and surface tension. Above some critical Weber number We_c droplet entrainment is assumed to take place. Above this threshold, extreme deformation of the wave leads to breakup of a fraction of the wave into droplets.[61]

$$We = \frac{\rho_g \delta v^2}{\sigma} \geq We_c \quad (43)$$

Using an expression for film thickness δ with negligible interfacial shear force (equation (45)), an expression for the heat flow as a function of the vapour velocity (equation (44)), and equation (43), an upper heat flux limit prior to entrainment can be found.

$$\dot{Q}_{in}(v_g) = v \frac{\pi}{4} D_1^2 h_{fg} \rho_v \quad (44)$$

$$\delta(\dot{Q}) = \left(\frac{3 \nu_l \dot{Q}_{in}}{\pi D_1 h_{fg} g \Delta \rho} \right)^{\frac{1}{3}} \quad (45)$$

The critical heat flow for the onset of entrainment in a cylindrical heatpipe as per a Weber number approximation is denoted in equation (46).

$$\dot{Q}_{max} = 0.26 \pi h_{fg} (We_c \sigma \rho_v)^{\frac{3}{7}} \left(\frac{g \Delta \rho}{\nu_l} \right)^{\frac{1}{7}} D_1^{\frac{13}{7}} \quad (46)$$

Varying values for the critical Weber number We_c have been reported in literature, often in the range of $1 < We_c < 20$. [5], [60] The magnitude of the critical Weber number is found to decrease for decreasing fluid viscosity.[60]

2.5 Vapour pressure

A limiting effect of the velocity of the vapour annulus on heat transfer in a heatpipe is not only found in entrainment. Operation at significantly negative gauge pressures will limit the allowable friction pressure drop on the gas core. Furthermore, increased heating rates may result in choked vapour flow. Both phenomena will be discussed in sections 2.5.1 and 2.5.2, respectively.

When modeling the flow of the vapour annulus as one-dimensional, the pressure gradient can be approximated for the three sub-components of a heatpipe. Throughout the entire heatpipe, a pressure gradient due to frictional drag forces at the liquid-vapour interface is present. The viscous drag related pressure drop depends on whether the flow is laminar or turbulent. In a one-dimensional model, vapour enters the evaporator radially, with no axial velocity component. A pressure gradient in the evaporator is necessary to provide the momentum flux in the axial direction, i.e. $\Delta p = \rho_v v^2$. [5] The total pressure drop in the evaporator is given by the sum of the pressure drop due to the axial acceleration of the vapour and the pressure drop due to drag on the vapour. In the condenser, the vapour is further slowed with recovery of the pressure as a result. However, only a fraction of the pressure is however recovered in the condenser.

2.5.1 Viscous limit

With low-temperature heatpipe operation, the saturation pressure of the medium in the evaporator may be very small. Viscous forces acting in the direction opposing the direction of the flow may become of the same magnitude as the pressure related driving force of the vapour annulus. At this point, the vapour pressure is unable to sustain a further increase of flow.[62] In the viscous limit, the pressure at the end of the evaporator is approximately equal to the pressure drop over the adiabatic section, as per equation (47).

$$p_e \approx \left(\frac{dp}{dx} \right) L_{ad}. \quad (47)$$

In case the viscous limit is restricting a further increase in heat flow, driving forces (a pressure difference) to the flow are generally small. Here, the flow can be considered to be laminar. For larger evaporator pressures, a more restrictive and accurate limit is found when approximating the pressure drop $\frac{dp}{dx}$ as per a turbulent flow. However, for large evaporator pressures the viscous limit will generally not be restrictive to the heatflow of a heatpipe, a turbulent approximation of the pressure gradient as a result of viscous drag is therefore not considered when approximating the viscous limit. The pressure gradient in the adiabatic section can be expressed as a function of heat flow \dot{Q} . As such, assuming laminar vapour flow, an approximation of the viscous limit is found, denoted in equation (48).[63]

$$\dot{Q}_{\max} = \frac{\pi D_i^4 h_{fg}}{256 \mu_v L_{\text{eff}}} \rho_v p_v \quad (48)$$

Please note that for most fluids, the viscous limit will pose no significant restriction on heat flow in an experimental setting, as the pressure drop is often small with respect to the operating pressure. For geothermal applications however, in which heatpipes are extended towards geothermal aquifers, length scales are often two orders of magnitude larger. For the temperature range of common aquifers, the limiting effect of viscous forces may be of great importance. Here, fluids with greater saturation pressures in the relevant temperature range, such as ammonia, should be considered.

2.5.2 Sonic limit

The vapour annulus is often modeled whilst assuming incompressibility of the gas. Flow of compressible media can be considered incompressible if the Mach number does not exceed a value of 0.3, i.e. $\text{Ma} = \frac{v}{c} \leq 0.3$. [64] Below this threshold, density changes in the medium are not significant. Compressibility of the medium should however be taken into account for large heat fluxes. The path of the vapour annulus shows resemblance with the flow of fluid through a converging-diverging nozzle.[5] However, in a heatpipe the area remains constant whilst the massflow varies. The massflow towards the top of the evaporator increases with increasing height. With increasing massflow, the Mach number of the vapour flow increases. The velocity-area differential shown in equation (49) applies for compressible flows.[64]

$$\frac{dv}{v} = \frac{-1}{1 - \text{Ma}^2} \frac{dA}{A} \quad (49)$$

Following from equation (49), a decrease in area will increase the speed of flow for subsonic ($\text{Ma} < 1$) flows. For supersonic ($\text{Ma} > 1$) flows however, an increase in area will lead to a velocity increase. For constant massflow, an increase in area is needed to accomodate flow acceleration, as the decrease in density outweighs the increase in velocity.[64] The maximum possible outflow through a duct is when the throat of the converging-diverging nozzle is at sonic conditions.[65] The throat will carry no additional massflow beyond this point. The flow is considered to be choked. An approximation of the maximum massflow through a throat is given in equation (50), when approximating the flow in one-dimensional fashion.

$$\dot{m}_{\max} = \rho^* A^* v^* = k^{\frac{1}{2}} \left(\frac{2}{1+k} \right)^{\frac{1}{2} \frac{k+1}{k-1}} A^* \rho_0 (RT_0)^{\frac{1}{2}} \quad (50)$$

Here, A^* is the area of the throat, which can be assumed to be equal to the heatpipe inner diameter D_i . Stagnation temperature T_0 should be chosen as the temperature at the bottom of the evaporator[5], with ρ_0 being the vapour density for this temperature. An expression for the maximum heatflow prior to choking can be formulated by multiplying equation (50) with the enthalpy of vaporization, h_{fg} .

3 Methodology

The experimental setup in this work stems from the work of Hogendoorn[33]. The following chapters will aim to defend the use of this pre-existing setup to some degree, and describe any design choices taken throughout the study. Section 3.1 will include an overview of the heat transfer limits (including a comparison between lab-scale and large-scale setups) of the setup, discuss the selection of an operating medium, and describe all relevant sub-components of the experimental setup. A brief summarized overview of the experimental apparatus is given in section 3.2. At last, an overview of all measurements is given in section 3.3.

3.1 Experimental setup

In order to investigate film heat transfer in the heatpipe evaporator and in order to confirm the findings discussed in section 2, an experimental setup was erected. The experimental setup is described in the following paragraphs.

3.1.1 Fluid selection

Working fluids can be systematically selected with the use of figures of merit.[5] Figures of merit are to be maximized or minimized groupings of material properties. An appropriate figure of merit is application specific, as such there is not one universally applicable figure of merit. In the case of heatpipes, a suitable medium would either increase a restrictive limit to heat transfer, or increase the heat transfer rate per unit area. In any case, the heat transfer (limit) can be formulated as per equation (51).

$$\dot{Q} = C \cdot (M)(G) \quad (51)$$

The total heat flow or the heat transfer limit can be expressed as a function of constants (C), a material group (M), and a remaining general, non-material specific group (G). In essence, material group M can be used as the figure of merit for the specific expression of \dot{Q} . Through comparison of the value of M for various materials, heat flow (limit) \dot{Q} can be maximized. All figures of merit discussed below have been tabulated in table 1.

In previous work on the use of heatpipes for geothermal purposes, a figure of merit based on the heat transfer coefficient was proposed.[33], [54] Here, figure of merit M is taken from the Nusselt approximation for film evaporation/condensation, seen from equation (7). Figure 19 shows the magnitude of this figure of merit for various fluids. For film evaporation, water is found to yield a significantly larger figure of magnitude than the other fluids listed in figure 19.

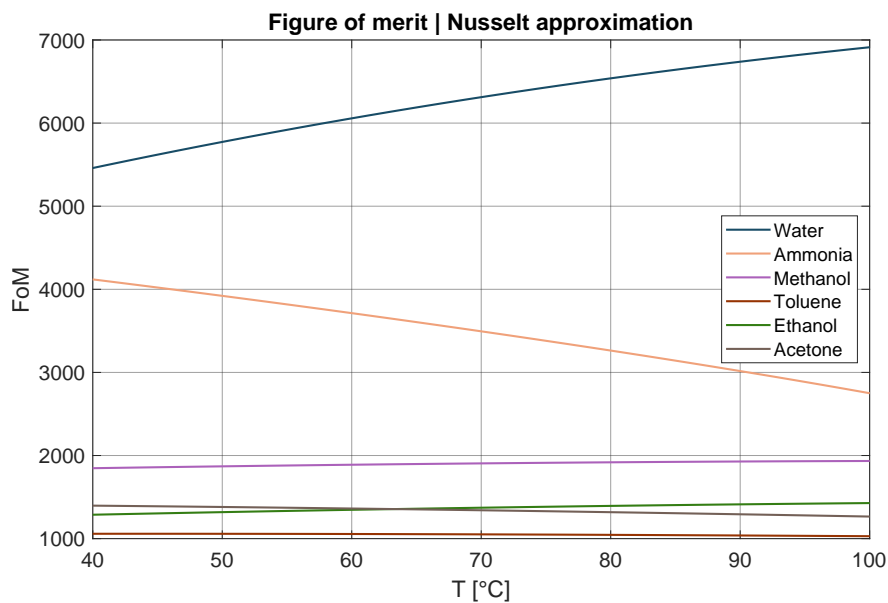


Figure 19: Figure of merit, maximization of heat transfer coefficient (Nusselt film evaporation).

Special attention is drawn to the relative difference in figure of merit between water and ammonia as operating fluids. As discussed in section 1.2, there is a possibility for aquifer driven pool boiling with ammonia-filled heatpipes. Figure 19 however suggests that the figure of merit of water significantly exceeds the figure of merit for ammonia, when considering Nusselt's film evaporation approximation. The previous implies that for a similar setting, a greater area of heat transfer is needed in the evaporator for ammonia-based devices.

At sufficient degrees of superheating the heat transfer coefficient may attain a great magnitude. Here, the heat transfer can be more accurately predicted using nucleate boiling correlations. As such, a figure of merit based on a nucleate boiling heat transfer coefficient approximation is proposed. Figure 20 shows the figure of merit based on the Shiraiishi heat transfer coefficient (equation (17)) for various operating fluids. Again, the figure of merit of water, albeit less significantly, exceeds the figure of merit for the other fluids listed in the figure.

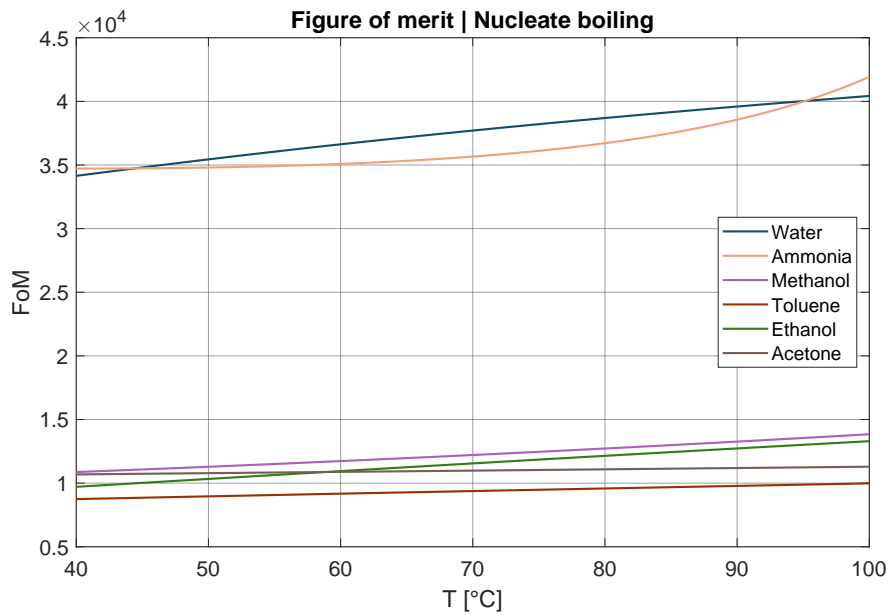


Figure 20: Figure of merit, maximization of nucleate boiling heat transfer coefficient as per Shiraishi [29].

Figures of merits can also be used for the maximization of heatpipe heat flow limits. An overview of all heat transport limits is given in section 3.1.2.1. Owing to the significantly greater saturation pressure within the geothermal operating temperature range of ammonia with respect to the other fluids considered in the analysis, the viscous limit of ammonia greatly exceeds the viscous limit of all other substances. Similarly, in a comparison of the sonic limit, the significantly greater density of ammonia (owing to the greater saturation pressure of ammonia filled systems) results in significantly lower vapour velocities with ammonia filled systems.

A comparison of the figure of merit based on the maximization of the entrainment limit is shown in figure 21. In contrast with the comparison for heat transfer coefficient-based comparisons, ammonia is found to be the preferential fluid when the entrainment limit is to be maximized. For temperatures below 90°C , a range relevant to the intended geothermal application of heatpipes, the figure of merit of ammonia exceeds the figure of merit of water.

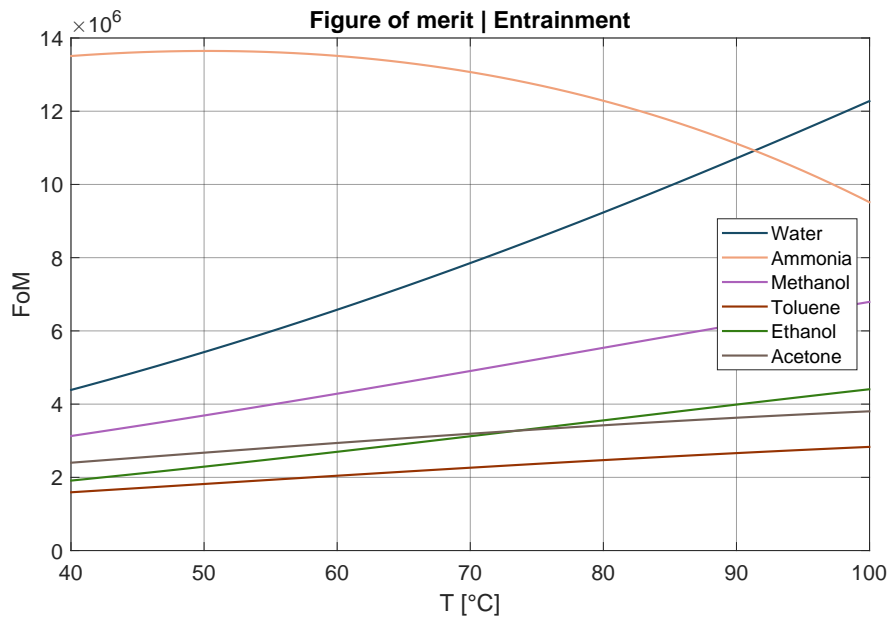


Figure 21: Figure of merit, maximization of entrainment heat transfer limit.

A comparison of the figure of merit based on the maximization of the film boiling limit is shown in figure 21. Owing to the greater vapour density of ammonia with respect to all other fluids in this analysis at the relevant temperature range, an ammonia filled system will see a departure to film boiling at the greatest heat flux. For a significant fraction of the operating range, the film boiling limit of ammonia exceeds the limit of water more than twofold.

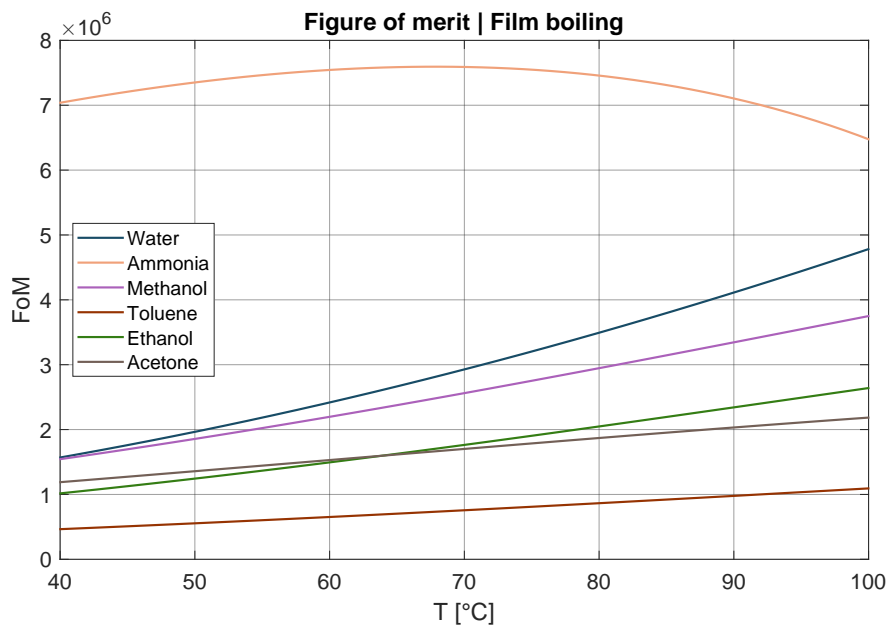


Figure 22: Figure of merit, maximization of film boiling heat transfer limit.

Figure 19 shows an almost twofold difference between the heat transfer characteristics of water and ammonia filled heatpipes. When considering evaporation at greater heat fluxes however, as per figure 20, the difference is less significant. As nucleate boiling is often the most relevant mode of heat removal in

heatpipes, both ammonia and water can be chosen as appropriate media. An ammonia-filled system is expected to be able to transport more heat than an equivalent water-filled heatpipe, as all heat flow limits attain greater values for ammonia filled systems for saturation temperatures below 90°C. The relative significance of the limits for both a lab-scale setup and a full-scale version is discussed in section 3.1.2.2. In full-size heatpipes for geothermal use, in which as much heat as possible is to be transferred through the system, ammonia should be chosen as the working fluid. The additional degree of user-safety, the compatibility with the existing experimental setup, and the amount of applicable literature found with water-filled columns resulted in the use of (demineralized) water as the medium of choice in this study.

Maximization of:	Expression
Film evaporation heat transfer coefficient	$M = \left(\frac{h_{fg}(\rho_l - \rho_v)k_l^3}{\gamma_l} \right)^{\frac{1}{4}}$
Nucleate boiling heat transfer coefficient	$M = \frac{\rho_l^{1.08} k_l^{0.5} c_p^{1.17}}{\rho_v^{0.42} h_{fg}^{0.67} \mu_l^{0.17}} p_{sat}^{0.383}$
Entrainment heat flow limit	$M = h_{fg} \rho_v^{\frac{3}{7}} \left(\frac{\rho_l - \rho_v}{\gamma_l} \right)^{\frac{1}{7}}$
Film boiling heat flow limit	$M = h_{fg} \rho_v^{\frac{1}{2}} (\sigma(\rho_l - \rho_v))^{\frac{1}{2}}$
Viscous heat flow limit	$M = \frac{h_{fg} \rho_v p_v}{\mu_v}$
Sonic heat flow limit	$M = h_{fg} k^{\frac{1}{2}} \left(\frac{2}{1+k} \right)^{\frac{1}{2} \frac{k+1}{k-1}} \rho_0 (RT_0)^{\frac{1}{2}}$

Table 1: Expressions of the figures of merit discussed in section 3.1.1

3.1.2 Heat flow limits

As discussed in section 2, there exist limits to the amount of heat that can be transported through a two-phase thermosiphon heatpipe. If there exists a minimum requirement to the heatpipe heat flow rate, the heatpipe tube diameter is to be varied in order to accommodate this requirement. The following paragraphs will aim to discuss the influence of tube diameters, operating media (water vs ammonia) and a difference in length scales (lab vs full-scale) on the heatpipe operating limits.

3.1.2.1 Overview of operating limits

Prior to designing the experimental setup, it is of importance to be able to quantify the limits to the throughput of the heatpipe. An increase in heat flow through the apparatus is not possible beyond any of the limits. Table 2 gives an overview of any limits to heat transfer discussed in section 2.

Limit	Expression	Section	Source(s)
Film boiling	$\dot{Q}_{max} = 0.098 \pi D_1 L_h h_{fg} \rho_v^{\frac{1}{2}} (\sigma(\rho_l - \rho_v)g)^{\frac{1}{4}}$	2.1.2.1	[14], [15]
Entrainment	$\dot{Q}_{max} = 0.26 \pi h_{fg} (We_c \sigma \rho_v)^{\frac{3}{7}} \left(\frac{g \Delta \rho}{\gamma_l} \right)^{\frac{1}{7}} D_1^{\frac{13}{7}}$	2.4.3	[60], [61]
Viscous	$\dot{Q}_{max} = \frac{\pi D_1^2 h_{fg}}{256 \mu_v L_{eff}} \rho_v p_v$	2.5.1	[63]
Sonic	$\dot{Q}_{max} = \frac{\pi D_1}{4} h_{fg} k^{\frac{1}{2}} \left(\frac{2}{1+k} \right)^{\frac{1}{2} \frac{k+1}{k-1}} \rho_0 (RT_0)^{\frac{1}{2}}$	2.5.2	[65]

Table 2: Overview of limits to heat transfer heatpipe.

The limits listed in table 2 are merely approximations, and will deviate from reality. In any case, operation at a heat flow in the proximity of one of the limits should be avoided. Please note that the film boiling heat flow limit derives from a limit to the heat flux. As such, an increase in the heating area ($A_h = \pi D_1 L_h$) will allow for larger system heat flows. The value for the heated height L_h differs significantly for experimental systems and operational-scale geothermal heatpipes. The film boiling heat flow limit for large-scale systems will therefore greatly exceed its experimental setup counterpart.

Please note however that the heat transfer area may decrease significantly for film evaporation as a result of dry-out and flow in rivulets, as is discussed in section 2.2. As such, the heat flow rate through the system may be significantly lower than expected, and the limits of table 2 may not have been reached.

3.1.2.2 Limits & tube sizing

Please note that for some part the experimental setup in this work stems from the preceding study of Hogendoorn.[33] As a prerequisite, the experimental setup was to convey a heat flow of 20 kW. As all heat transfer limits are in some form a function of inner pipe diameter D_i , D_i was varied until all heat transfer limits exceeded the heat transfer requirement. In order to reduce the temperature drop over the evaporator wall and to ensure that conduction is not the limiting resistance to heat transfer, conductive evaporator wall materials were sought after. The evaporator was constructed from copper, yielding a conductivity of approximately $400 \frac{W}{mK}$. Copper tubing is listed by some nominal diameter D_n in inches. For this work, only thin-walled (type-M) copper tubes were considered. In the work of Hogendoorn[33], a tube size of 2 inch ($D_i = 51\text{mm}$) was found to be the smallest commercially available sizing able accommodate a heat flow of 20 kW.

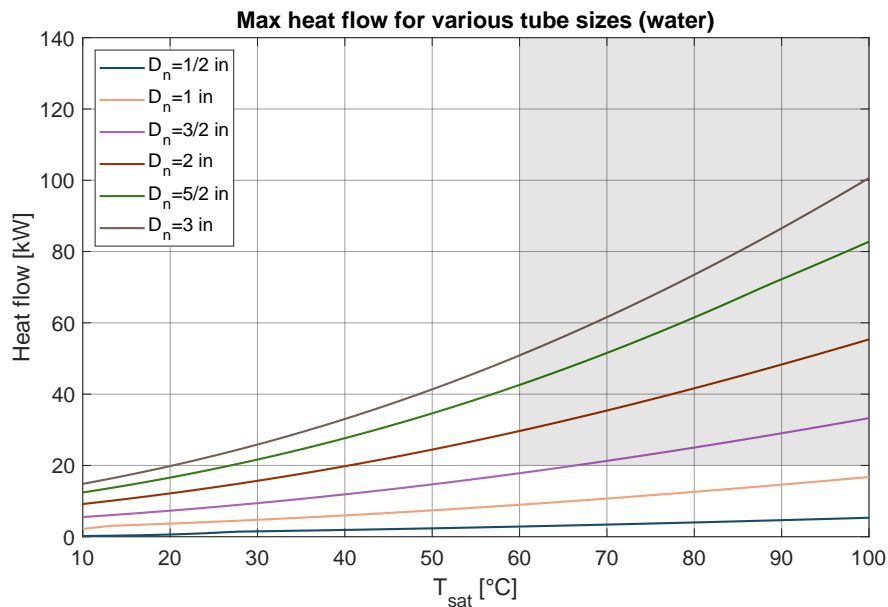


Figure 23: Limit to heat flow, combined from section 3.1.2.1, at various nominal tube sizes for a water-filled heatpipe, using $L_h = 10D_i$. All lines within the shaded area in the figure meet the requirement for the relevant geothermal temperature range.

This work however argues for the heat transfer limits listed in section 3.1.2.1, deviating from the limits used in the work of Hogendoorn and Zijm.[33], [54] Figure 23 shows a superposition of the upper limits to heat flow listed in section 3.1.2.1 for various common tube sizes. Please note that during the analysis resulting in figures 23 and 24, a conservative estimation of the critical Weber number ($We_c = 1$) has been used. As can be seen from the figure 23, the desired heat flow of 20 kW is first found for 2 inch tubes in the desired operating temperature range ($T_{sat} > 60^\circ C$) for water-filled thermosiphons.

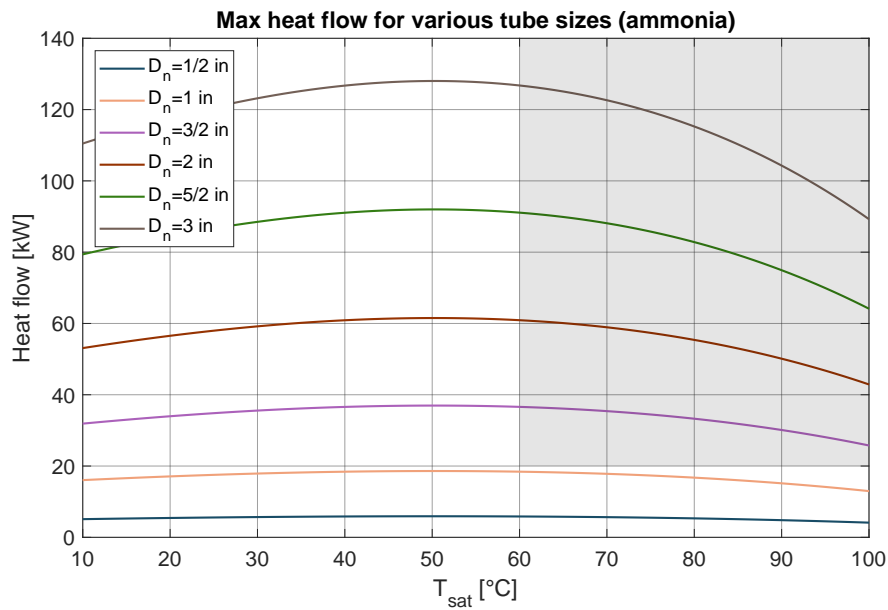


Figure 24: Limit to heat flow, combined from section 3.1.2.1, at various nominal tube sizes for an ammonia-filled heatpipe, using $L_h = 10D_i$. All lines within the shaded area in the figure meet the requirement for the relevant geothermal temperature range.

For comparison, figure 24 shows the combined heat flow limit for ammonia-filled heatpipes. The good theoretical performance of ammonia, as was discussed in section 3.1.1, justifies its inclusion in this analysis. At a constant pipe diameter, the heat flow limits for thermosiphons using ammonia as their working fluid exceeds the heat flow limits for water-filled systems. The heat transfer area required to convey a similar amount of heat per unit time is however larger for ammonia heatpipes than for heatpipes operating with water. As expected from section 3.1.1, the heat flow limits of ammonia filled systems exceed the limits of water filled systems. Within the geothermal temperature range, the entrainment limit is most restrictive for heat transfer in ammonia-filled heatpipes with conservative estimates for the critical Weber number.

As per the above, the choice for 2 inch copper tubes is acceptable for the 20 kW heat flow requirement within the operating limits discussed in this study. For the current configuration, figure 25 shows the heat transfer limits from section 3.1.2.1 separately.

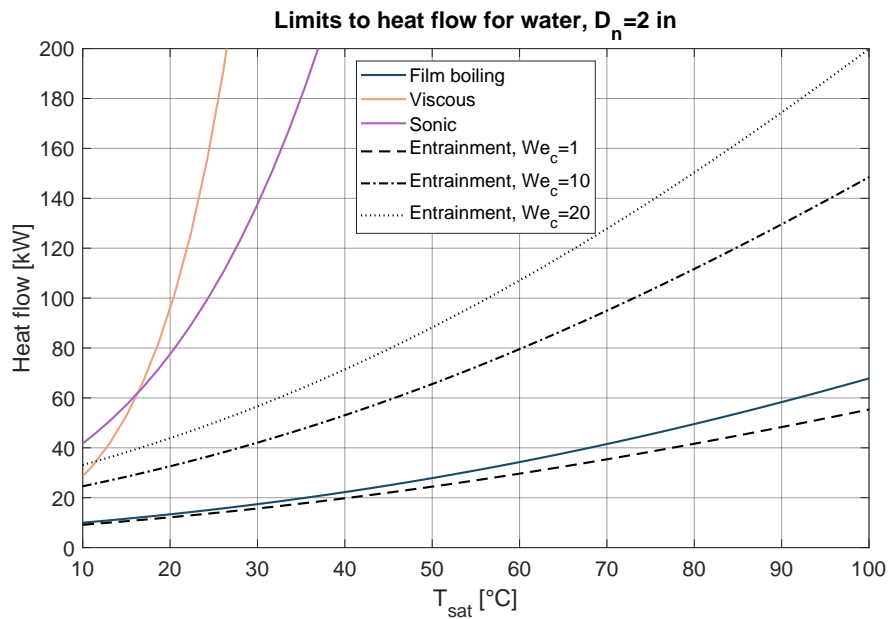


Figure 25: Limit to heat flow, as found in section 3.1.2.1, for a 2 inch water-filled copper tube, using $L_h = 10D_i$, and $L = 9$ m.

Please note that the choice for a conservative estimation of the critical Weber number We_c may result in an underestimation of the upper entrainment limit shown in figure 25. As discussed in section 2.4.3, critical Weber numbers were found to vary in a range of $1 < We_c \leq 20$. Figure 25 shows that the selection of a value for the critical Weber number has a significant effect on the prediction of the limit to heat flow by entrainment. For critical Weber numbers in the upper half of this range, entrainment is no longer the most limiting factor to heat flow in the experimental heatpipe set-up.

As discussed in section 3.1.2.1, film boiling is limiting only for heatpipes with limited boiling areas. In heatpipes intended for geothermal use, the heat exchange area is significantly larger than for lab-scale setups. With this, the limit to film boiling in full-length geothermal heatpipes may greatly exceed the limit to film boiling in an experimental setting. Furthermore, the additional adiabatic section length of a geothermal solution with respect to the experimental apparatus may result in a greater limitation by viscous friction. Figure 26 shows the limit to heat flow in a full-scale heatpipe, with the same cross sectional area as the heatpipe in figure 25, for geothermal use.

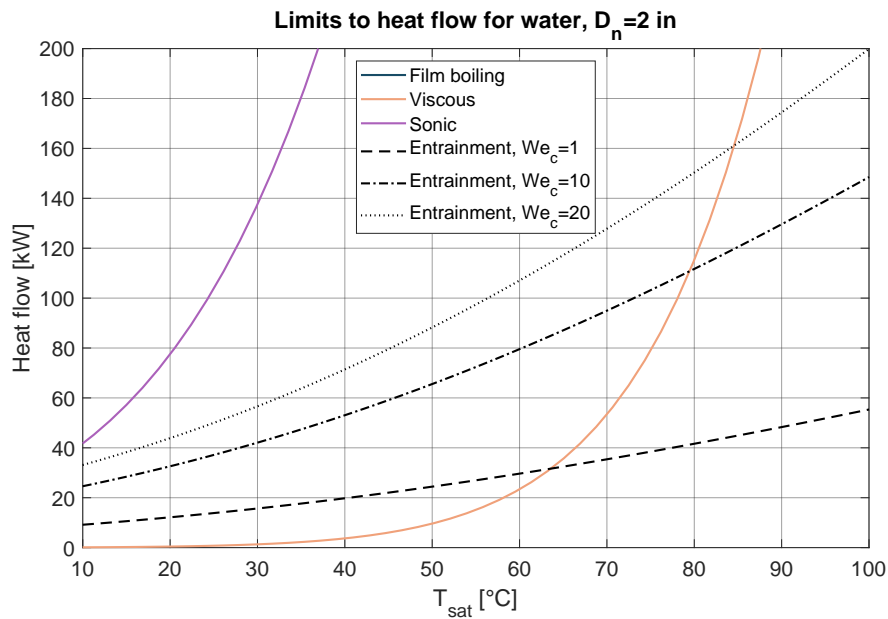


Figure 26: Limit to heat flow, as found in section 3.1.2.1, for a 2 inch water-filled copper tube, using $L_h = 25$ m, and $L = 2000$ m.

With the significant increase in the film boiling limit, the maximum allowable heat flow increases for a great range of saturation temperatures. As expected, viscous effects will limit the heat flow for moderate and low saturation temperatures.

3.1.3 Experimental evaporator

The following paragraphs discuss the evaporator of the heatpipe, in which heat is added to the system.

3.1.3.1 Heating

Heat is supplied to the evaporator through a series of cylindrical band heaters clamped to the outside surface of the copper evaporator tube. The electric band heaters used in the experimental setup [A4] have a height of 0.051 m, a heating intensity of $1.5 \cdot 10^5 \frac{W}{m^2}$ (according to the manufacturer), and a maximum heat flow of $\dot{Q}_{max} = 1200W$ per band heater. The band heaters are laced with a network of thin, long electrically resistive wires. As an electrical current is applied to the wires, heat is produced (joule heating). The degree of heating homogeneity provided by the band heaters to the system is determined by the wire distribution in the heaters. Infrared imaging in the work of Hogendoorn [33] shows inhomogeneity over the height of the band heaters, with two distinct temperature hotspots at approximately 15 mm from the heater edges, and homogeneity in the circumferential direction.

3.1.3.2 Heater inhomogeneity

In order to understand the effect of the heater inhomogeneity on evaporation in the heatpipe, a more thorough analysis of the band heaters is required. An attempt in quantifying the inhomogeneity of the heaters was performed using the sub-heater thermocouples, which are discussed in section 3.1.3.4. During the analysis, temperature transmitters were placed at set intervals throughout the heater height and circumference.

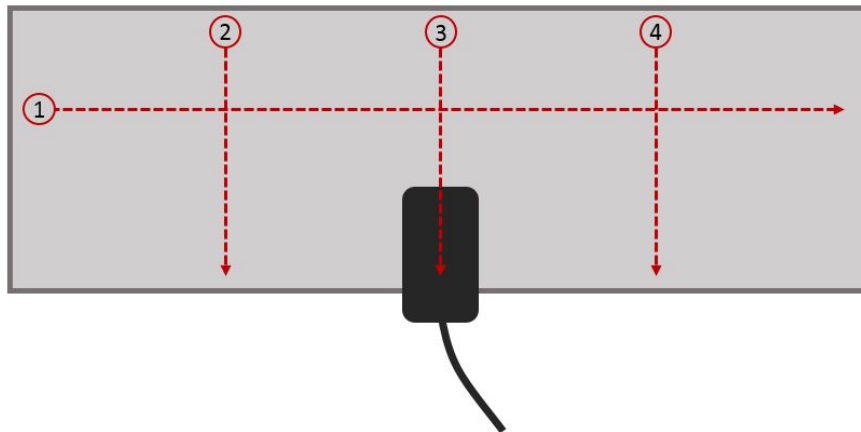


Figure 27: Schematic view of unfolded band heater. [A4] Heater depicted in grey, cable and cable attachment depicted in black. Heater homogeneity measurements indicated with red dotted lines.

For the analysis, inserts deviating from the inserts discussed in section 3.1.3.4 were used. Here, inserts with multiple probe cut-outs, with place for multiple temperature probes, were positioned between the heaters and the evaporator wall. During the analysis, the analyzed heater was used to heat a pool of subcooled water. Using the control system discussed in section 3.1.3.3, the heater was set to control the temperature of one of the temperature probes placed in the insert. Temperature transmitters were positioned along the red dotted lines indicated in figure 27, the result of which is shown in figure 28.

An initial set of diagonal measurements, not shown in figure 28, showed the presence of possible heater hot-spots at a vertical distance of 17.5 mm from the heater edges. A horizontal temperature distribution at this height, as can be seen from figure 28a, revealed the presence of two distinct higher temperature areas at 25 mm from the center of the heater. A great decrease in heater temperature near the heater edges indicates the absence of heating wires or a significant decrease in heating wire density further away from the heater center. The two hot spots shown in 28a were further investigated by measuring the heater temperature distribution along the vertical lines at both hot spot locations, lines 2 and 4 in figure 27 respectively, and along a vertical line at the center of the heater, or line 3 in figure 27. The results, shown in figures 28b, 28d and 28c respectively, show relatively similar results for the measurements along lines 2 and 4. Here, the temperature is highest and constant for some region in the middle of the heater, and decreases towards the heater edges. Please note that the measured temperatures of figure 28d deviate from the set temperature. The measurements discussed in this section were performed prior to the proper tuning of the control system discussed in section 3.1.3.3. With this, the process temperatures could deviate from their set values, without the correct intervention of the control system. Figure 28d does however provide one with insight on the temperature distribution along line 4 of figure 27. Figure 28c, however, shows a considerable decrease in temperature towards the cable housing of the heater. The above indicates the absence of heating wires near the cable housing.

The heating density of electrical band heaters locally depends on the density of heating wires in the heater. The results shown in figure 28 indicate that no heating wires are present in the proximity of any heater edges. Large heating zones exist in the proximity of heating lines 2 and 4, as is shown in figures 28b and 28d. Little heating wires are placed at the cable housing, leaving the adjacent area with a lesser heat flux than in the heated areas along lines 2 and 4, resulting in a lower temperature in the middle of the heater than in the area some distance from the center, as can be seen in figure 28a.

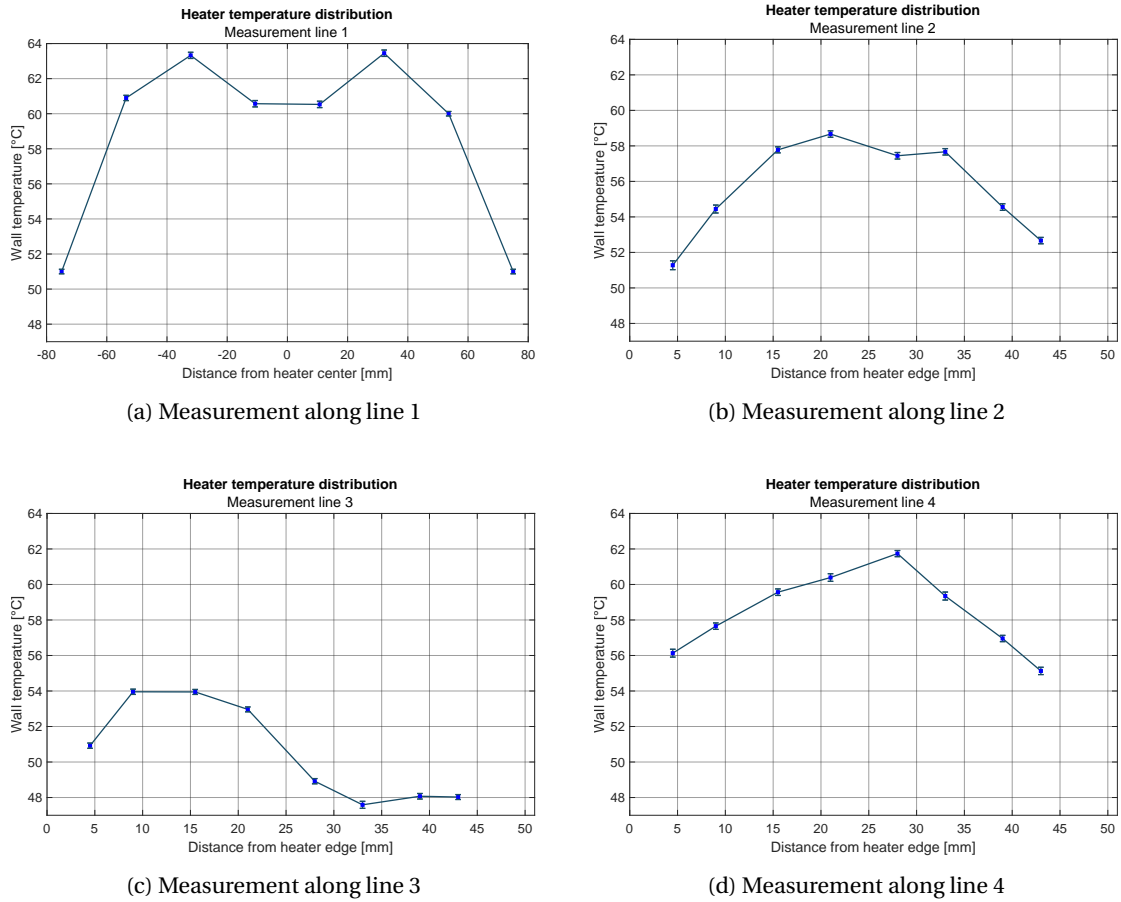


Figure 28: inhomogeneity measurements for band heaters, along lines indicated in figure 27. For all measurements, $T_{\text{set}} = 50^\circ\text{C}$.

3.1.3.3 Heater placement & control

As a large fraction of the measurements proposed in section 3.3 only considers the liquid film in the heat-pipe, the evaporator is divided in two separate zones. The pool boiling zone consists of the bottom four heaters, in which all heaters are "submerged" in a liquid pool. The bottom heaters are used to either control the saturation temperature by increasing the liquid evaporation rate, or to manually adjust the total heat flow rate through the evaporator. The bottom heaters are controlled using a RKC RB100 controller [A5]. Here, the saturation temperature, originating from TT_{sat} (see section C.2) is fed to the controller as the process variable. The output, the power sent to the band heaters, is either manipulated manually or by the controller. By altering the pulse width of the outgoing current, the time-averaged power to the heaters is adjusted. Instantaneously, however, the power to the heaters is always either at its maximum (1200 W for each band heater), or at its minimum (0 W). Thermocouples placed under the heater sheath (see section 3.1.3.4) are used as alarm values for the control system. Beyond some local wall temperature, the system will decrease the power to the band heaters.

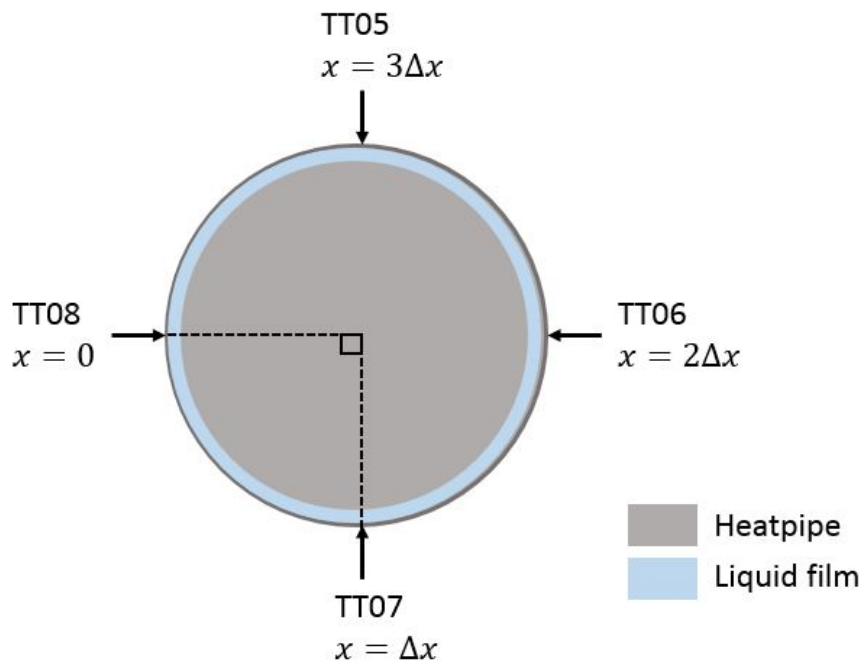


Figure 29: Schematic top view of film section of evaporator. Figure indicates temperature transmitter placement and height x with respect to the top heater, with distance x increasing towards the bottom of the evaporator.

The film heating zone consists of the top four band heaters. In order to, to some degree, sense inhomogeneities in the liquid film, thermocouple probes are aligned as shown in figure 29. Here, thermocouples are placed in equidistant tangential intervals for successive heaters. The readings from the thermocouple temperature transmitters are used as process variables for a multi-zone RKC MA901 controller.[A6] The four heaters are controlled independently, as a set point can be set for each heater. The controllers have been set for tight temperature control during film evaporation and boiling in the film section of the experimental setup, in the absence of any film dry-out. The controller settings remain unaltered throughout the study. Similarly to the RB100 controller, the outgoing pulse width is manipulated. Were the liquid film to dry out locally near one of the temperature probes, the wall temperature will rapidly increase as the heat transfer rate decreases significantly, followed by a decreasing output signal by the temperature controller. As such, intermittent (frequent, smaller temperature spikes) and permanent (significant, longer temperature spikes) can be detected during measurements.

The controller settings have been adjusted for tight control of the temperature of the film heaters within the relevant operating range. Any data originating from the controllers and transmitters is logged using Specview.[66] Here, a user-set graphical environment allows for the manipulation of controller settings and the visualization and logging of any results originating from measurements.

3.1.3.4 Heater thermocouples

The band heaters fitted to the experimental apparatus [A4] contain thermocouple temperature transmitters, mounted to the outside heater surface. The temperature transmitters do however not give similar temperature readings for a set film temperature in the heatpipe. Furthermore, as the transmitters have been mounted on the outside heater surface, little is known about the inside wall temperature of the evaporator. The thermocouples and the inside wall are separated by four thermal resistances, of which two unpredictable contact resistances. Ideally, one could avoid the additional resistances by measuring the exterior wall temperature directly adjacent to the heater. As a result of the inhomogeneity of the band

heaters, as discussed in section 3.1.3, the temperature at the outer ring of the evaporator may vary significantly from the temperature at the outermost heating wire of the heater. An attempt in quantifying this temperature difference for the nucleate boiling region is shown in figure 31. Here, the evaporator wall surrounding a heater hot-spot has been modeled as a fin, whilst assuming steady state heat transfer. When assuming a homogeneous heater temperature in the circumferential direction and assuming an adiabatic outside wall, the fin energy balance of figure 30 is found for a slice in the axial direction with length Δx .

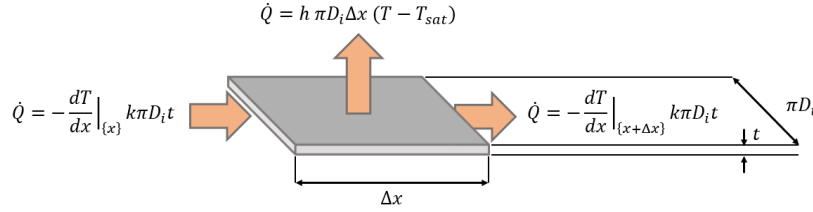


Figure 30: Approximation of energy balance over unheated section of evaporator wall section during nucleate boiling.

For an infinitesimal slice the energy balance reduces to equation (52).[8] At the heating wire ($x=0$) the temperature of the fin is equal to T_h . At some distance $x = L_{fin}$, the fin will have neared film temperature T_{sat} , and the local temperature gradient will be negligible, or $\frac{dT}{dx} \approx 0$. As such, the temperature profile in the evaporator wall with increasing distance x from a heater for a sufficiently large section of wall not surrounded by other heaters is denoted per equation (53). Probable heater- ($T_h = 100^\circ C$) and saturation temperatures ($T_{sat} = 70^\circ C$) have been considered for the analysis.

$$\frac{d^2 \theta}{dx^2} - \left(\frac{h}{kt} \right) \theta = \frac{d^2 \theta}{dx^2} - \beta^2 \theta = 0, \quad \theta = (T - T_{sat}) \quad (52)$$

$$\frac{T - T_{sat}}{T_h - T_e} = \frac{\cosh(\beta(L_{fin} - x))}{\cosh(\beta L_{fin})}, \quad \beta = \left(\frac{h}{kt} \right)^{\frac{1}{2}} \quad (53)$$

In equation (52), heat transfer coefficient h is a function of the local temperature difference and is therefore nonconstant. The heat transfer coefficient has been modeled using the nucleate boiling equation of Shiraishi et al.[29], previously discussed in section 2.1.2.3. For a copper evaporator wall, and a reference section of $L_{fin} = 0.1 m$ the temperature of the evaporator wall with increasing axial distance from the evaporator within the applicable range of the nucleate boiling heat transfer coefficient formula is as per figure (31).

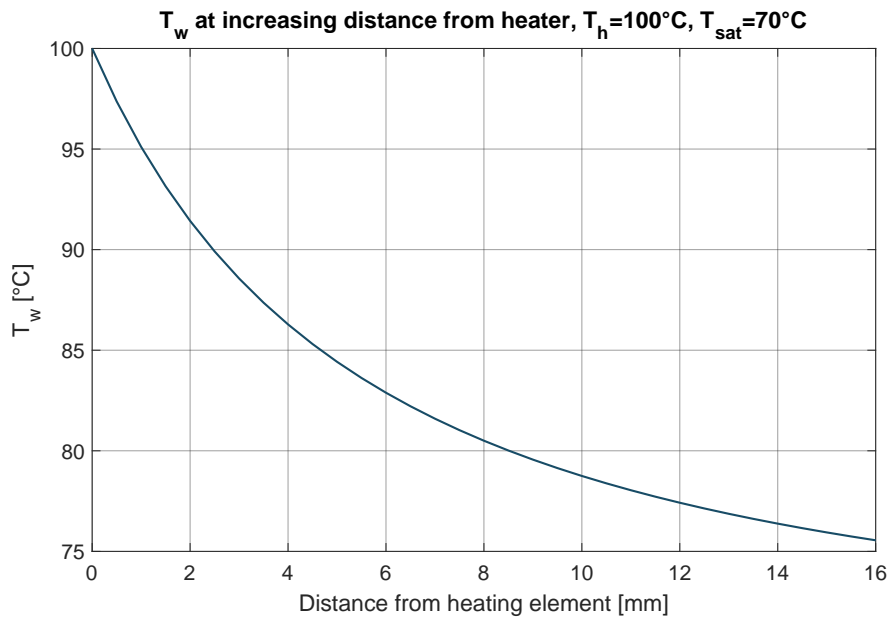


Figure 31: Temperature decrease of copper evaporator wall with increasing distance from heating element, assuming the Shiraishi[29] nucleate boiling heat transfer coefficient within its applicable range.

The wall temperature is found to significantly decrease with increasing axial distance from the heater hot-spot. As a result, temperature measurements adjacent to the heaters may not yield accurate representations of temperatures at heating wire locations, as the heater hot-spots are at some distance from the heater edges.

A measurement configuration is therefore proposed, in which temperature probes are inserted between the heaters and the evaporator walls. The probe is surrounded by an aluminium ring of the same thickness as the probe with a cutout for the transmitter, allowing for a more seamless interface. As the space between the heater and the evaporator tube is limited, thin (0.5 mm) thermocouple transmitters have been chosen [A8].

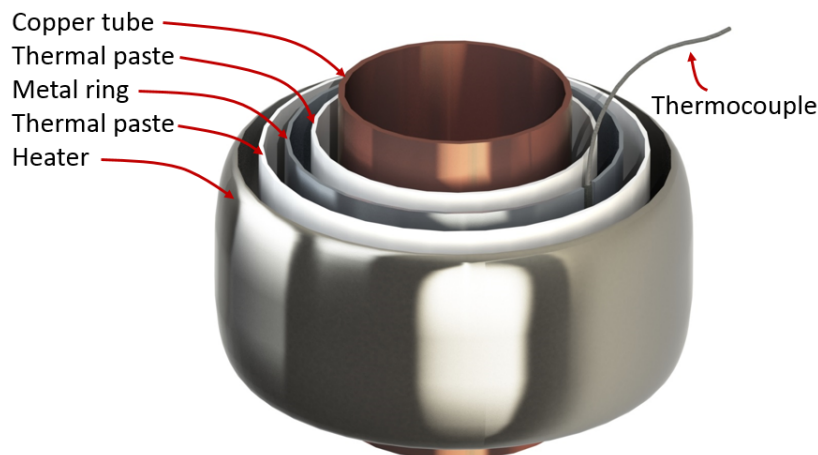


Figure 32: Exploded view of heater and temperature probe assembly, not to scale. Thermal paste depicted in white.

Figure 32 depicts the sub-heater temperature transmitter assembly. Here, any dimensions have been

exaggerated for the sake of clarity. The solid-solid contact cavities are filled with thermal paste [A7] (depicted in white in figure 32) to decrease the magnitude of any interfacial resistances, as previously described in section 2.1.4. The thermocouple probes are inserted in one of the two heater hot spots, as found from the analysis presented in section 3.1.3.2. Probes are placed at a vertical distance of 25.5 mm from the heater edges, at 30 mm from the centers of the band heaters.

3.1.4 Highlighted components

Any relevant (sub-)components of the experimental system, not previously mentioned in the previous sections, are described in the following paragraphs. The calibration of any of the sensors used in this work is discussed in Appendix III: Sensor calibration.

3.1.4.1 Experimental condenser

In the condenser, heat is extracted from the heatpipe. In order to create a condensate film that covers the entire interior surface of the heatpipe, a tube-in-tube type heat exchanger has been chosen for the experimental apparatus. In such exchangers, a stream of fluid propagating in an outer cylindrical cell removes heat from the heatpipe wall through forced convection. As such, an almost even amount of heat can be removed in the circumferential direction of the condenser. In the experimental setting, the condenser offers countercurrent flow, as the fluid in the outer shell is pumped upwards. Both the temperature of the cooling water inflow (through recycling) and its massflow can be adjusted in the condenser. The annular heat exchanger stems directly from the work of Hogendoorn.[33]

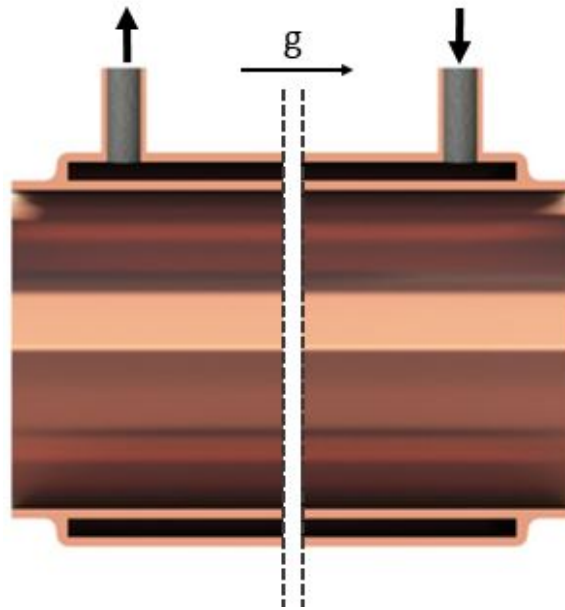


Figure 33: Cross-sectional view of experimental condenser, not to scale.

Figure 33 schematically depicts the condenser.

3.1.4.2 Insulation

A layer of insulation is applied to the exterior of the heatpipe to increase the resistance to heat flow in the outward radial direction of the heatpipe, in order to minimize heat losses to the surroundings. In a comparison of commercially available tube insulation materials in the work of Hogendoorn, a 40 mm thick rock wool insulation sheet coated with aluminum foil [A1] has been deemed most fit for the experimental heatpipe.[33] In this section, an attempt on the quantification of the heat loss through the insulation

layer is made.

When neglecting interfacial resistances (section 2.1.4), neglecting the conduction resistance through the aluminum coating layer, and assuming unforced air flow in the heatpipe surroundings, the resistance scheme of equation (54) can be used to approximate the resistance of the rock wool insulation layer covering the heat pipe. The equation denotes the sum of thermal resistances between the heatpipe interior wall and the surroundings. With increasing radial distance from the interior wall heat flows through the cylindrical tube wall ($R_{c,t}$), and the cylindrical insulation layer ($R_{c,i}$). Between the outside reflective surface of the insulation and the surroundings, heat is exchanged in parallel through natural convection (R_{nc}) and radiation (R_{rad}).

$$\Sigma R = R_{c,t} + R_{c,i} + \frac{R_{nc}R_{rad}}{R_{nc} + R_{rad}} \quad (54)$$

$$R_{c,x} = \frac{\ln\left(\frac{r_2}{r_1}\right)}{2\pi k_x L}$$

$$R_{rad} = \frac{1}{h_{rad}A_e}, \quad h_{rad} \approx 4\epsilon\sigma T_m^3$$

$$R_{nc} = \frac{1}{h_{nc}A_e}, \quad h_{nc} = \frac{k_{air}}{L} \left(0.825 + \frac{0.387Ra_L^{\frac{1}{6}}}{\left(1 + (0.437/Pr)^{\frac{9}{16}}\right)^{\frac{8}{27}}} \right)^2$$

The conduction resistance in cylindrical shells $R_{c,x}$ is found from assuming constant heat flux with increasing radial distance in the cylinder.[8] Assuming the surroundings can be modeled as a large black body, an expression for the radiation heat transfer coefficient h_{rad} can be found as a function of the mean temperature T_m .[8] Temperature T_m is the mean of the temperature of the emitting body T_a (aluminum foil surface) and the temperature of the surroundings T_∞ . An expression for the space mean heat transfer coefficient for natural convection h_{nc} can be found in the work of Churchill et al.[67] Here, an empirical formula is defined for heat transfer through natural convection on an isothermal vertical structure over a broad range of Rayleigh- ($Ra_L = \frac{g\beta(T_a - T_\infty)L^3}{\nu_{air}\alpha_{air}}$) and Prandtl numbers. As per the above, both the radiation resistance and the natural convection resistance are a function of exterior temperature T_a , an unknown entity in equation (54). A value for T_a can however be found iteratively, by first solving equation (54) with an initial guess for T_a , and assuming constant heat flow in the radial direction. Figure 34 depicts the magnitude of the individual resistances to heatflow, as described in equation (54), with increasing interior temperature. Any material properties have been retrieved from the Granta EduPack material database.[68] Air properties were acquired from the NIST database.[6]

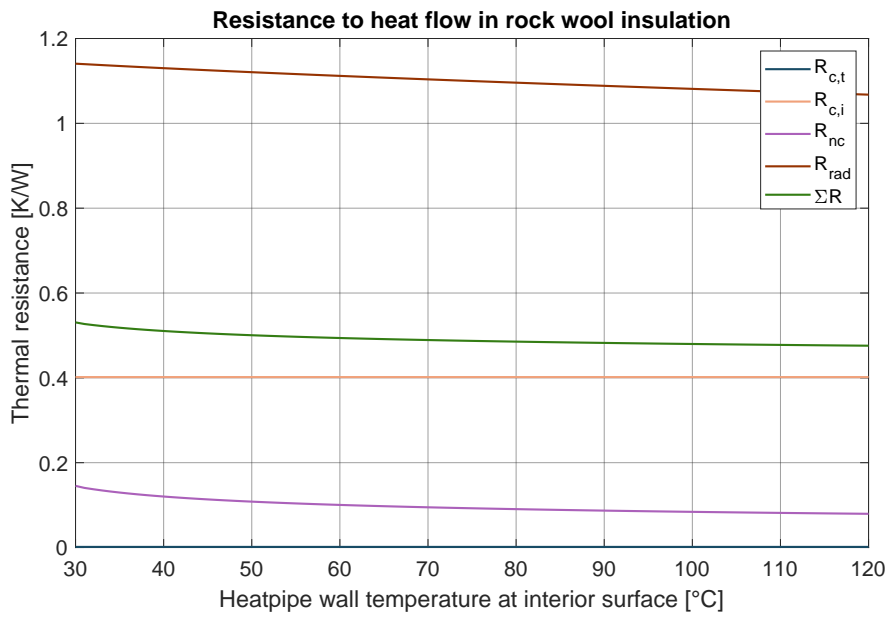


Figure 34: Resistance to heat transfer in insulation, with increasing interior surface temperature.

As per figure 4, the greatest contribution to the equivalent heat flow resistance ΣR is found from conduction through the insulation cylinder. Please note that the conduction resistance through the tube wall $R_{c,t}$ attains negligible values compared to the other thermal resistances of equation (54), for both borosilicate glass sections and for copper tube sections. The difference in heat loss through insulated sections of both respective tube material sections is therefore insignificant.

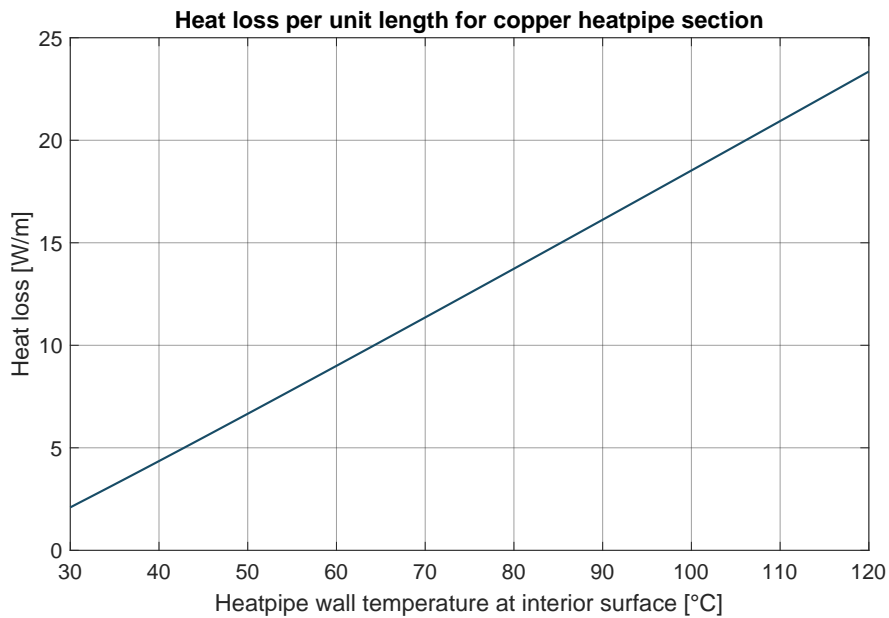


Figure 35: Loss of heat heat flow through insulation per unit height of heat pipe, with increasing interior surface temperature.

Please note that figure 34 shows that the resulting heat transfer resistance ΣR is almost temperature invariant. As such, an almost linear increase in heat loss is expected with increasing interior temperatures. Figure 35 depicts the heat loss per unit length of a heatpipe insulated with aluminum-foil-coated stone

wool, with increasing interior surface temperature of the heatpipe wall. For both figure 34 and figure 35, an exterior temperature T_{∞} of 20°C was assumed. Please note that in full-scale geothermal settings, the sink temperature varies with depth. As a result, a greater amount of heat will be lost in more shallow sections of the heatpipe, where the temperature difference between the heatpipe interior and the soil is great.

3.1.4.3 Tube connectors

The experimental heatpipe is erected from flangeless glass- and copper pipe sections. As such, couplings are needed to connect successive pipe sections. During operation, the temperature of the heatpipe increases. As a result, assuming the heatpipe is vertically fixed at the u-bolt pipe supports, the tube sections expand away from the supports towards the pipe connections. With direct contact between two pipe sections, the thermal expansion towards the connection will result in expansion induced stresses, possibly cracking the glass sections. As such, direct contact between tubes is to be avoided in the pipe connectors. Furthermore, the connectors have a sealing function, and should be able to keep air from leaking into the setup at below-atmospheric pressures. In an earlier iteration of the experimental apparatus, flexible EPDM couplings [A2] were used to connect consecutive pipe sections.[33] While these couplings did provide the system with appropriate sealing, an outward bulge was formed when fastening the connection to the tubes, allowing for the buildup of liquid in the connector. As a result, the tangential film homogeneity is lost to a degree after the fluid has passed through the connector. Furthermore, some amount of liquid previously trapped in the connector cavity would travel down the heatpipe wall periodically.

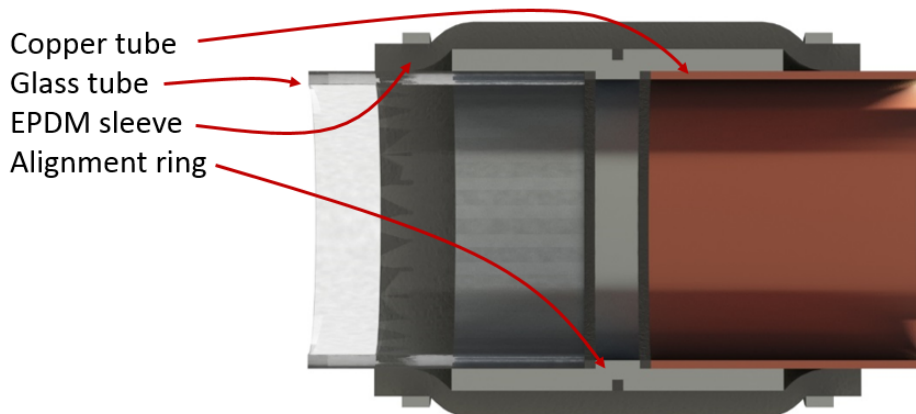


Figure 36: Cross-sectional view of tube connector.

In order to suppress the build-up of liquid in the connector, a cylindrical metal insert is placed between consecutive pipe sections. The insert, as a part of the entire pipe connector, is depicted in figure 36. The edge of this insert is lined with a flexible polymer o-ring, allowing for (a limited amount of) thermal expansion. Please note that the film is still disrupted in the above proposed connector as the gap caused by the flexible ring and the heatpipe interior is greater than the estimated film thickness. The disruption is however significantly less than in the absence of the cylindrical insert. At last, an attempt was made to replace the external seal, a polymer sleeve, with an EPDM sleeve laced with a single layer of polyester liner [A3] to provide the couplings with additional rigidity in order to combat any misalignment of subsequent tube sections. The increased rigidity of the material did however not allow for appropriate sealing.

3.1.4.4 Optical access

In order to obtain visual access to the evaporator, the bottom evaporator surface contains a glass visor. In order for light to be able to protrude towards the visor, the top of the heatpipe contains a similar glass visor. A cross-sectional view of the bottom visor assembly is depicted in figure 37. A glass holder is clamped

between a flanged tube-end and an exterior ring. As the holder contains grooves containing o-rings, the system can be sealed through clamping. A visor similar to figure 37 is positioned at the top of the heat-pipe. The top visor does however not contain a side bore.

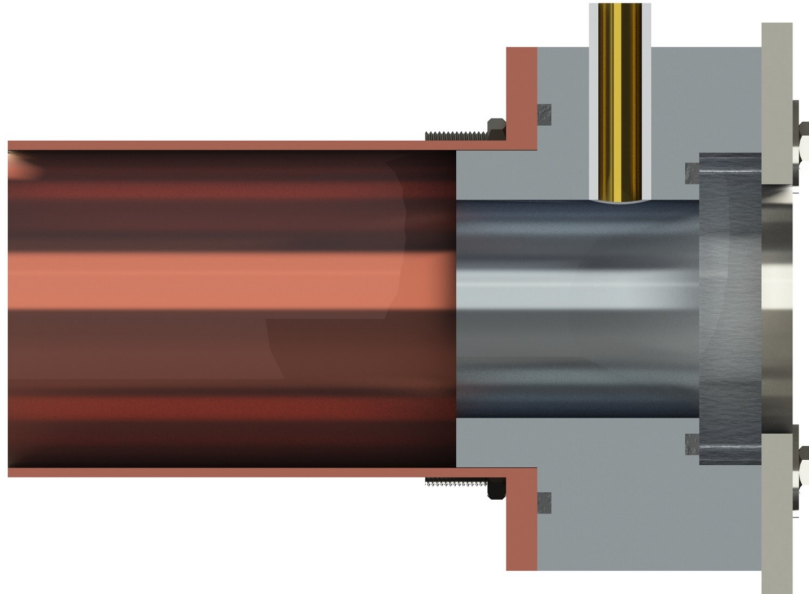


Figure 37: Glass visor assembly bottom of heatpipe, including side bore for transparent bypass.

With the addition of a light source (indicated in figure 41), aimed towards the top visor, the boiling behaviour of the evaporator can be observed through the bottom visor for sufficiently quiescent boiling conditions or sufficiently thin liquid pools.

3.1.4.5 Liquid column height

In order to differentiate between heating a fully submerged or a film-covered section of the evaporator, knowledge regarding the liquid column height is of interest. In order to not disrupt the evaporator, the liquid column height is shown using an additional transparent side stream parallel to the heatpipe evaporator. The side cylinder is erected from silicon tubing [A11], accompanied with a steel spiral insert [A12], as shown in figure 38, in order to prevent the tube from flattening whilst experiencing external pressure.

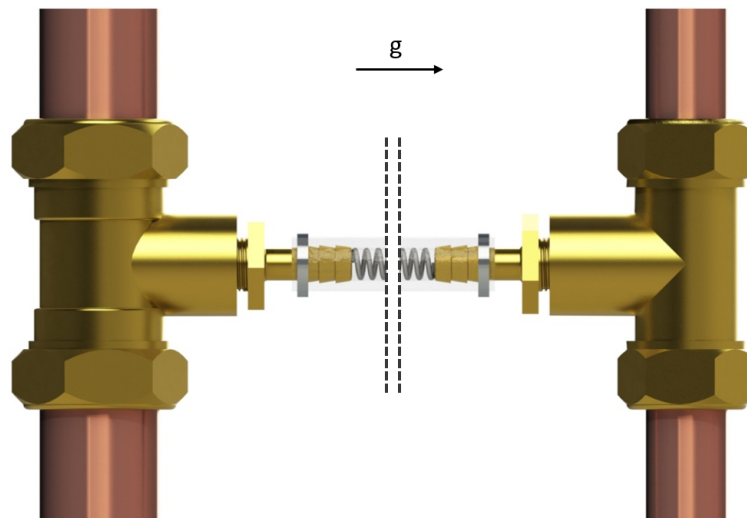


Figure 38: Transparent tube with insert, black dotted lines indicative of local shortening of tube in figure.

The side stream is connected to the evaporator at both ends. With this, the pressure in the side stream will be equal to the pressure in the main evaporator section during equilibrium. A change in pressure in the evaporator will therefore result in a change of the liquid-vapour interface height in the transparent side stream. Please note that the height of the side stream upper vapour-liquid interface will be of lesser magnitude than the height of the vapour-liquid interface in the evaporator tube as a result of the absence of vapour bubbles in the liquid column. The side stream will therefore provide the operator with (only) an estimation of the liquid column height.

3.1.5 Homogenizer

In order for the film to be evenly distributed over the inner heatpipe surface, a homogenizer is inserted into the heatpipe. The homogenizing part, a ring of foam, is placed inside the heatpipe tubing. A suitable open-celled foam has to withstand moderate temperatures (up to 100°C) for a long period of time, and the heatpipe liquid has to be preferentially attracted to the foam. Melamine foam [A13], a foam often used as insulation or for the production of magic erasers, is suitable for exposure to temperatures in the relevant operating temperature range. Furthermore, the foam contains a fine open-cell structure, suitable for capillary suction if wetting with the operating fluid. The possibility of liquid spreading for the foam-liquid pair can be investigated by placing the foam above a body of water, and allowing for contact between the foam and the liquid surface. If the liquid is preferentially attracted to the foam over air, it is drawn upwards into the matrix and the theory discussed in section 2.3.2 is applicable to the foam. A setup as per figure 39 may show a foam's preference for water over air.

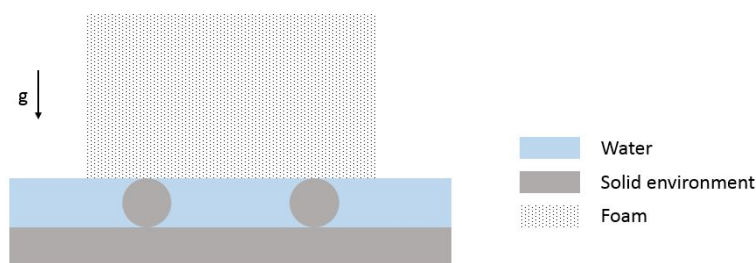


Figure 39: Schematic front view of foam suction experiment. Foam blocks are placed on top of a body of water, resting on top of cylindrical pillars. Figure is not to scale.

Preliminary measurements at conditions measured with uncalibrated temperature- and humidity sensors for a setup similar to figure 39 have shown the possibility of such preference for the melamine foam. As such, a melamine foam construction is still considered as a possible homogenization option in this study. The spreading of water in a water vapour environment with melamine foam is investigated in the heatpipe experimental setup, the results of which will be shown in section 4.

At the bottom of the homogenizer, a homogeneous film is to be offered in the absence of liquid droplets. A liquid leaving the bottom boundary of the homogenizer will form a coherent film on the wall if surface tension forces dominate the flow. If the gravity force however exceeds the surface tension force, droplets will form at the bottom of the foam. The Eötvös number describes the relative influence of gravity forces with respect to surface tension forces, and is denoted in equation (55).

$$Eo = \frac{\Delta\rho g l^2}{\sigma} \quad (55)$$

Beyond unity, surface tension forces dominate the flow. The length scale found from equating equation (55) to unity is the capillary length scale. At a thickness below the capillary length, no droplets will be formed at the bottom foam rim if the foam is placed against a wall on which a film can be formed. The capillary length exceeds 2.5 mm for a water-vapour interface within the operating temperature range of geothermal heatpipes. As such, geometrical requirements for the foam ring can be formulated. The foam homogenizer is to be in contact with the evaporator inner wall, and should have a bottom boundary thickness of below 2.5 mm.

When manipulating the melamine foam with a laser cutter, an increasing amount of foam is removed with increasing distance from the laser cutting nozzle, as is depicted in figure 40. In order to combat the impreciseness resulting from the diffusion of the laser beam in the foam, the magnitude of the deviation is investigated for various laser cut settings. Separate foam samples are cut whilst varying the beam power and the workbench velocity.

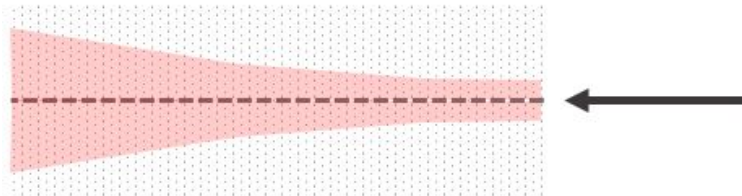


Figure 40: Schematic depiction of foam removal during laser cutting, intended cut indicated with dotted line, removed volume indicated in red, laser beam indicated with black arrow. Figure is not to scale.

With increasing power, the average diffusion of the laser beam decreases in magnitude. The amount of unwanted black residue resulting from the incineration of the foam, and the level of inhomogeneity in deviation from the projected cut however also increase with increasing power. At lower powers a more homogeneous cut is found, albeit with greater deviation from the projected cut. An additional decrease in beam diffusion is however found for increasing workbench velocities. As such, a homogenizer ring erected from melamine foam is to be laser cut at relatively low power, and high bed velocities.

If contact between the bottom outer edge of the foam ring and the inner evaporator wall is desired, the diameter of the top boundary of the ring has to exceed the inner diameter of the evaporator. As a result, an outward normal force is exerted from the ring onto the wall when placed in the heatpipe cylinder. The friction resulting from this outward normal force has been found to exceed the downward acting gravity force on a saturated homogenizer ring, for both foam-glass and foam-copper contact. As a result, no additional clamping is required to keep the homogenizer in position.

3.2 Setup overview

In this section, an overview of the experimental apparatus and its sizing is provided. A process & instrumentation diagram of the setup is shown in figure 41. Here, the location of any details discussed in the previous paragraphs is indicated. Any relevant dimensions or specifications needed for the replication of the results in this study are listed in tables 3 and tables 4 respectively.

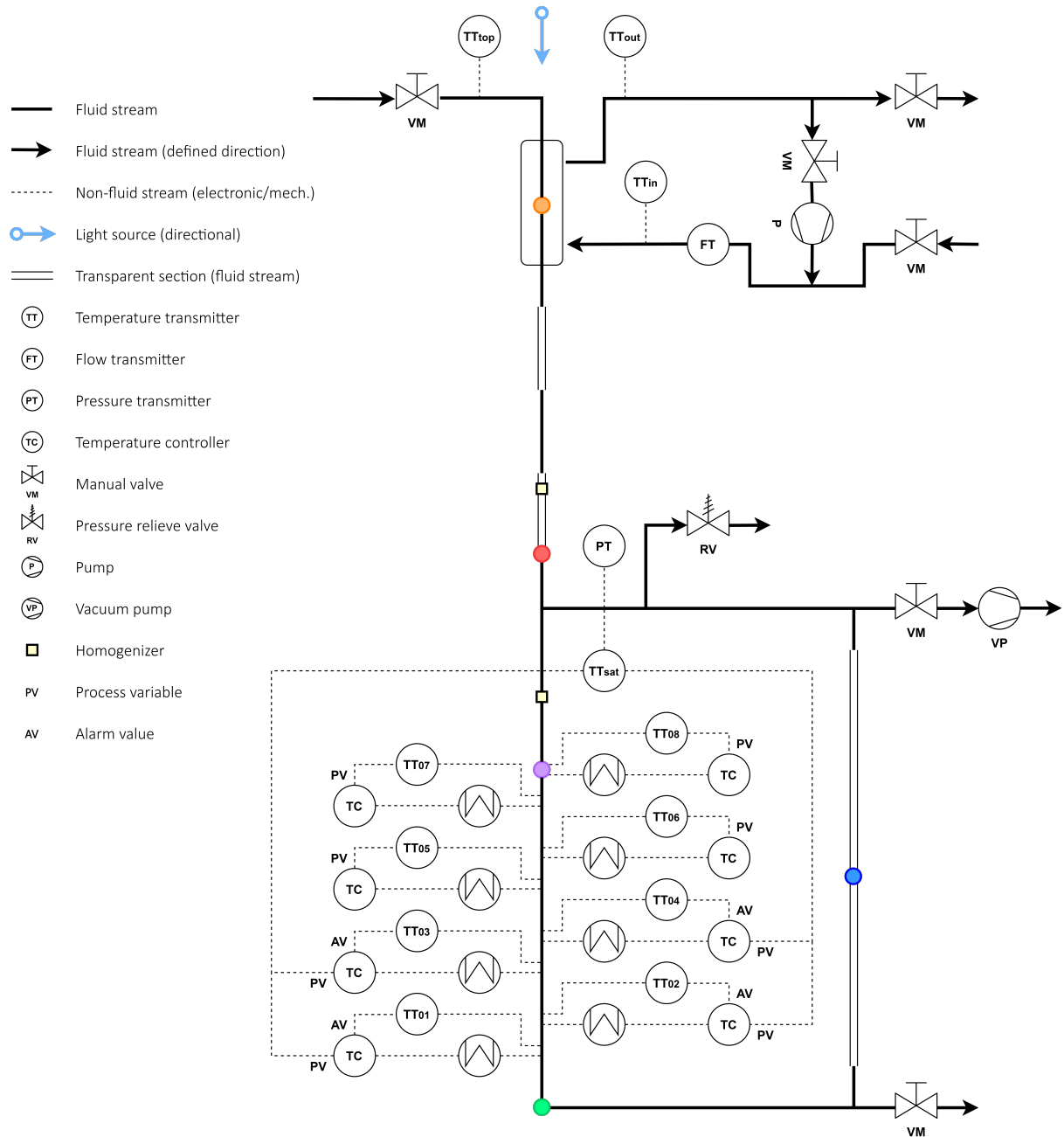


Figure 41: Process & instrumentation diagram of experimental setup. The location of figure 33 is indicated in orange. The location of figure 36 is indicated in red. The location of figure 32 is indicated in purple. The location of figure 37 is indicated in green. The location of figure 38 is indicated in blue.

Dimension	Value	Unit
Total heatpipe height	9.0	m
Evaporator height	1.5	m
Condenser height	1.5	m
Copper pipe outer diameter (main section)	54.0	mm
Copper pipe inner diameter (main section)	51.0	mm
Glass pipe outer diameter (main section)	54.0	mm
Glass pipe inner diameter (main section)	49.0	mm
Condenser shell outer diameter	62.0	mm
Condenser shell inner diameter	58.0	mm
Transparent tube inner diameter	10.0	mm
Interval top four heaters (center to center)	100.0	mm
Interval bottom four heaters (center to center)	80.0	mm
Heater height (total)	408.0	mm
Heater height (single)	51.0	mm
Homogenizer height	30.0	mm
Distance top homogenizer to visual measurement	650.0	mm
Distance bottom homogenizer to top heater	400.0	mm

Table 3: Overview of (sub)component dimensions of heatpipe assembly.

Parameter	Value	Unit
Heater power (total)	9600	W
Heater power (single)	1200	W
Cooling water flow rate (max)	2450	L/h

Table 4: General specifications of heatpipe assembly.

3.3 Measurements

The following paragraphs will aim to describe any measurements performed using the experimental apparatus. The reasoning behind and the necessity of any experiments are also discussed. All measurements have been performed with the presence of homogenizers, as indicated in figure 41, in the system. An analysis of the effectiveness of the homogenizers is proposed in section 3.3.6. Any results are shown and discussed in section 4.

3.3.1 Increasing ΔT

If the heatpipe heat extraction rate exceeds the local aquifer heat replenishment rate, the local temperature in aquifer regions adjacent to the geothermal heatpipe evaporator may decrease. As such, assuming no change in the saturation temperature of the system, the degree of wall superheating in the heatpipe evaporator decreases. The effect of a change in the degree of wall superheating on the heat removal rate of the evaporator is to be studied. In the measurements associated with this section, the value of $(T_w - T_{sat})$ for the film heaters is increased incrementally, at a constant total system flow rate and a constant saturation temperature. The top four film heaters are positioned as described in section 3.1.3.3. The bottom four heaters are used to control the total system flow rate. In order to generate the results presented in section 4.1, the heatpipe evaporator section has been insulated as discussed in section 3.1.4.2.

3.3.2 increasing initial flow rate

Film dry-out may significantly reduce the available area for heat transfer in the full-scale heatpipe evaporator. Fujita et al. reported that the formation of permanent dry-spots was prevalent at the bottom of

falling films subject to nucleate boiling.[12] At the bottom of the film, the film velocity has decreased as a result of a loss of mass. The dependency of the onset of (permanent) dry-out of an initially annular film on the initial film flow rate and the degree of wall superheating is studied in this work. In a series of measurements the initial liquid flow rate is incrementally decreased (by lowering the throughput of the bottom four heaters) at a constant value of $(T_w - T_{sat})$. The effect of the decrease in flow rate on the heat removal rate of the film heaters is presented. The measurements are repeated for various degrees of wall superheating. At all times, the saturation temperature is kept constant throughout the measurements. In order to generate the results presented in section 4.2, the heatpipe evaporator section has been insulated as discussed in section 3.1.4.2.

3.3.3 Increasing saturation temperature

As the temperature of the aquifer varies over time as a result heat extraction by the heatpipe, the total heat flow through the system may vary. A decrease in heat flow may decrease the saturation temperature in the system. The figures of merit shown in section 3.1.1 suggest a dependency of the heat removal rate on the saturation temperature. As such, the heat removal rate may decrease as a result of a decrease in saturation temperature. In this work, a series of measurements is presented in which the degree of wall superheating and the total system flow rate are kept constant, and the film heater heat removal rates are analyzed. In order to generate the results presented in section 4.3, the heatpipe evaporator section has been insulated as discussed in section 3.1.4.2.

3.3.4 Saturation temperature development

As the temperature of the aquifer varies over time, the total heat flow through the system may vary. The significance of a change in the total heat flow on the saturation conditions is studied in this work. Furthermore, the influence of a change in the cooling water flow rate on the saturation conditions in the heatpipe is presented. During the experiments the total heat transfer rate of the evaporator is incrementally increased at a set cooling water flow rate. The previous is repeated for various cooling water flow rates. Prior to the measurements, an attempt was made to remove any remaining air from the setup by boiling the water in the setup with the top valve open. In order to generate the results presented in section 4.4, the entire heatpipe has been insulated as discussed in section 3.1.4.2.

3.3.5 Heat extraction

The intended purpose of the heatpipe in a geothermal setting is to transport heat towards- and extract heat from the condenser. At the surface, an operator may only be able to adjust the temperature and the flow rate of the cooling water. During operation, however, the total heat flow rate through the apparatus may vary as a result of temperature variations in the adjacent aquifer. The results of this work will include an analysis of the extracted heat flow rate in the condenser, with varying system heat flow rates. As such, it may become apparent what can be done on the operating side of the heatpipe to maximize the efficiency of the system when the aquifer heat extraction rate decreases. In order to generate the results presented in section 4.5, the entire heatpipe has been insulated as discussed in section 3.1.4.2.

3.3.6 Homogenizer effectiveness

As a result of slight irregularities and misalignments in the experimental heatpipe, a non-homogeneous liquid film is presented to the evaporator at moderate flow rates. Here, the liquid has a tendency to flow in a single bulge or rivulet centered around the location of temperature transmitters TT₀₅ and TT₀₆. In order to redistribute the liquid prior to it entering the evaporation section of the experimental apparatus, a melamine foam ring was presented in section 3.1.5. The effectiveness of the homogenizing ring is first qualitatively discussed, with the use of images taken in the transparent heatpipe segment. Furthermore, the measurements discussed in section 3.3.1 are repeated after the removal of the homogenizer, in order to be able to quantify the effectiveness of the foam ring.

4 Results & Discussion

The results of the measurements proposed in section 3.3 are shown in the following paragraphs. Any results are discussed and compared to the theory of section 2. Please note that any experimental data that is shown in graphical form in section 4 is tabulated in Appendix II: Experimental data & Error propagation.

4.1 Increasing ΔT

The following paragraphs will show and discuss the results originating from the measurements proposed in section 3.3.1. Figure 42 shows the film heater outputs for an increasing degree of superheating of the evaporator wall, at a set saturation temperature and initial liquid flow rate.

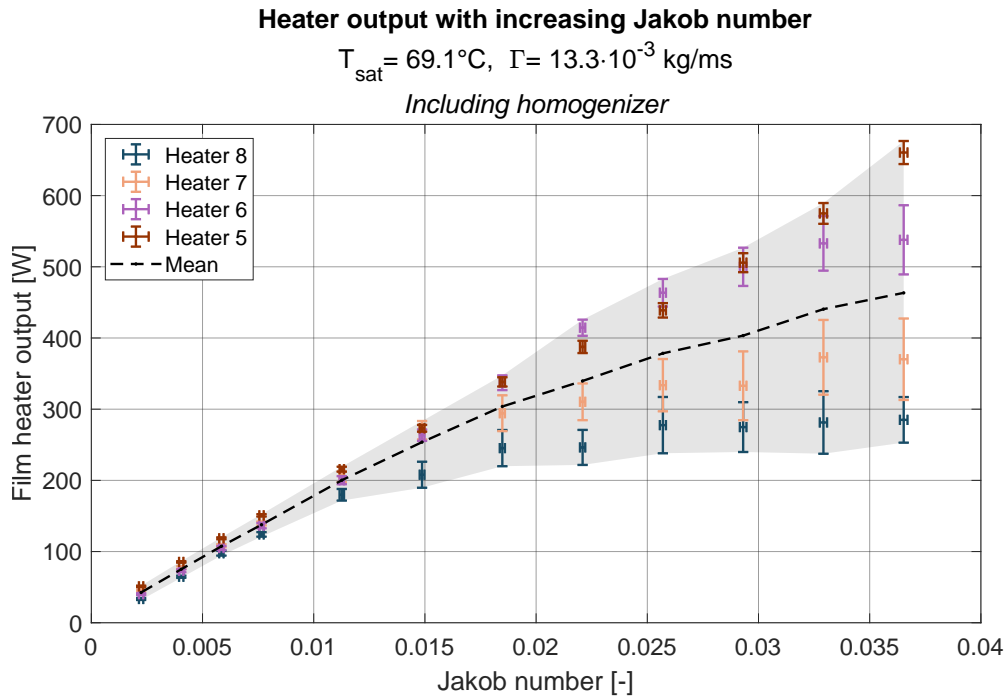


Figure 42: Heater heat removal rate for film heaters, as a function of the degree of superheating, expressed with the Jakob number ($Ja [-]$). Here, $T_{\text{sat}} = 69.1^\circ\text{C}$ and $\Gamma = 13.3 \cdot 10^{-3} \frac{\text{kg}}{\text{ms}}$. The gray area indicates the degree of spreading between the greatest ($\dot{Q}_{i,\text{in}} + u_{\dot{Q}}$) and the lowest ($\dot{Q}_{i,\text{in}} - u_{\dot{Q}}$) film heater output for some value of Ja . Data shown in figure includes 68% ($t_{v,p}=1$) confidence interval.

Figure 42 shows an increase in the mean heat removal rate with increasing ΔT , along a concave trend line. The absolute spreading in heater outputs between the four band heaters is found to increase for increasing ΔT . An evaluation of the evolution of all individual heater heat removal rates may aid in finding the cause of the concave trend. At low degrees of superheating ($Ja \leq 0.01 [-]$) the spreading among consecutive heaters remains limited. At some degree of superheating, the heat flow rate of heater 8 diverts from the trend followed by the other three heaters. An onset of intermittency accompanies this deviation, characterized by a greater uncertainty interval for film heater 8. With further increasing values for the Jakob number, no significant further increase in the heat removal rate for heater 8 is observed. A similar trend is observed for heaters 7 and 6. Here, the first onset of intermittent behaviour occurs at greater degrees of superheating than the first increase in intermittency at heater 8.

The behaviour in which a sudden onset of intermittency in the heat removal rate could be indicative of film dry-out of intermittent nature, as described in the work of Fujita et al.[12] Here, dry-spots resulting

from the formation of vapour nuclei result in brief temperature spikes, with subsequent rapid rewetting of the dry-patches. As per the theory of section 2.1.2.1, the rate at which nucleate bubbles form and the area for which nucleation sites are activated increase with increasing degree of superheating. If the degree of superheating is further increased after the onset of dry-out, the area of film dry-out will increase as a result of the increased presence of vapour nuclei. As such, an increase in the heat transfer rate with further increasing degrees of superheating may be suppressed by an increase of the bubble-covered area, after the onset of dry-out.

The presence of inconsistencies and minor misalignments in the experimental setup results in a tendency for the liquid film to flow in a single rivulet passing through the temperature probes under heater 5 and heater 6. As will be shown in section 4.6, the spreading of the film decreases significantly after the insertion of homogenizer rings into the apparatus. The results shown in figure 42 however suggest that although the film is put through a homogenizer, not all inhomogeneity is lost. The consecutive onset of intermittency (onset occurs at different Jakob numbers) for heaters 8, 7, and 6 suggests the presence of a circumferential variation of the liquid film thickness. With greater degrees of superheating, the disruptive influence of nucleate boiling increases, and will break up films of greater thickness.[40] As such, the later onset of intermittency for heaters 7 and 6 suggests a locally greater film thickness than at heater 8. In case of ideal homogenization, the onset of intermittent behaviour as a result of film dry-out is expected to take place simultaneously for all film heaters. A more detailed analysis of the significance of the liquid film flow rate on the onset of the intermittent behaviour is found in section 4.2.

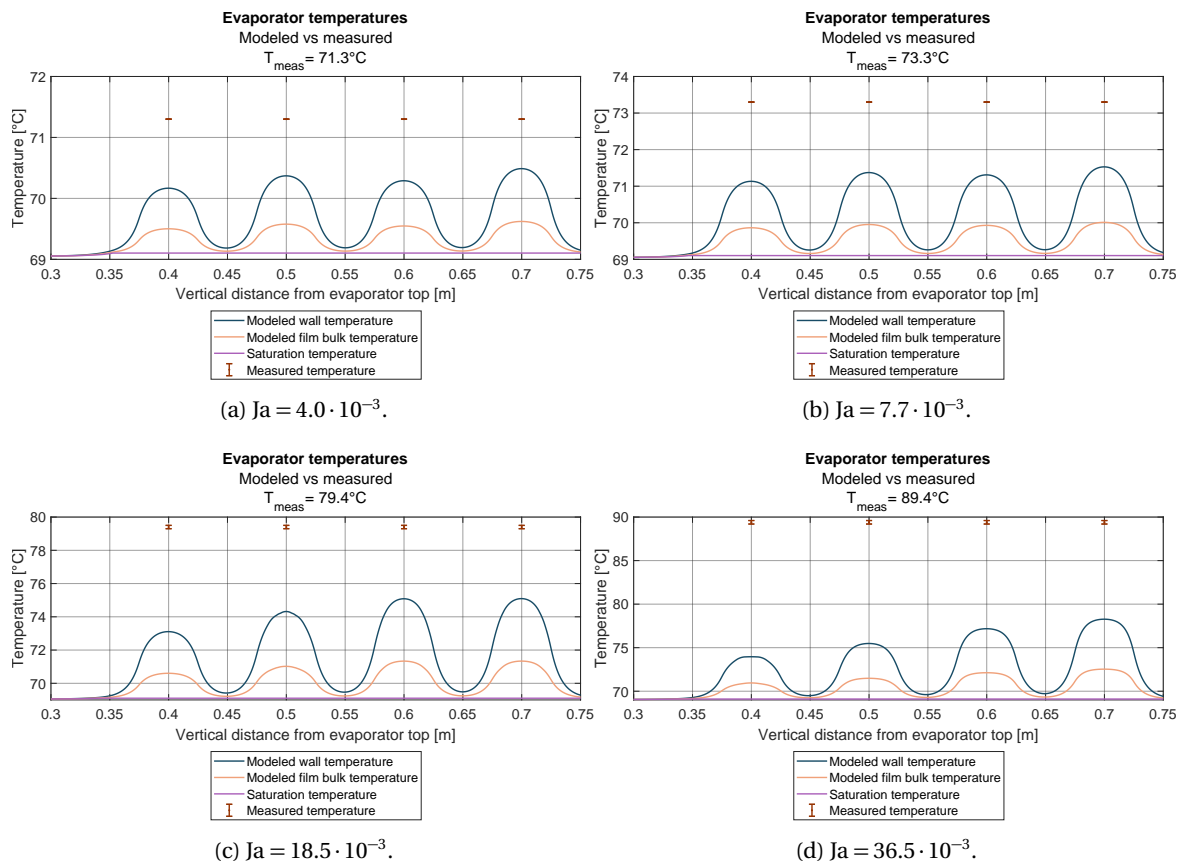


Figure 43: Comparison between data shown in figure 42 and the model discussed in Appendix V: Numerical model.

The heater output in the experimental setting is compared to the theoretical heat flow rate for a homogeneous film in figure 43. Here, the empirical formulae of section 2.1.2.3 have been used to define a

heat removal boundary for a steady state finite difference temperature grid of the evaporator wall, further discussed in Appendix V: Numerical model. Figure 43 shows a comparison of the interior heater wall temperature for the domain in which film heaters are present, for heater heat throughputs equal to the resulting heat removal rates found from several data points in figure 42. For all points of comparison, the measured wall temperature exceeds the modeled wall temperature. With increasing Jakob number, the difference between the temperatures increases. Similarly, one can compare the modeled heat removal rates with the found heat removal rates for varying degrees of superheating, as is shown in figure 44. In order to obtain the theoretical curves of figure 44, homogeneity of the heaters has been assumed.

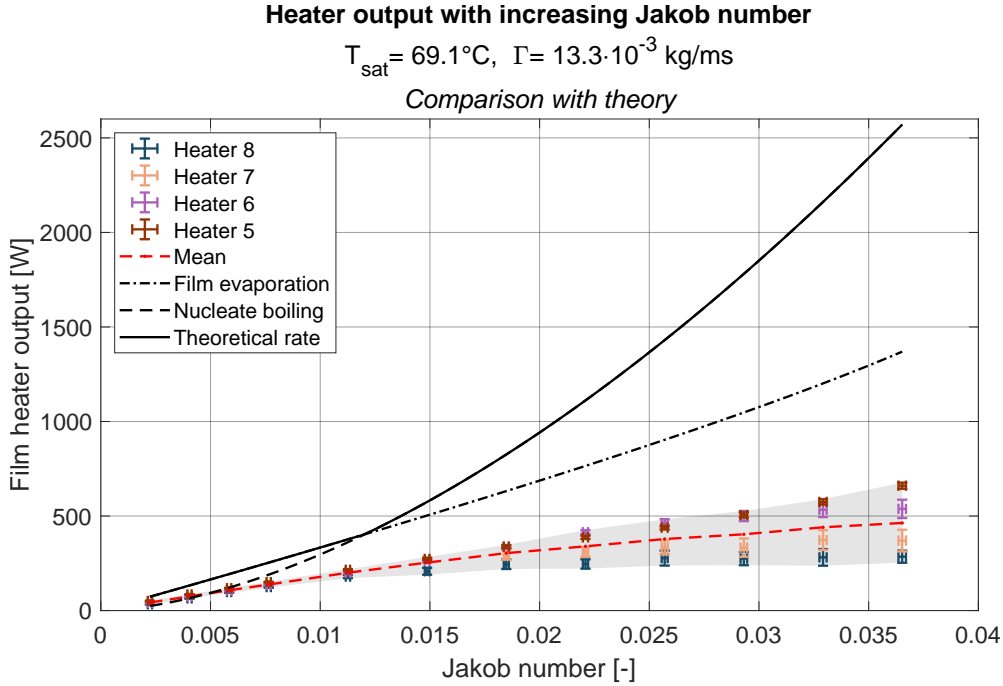
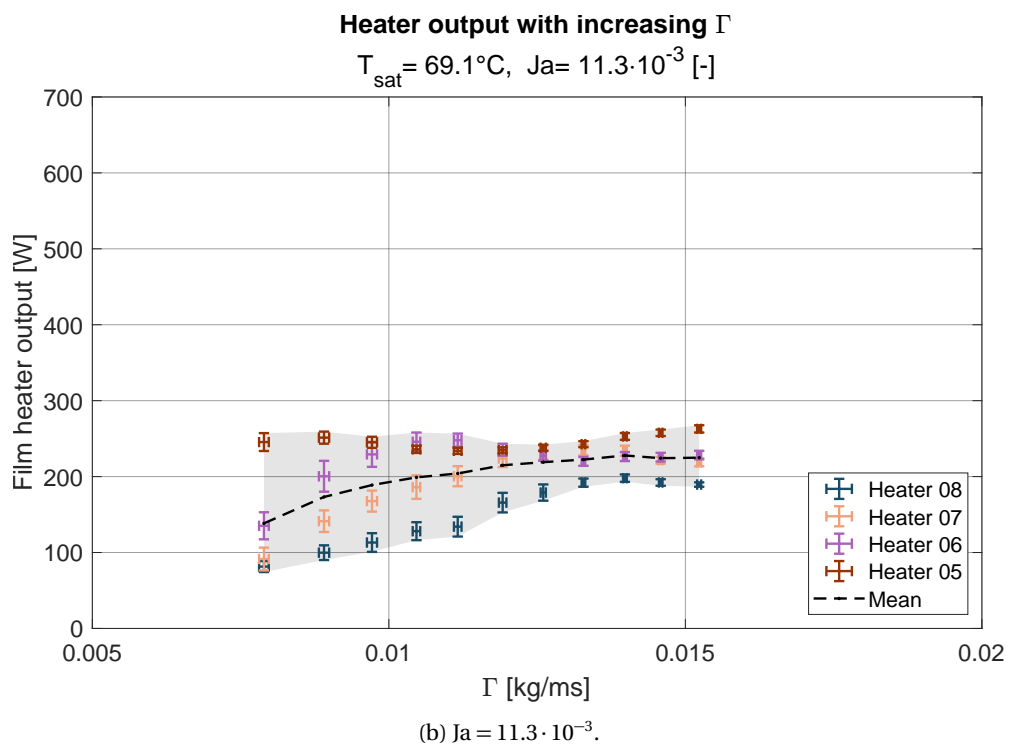
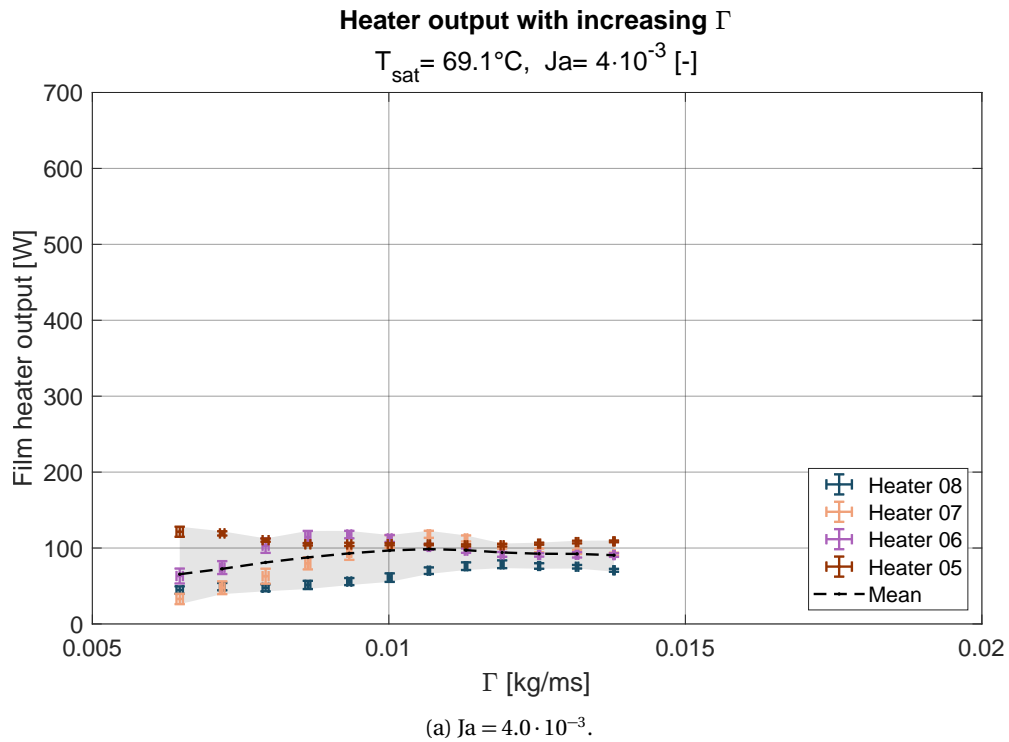


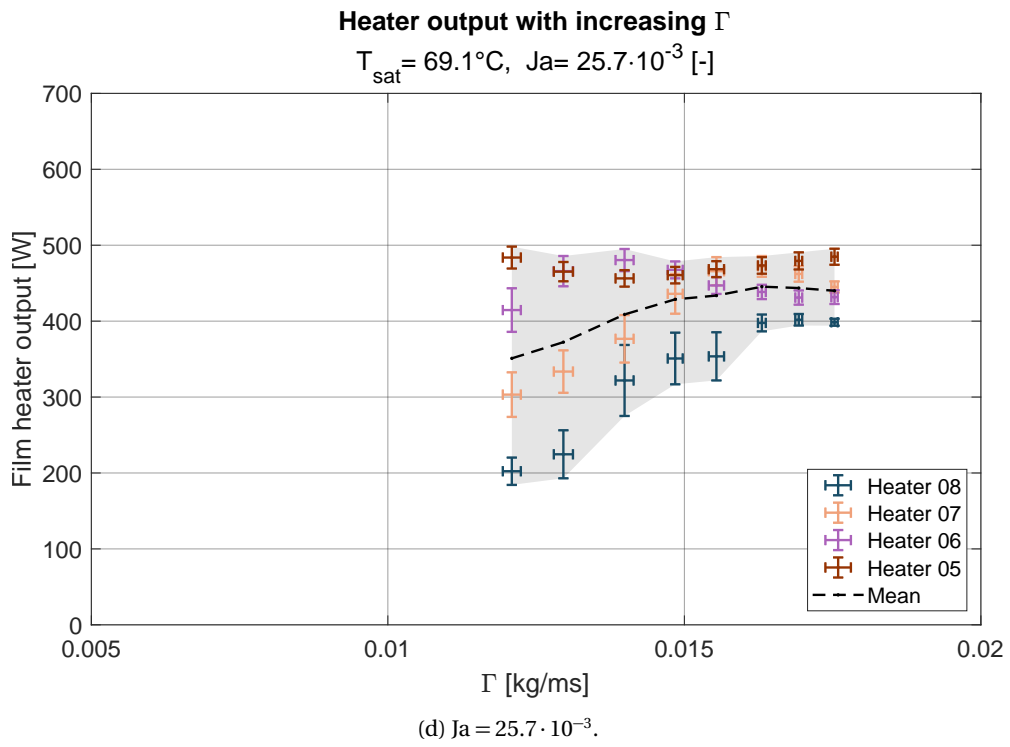
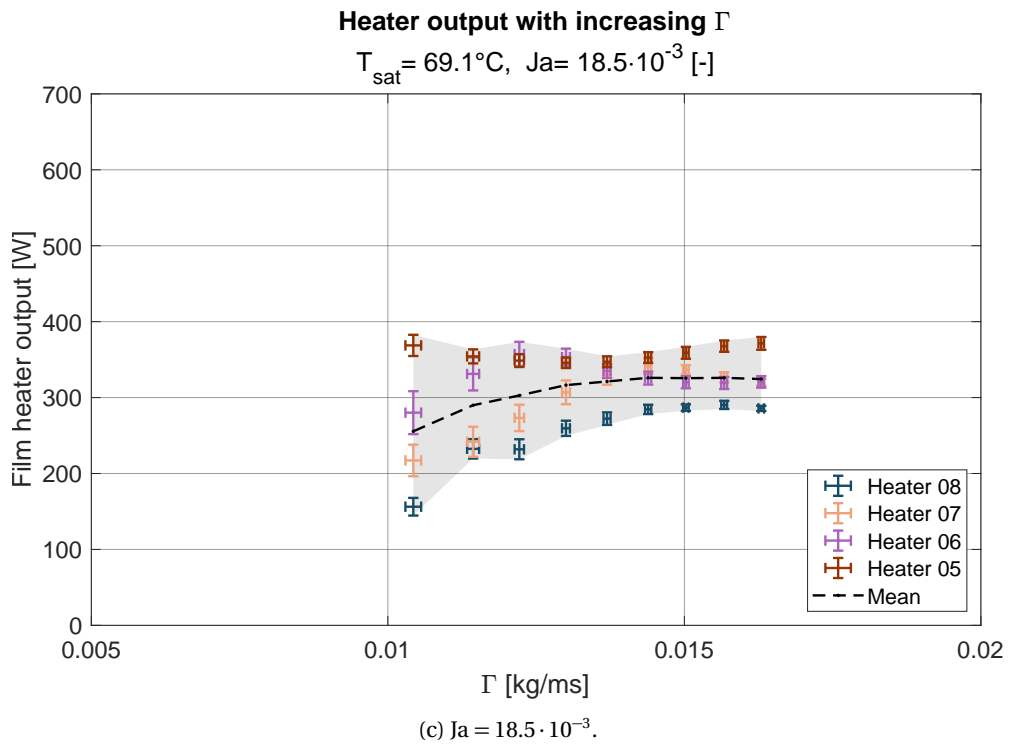
Figure 44: Comparison between data shown in figure 42 and the expected average heat flow rate for the specified Jakob number.

Here, a superposition of equations (8) and (17) is used as the theoretical reference to the heat removal rate. As previously found, the difference between the modeled and measured lines increases with increasing Jakob numbers. Furthermore, the slopes of the theoretical and measured curves appear to differ significantly. The heat removal rate can be denoted as a function of the Jakob number, i.e. $\dot{Q}_{\text{in}} \sim C \cdot \text{Ja}^n$. The theoretical curve shows an increasingly great slope with increasing values for Ja, or $n > 1$. The measurements however show a trend for which $n < 1$. Please note that the Jakob number is directly proportional to the wall temperature difference. As such, a value for n that is smaller than unity suggests that the thermal resistance of the measured film evaporation process increases with growing degrees of superheating.

In the theoretical model, the heat transfer is modeled assuming a uniform heater temperature of T_{wall} . The heater analysis of section 3.1.3.2 however showed that the heater temperature is highly heterogeneous during operation. As the temperature measurement probe is inserted at the heater hot-spot, the average heater temperature lies at a significantly lower value than the measured wall temperature. With this, the film heater output is expected to lie at values substantially lower than what is indicated by the theoretical line of figure 44. A more accurate comparison is found when correcting the measured values (decreasing the Jakob number) in figure 44 with some unknown amount. With this, little can be said regarding the validity of the heat transfer coefficient approximation by Shiraishi et al.[29] for areas with film heating using the results shown above. However, even after correcting for the actual wall temperatures, the slope of the mean heat removal rate curve will decrease with increasing Jakob numbers, and

not match the theoretical curves.





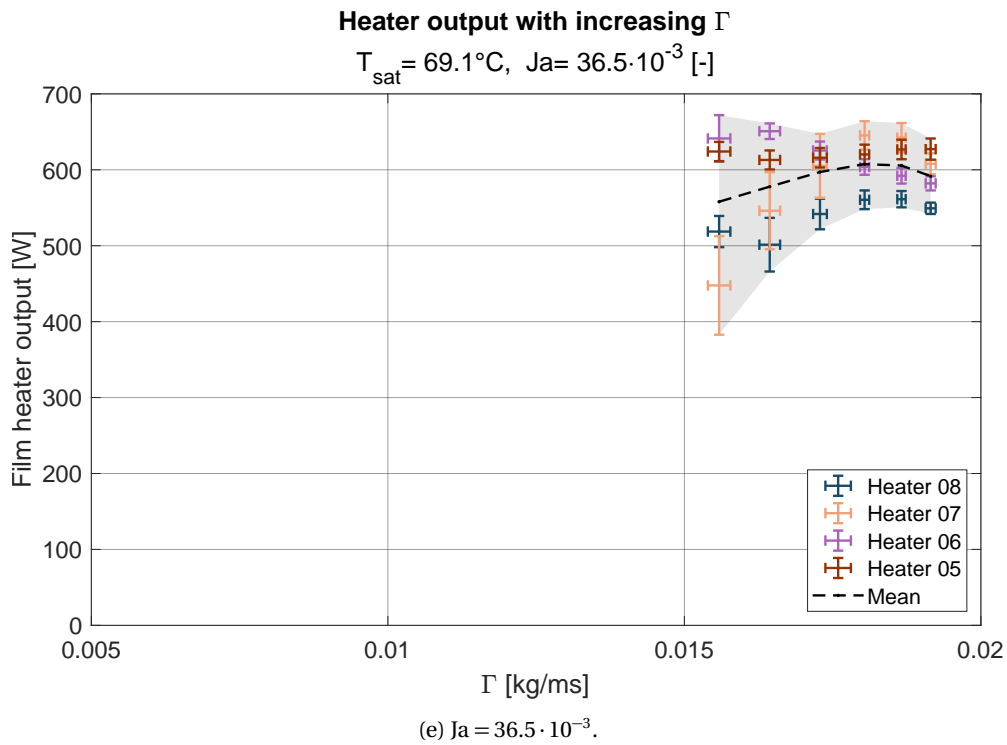


Figure 45: Film heater output at decreasing initial liquid film flow rate, for various Jakob numbers. $T_{\text{sat}} = 69.1^\circ\text{C}$, $Ja = 36.5 \cdot 10^{-3}$. The gray area indicates the degree of spreading between the greatest ($\dot{Q}_{i,\text{in}} + u_{\dot{Q}}$) and the lowest ($\dot{Q}_{i,\text{in}} - u_{\dot{Q}}$) film heater output for some value of Ja . Data shown in figure includes 68% ($t_{v,p}=1$) confidence interval.

4.2 increasing initial flow rate

The following paragraphs will show and discuss the results originating from the measurements proposed in section 3.3.2. Figure 45 shows the film heater outputs for a decreasing initial film flow rate, at a set saturation temperature for various Jakob numbers. Please note that, for the sake of comparison, all sub-figures of figure 45 have identical axes value ranges. Additional figures, in which individual data points are more clearly depicted for each separate subfigure can be found in Appendix VI: Auxiliary figures.

For the experiments of which the results are shown in figure 45, the maximum possible flow rate was first imposed on the system for the conditions listed in each subfigure. In all cases, a film (visually) free of dry-spots in the transparent section of the heatpipe was produced, with little deviation and intermittency among the respective film heater outputs. The latter is indicative of a film that is homogeneous to some degree. The total liquid flow rate (controlled with the pool heaters) was made to gradually decrease at constant saturation conditions.

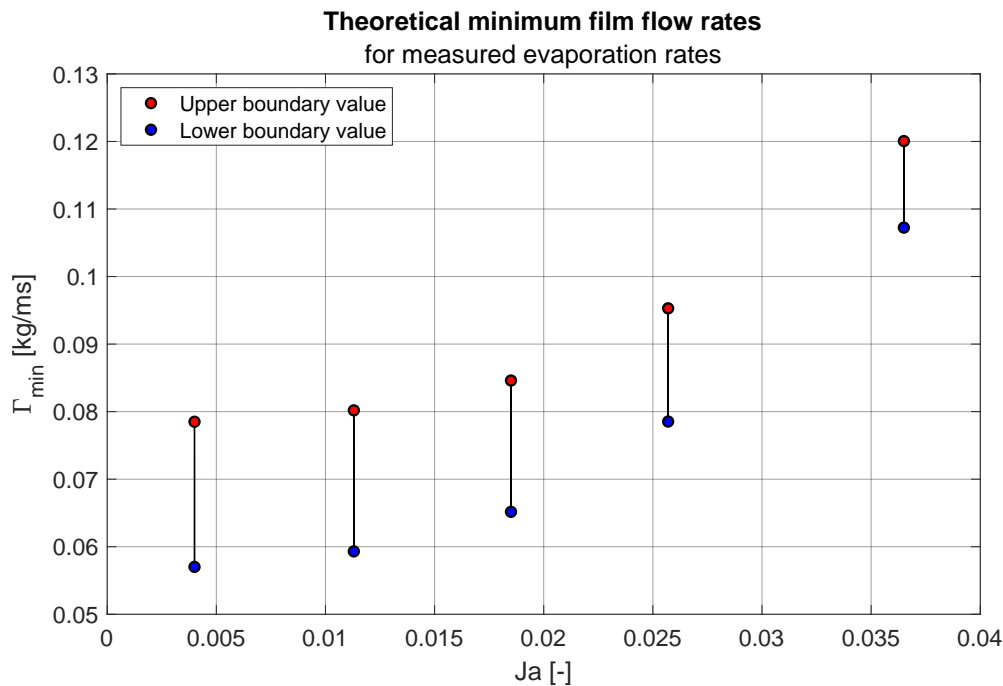


Figure 46: Theoretical minimum wetting rate[35], [40], for heat flow rates of the seemingly homogeneous films of figure 45.

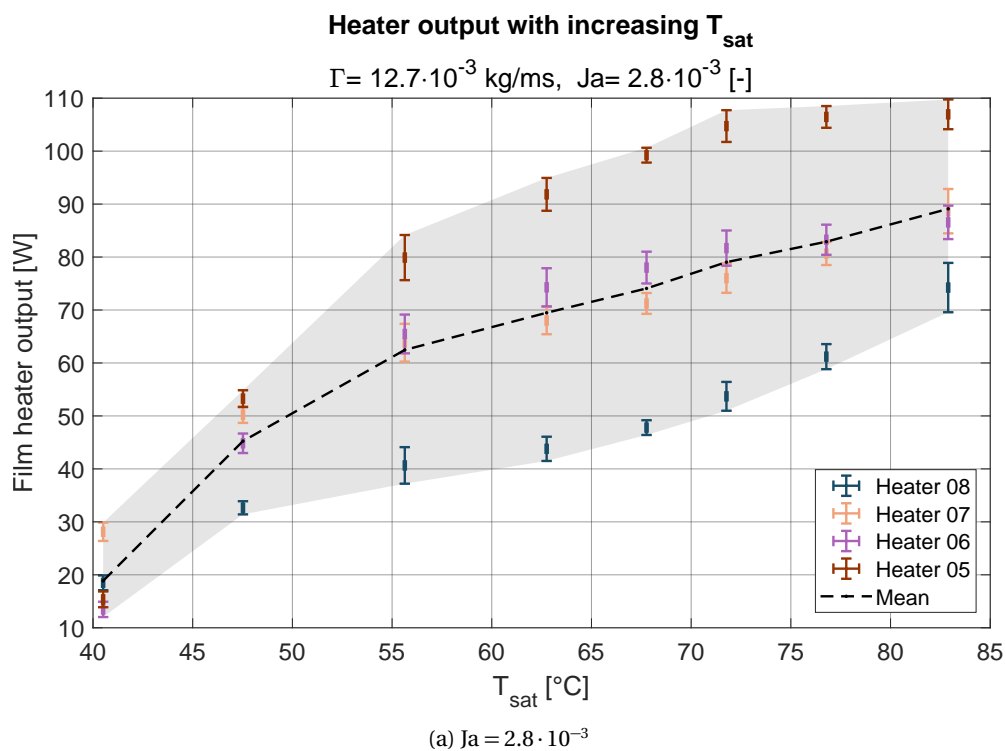
When assuming that the influence of vapour shear on the liquid film in the evaporator is negligible,[31] an approximation of the minimum wetting flow rate of a film subject to evaporation (on a flat vertical plate) can be found from the theory of El-Genk et al.[35], [40] Using the measured heat transfer rates of figure 45, an approximation of the minimum wetting rate for each sub-setting can be found for equilibrium contact angles of $65^\circ \leq \theta_0 \leq 80^\circ$. The predicted minimum wetting rates have been depicted in figure 46. As can be found from a comparison between figures 45 and 46, initially homogeneous annular films have been found for flow rates one order of magnitude smaller than the predicted minimum wetting rate by the theory for flat vertical plates by El-Genk et al.

All subfigures of figure 45 show the gradual onset of intermittency with decreasing initial flow rates. Prior to the onset of intermittency, the heat removal rate of a single film heater increases to a maximum at some film flow rate. The film velocity decreases with decreasing film flow rate. An increase in the bubble size (and a greater area for micro-layer evaporation) resulting from a decrease in the film shear,[23] or an increase in the sliding of vapour bubbles[24] resulting from a decrease in the film velocity may be the cause of an increase in the heat transfer rate. The above theory however requires visual verification in future work. With a further decrease of the film flow rate, the heater heat removal rate decreases, and intermittency ensues. As the film flow rate decreases, the heat removal rate of all-but-one heaters are found to consecutively decrease as described previously. Similarly to the results shown in figure 42, the onset of intermittency is first found to occur for heater 8, followed by an onset of intermittency for heaters 7 and 6, respectively. As a result of the consecutive decrease in individual heater heat removal rates, the total heat removal rate in the evaporator decreases with decreasing film flow rate for all subfigures. Below some film flow rate, long (in terms of duration) temperature spikes of significant magnitude impede further measurements, and decrease the heat removal rate substantially. From this flow rate onwards, the generation of additional data points is impeded as constant operating conditions can no longer be maintained in the heatpipe. The temperature spikes are indicative of permanent dry-out regions on the inner evaporator wall. Please note that the longer lasting spikes are less prevalent for small degrees of superheating (figure 45a).

As the Jakob number increases, the first onset of intermittent behaviour of any of the four film heaters is found at a greater initial liquid flow rate Γ . The flow rate required to sustain a film without (permanent) dry-out increases with increasing degrees of superheating. As a result of the evaporation of liquid in the evaporator, the film flow rate decreases with increasing distance from the top of the heated section. With this, the onset of both permanent- and intermittent film dry-out are expected to take place at an increasingly greater height from the bottom of the evaporator with increasing degrees of superheating. Analogously, an increasing amount of interior evaporator surface area is not used for heat transfer with increasing Jakob numbers.

4.3 Increasing saturation temperature

The following paragraphs will show and discuss the results originating from the measurements proposed in section 3.3.3. Figure 47 shows the film heater outputs for increasing saturation temperatures, for various Jakob numbers in films with flow rates beyond the onset of intermittent dry-out phenomena.



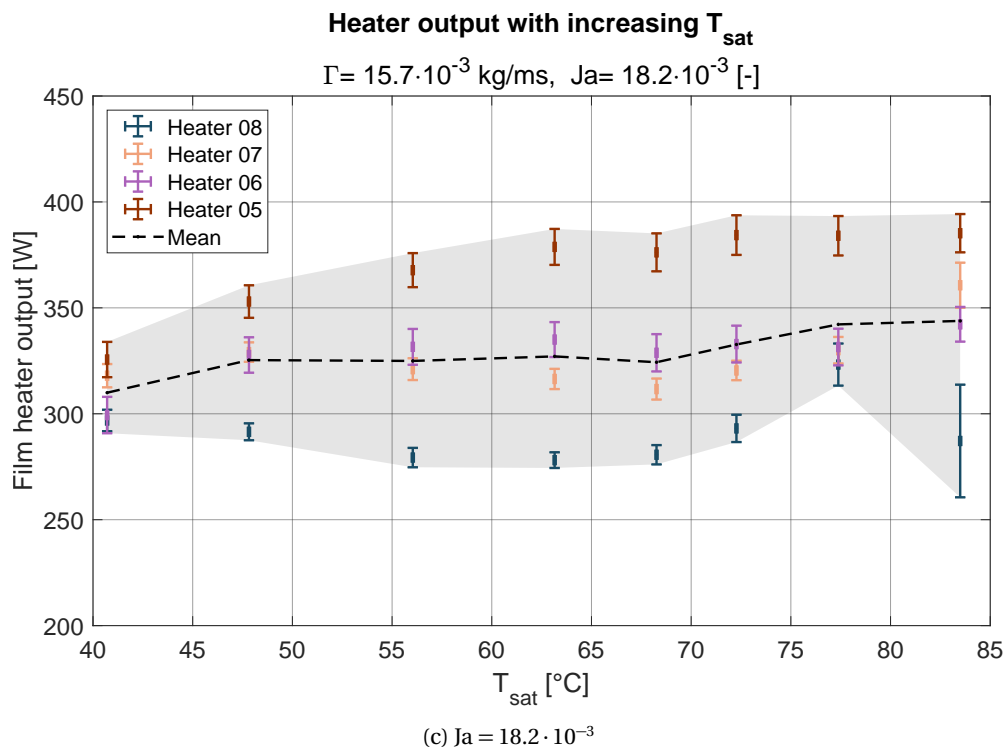
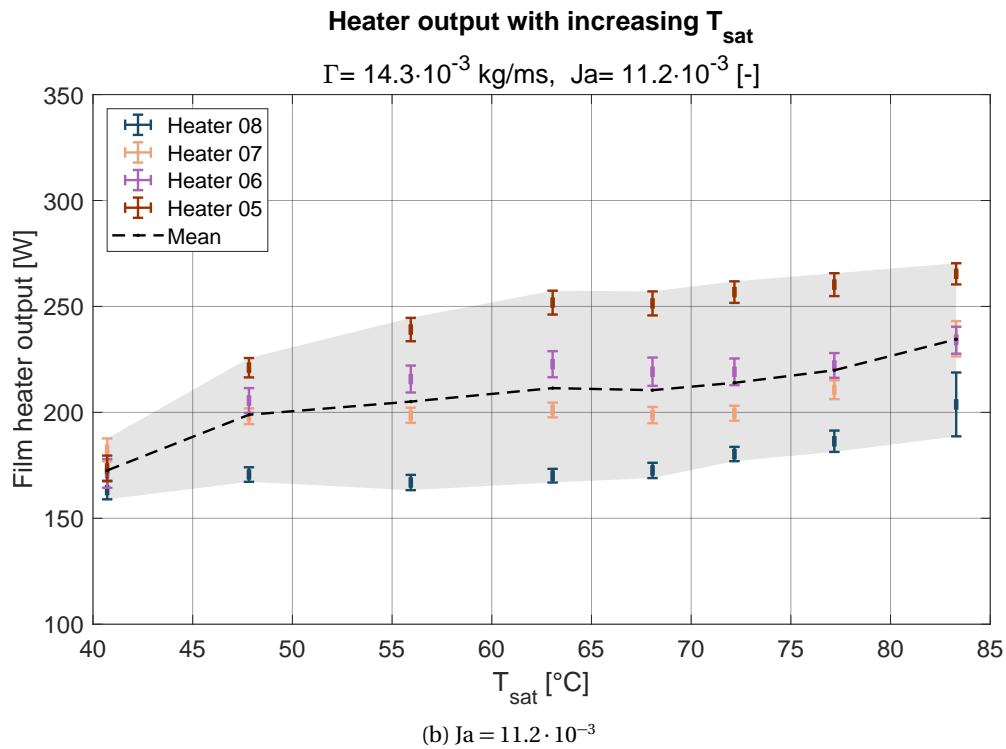


Figure 47: Film heater output at increasing saturation temperature T_{sat} , for various Jakob numbers. The gray area indicates the degree of spreading between the greatest ($\dot{Q}_{i,\text{in}} + u_{\dot{Q}}$) and the lowest ($\dot{Q}_{i,\text{in}} - u_{\dot{Q}}$) film heater output for some value of Ja . Data shown in figure includes 68% ($t_{v,p}=1$) confidence interval.

Figures 47b and 47c show an increase in all film heater heat removal rates for an increasing saturation temperature, for measurements with intermediate Jakob numbers. A steeper increase in the film heater throughputs is found for low degrees of superheating, as shown in figure 47a. As the saturation temperature of the systems decreases below $T_{\text{sat}} = 55^\circ\text{C}$, a substantial decrease in the heat removal rate is found with further decreasing saturation temperatures. Furthermore, all figure show no clear change in intermittency for consecutive data points, suggesting an indifference to the saturation temperature of the onset of dry-out.

The expected dependency of the heater heat transfer coefficient (directly proportional to the heat transfer rate) can be expressed using heat transfer coefficient figures of merit, as described in section 3.1.1. Figures of merit are material property groupings of certain approximations or formulae. An overview of the evolution of film evaporation and nucleate boiling figures of merit within the temperature range of figure 47 is given in figure 48.

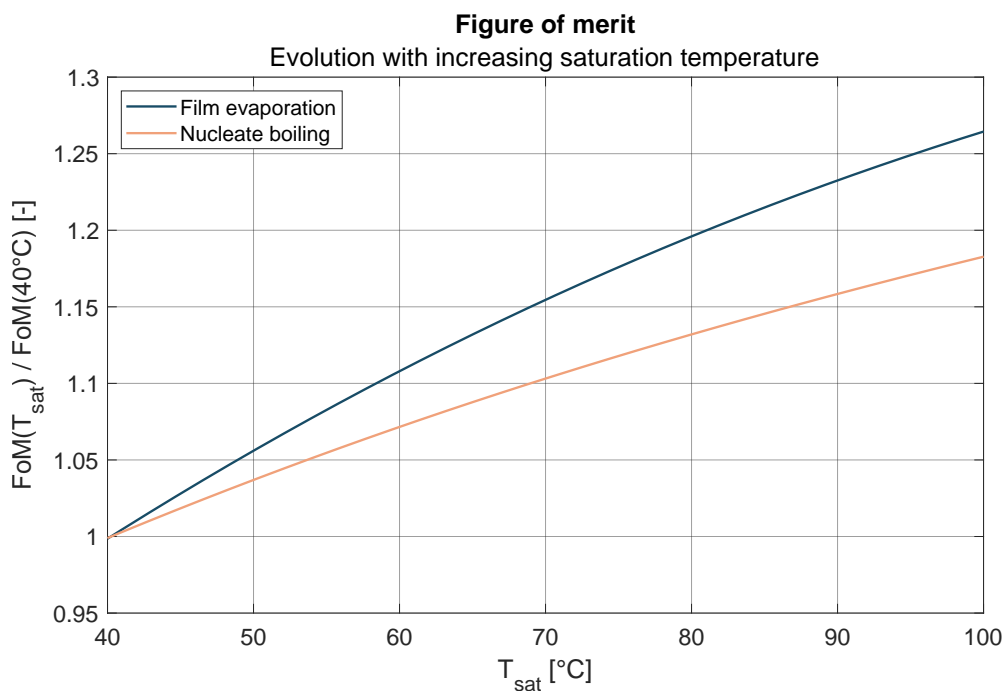


Figure 48: Evolution of heat transfer coefficient figures of merit, with increasing saturation temperature.

As can be seen from figure 48 a greater variation in the heat transfer rate with varying saturation temperature is expected for low degrees of superheating. The slope of the mean heat removal rate curve of figure 47a however greatly exceeds the film evaporation slope of figure 48. Over the range depicted in figure 47a, with increasing saturation temperatures, the heat removal rate rises to a value at a magnitude of 4.5 times the initial value at $T_{\text{sat}} = 40^\circ\text{C}$. The slope of the mean heat transfer rate curve however decreases beyond $T_{\text{sat}} = 55^\circ\text{C}$. With this, the operation of water-filled heatpipes at low degrees of superheating is highly unattractive at lower system pressures. Within a realistic temperature range for geothermal applications ($60^\circ\text{C} \leq T_{\text{sat}} \leq 80^\circ\text{C}$), an increase of the heat transfer rate of approximately 25% is found with increasing T_{sat} . Please note that with increasing degrees of superheating, the relative variation in the heat removal rate decreases. The measurements shown in figures 47b and 47c are in more accordance with the theoretical nucleate boiling curve of figure 48.

4.4 Saturation temperature development

In section 4.3, the influence of the heatpipe saturation temperature was discussed. A significant dependency on the saturation temperature was found (notably for low degrees of wall superheating) in section 4.3. The saturation temperature in the device varies for different sets of heatpipe boundary conditions. When used for the extraction of geothermal heat, the heatpipe is a mostly passive heat transfer device, for which the operator can only vary the condenser conditions. Both the condenser cooling rate and the evaporator heat extraction rate may influence the heatpipe vapour fraction (and with this the saturation conditions in the system). Figure 51 shows the saturation temperature development with varying heat throughputs, at various cooling water flow rates. Please note that during all measurements, the inflow temperature of the cooling water remained constant.

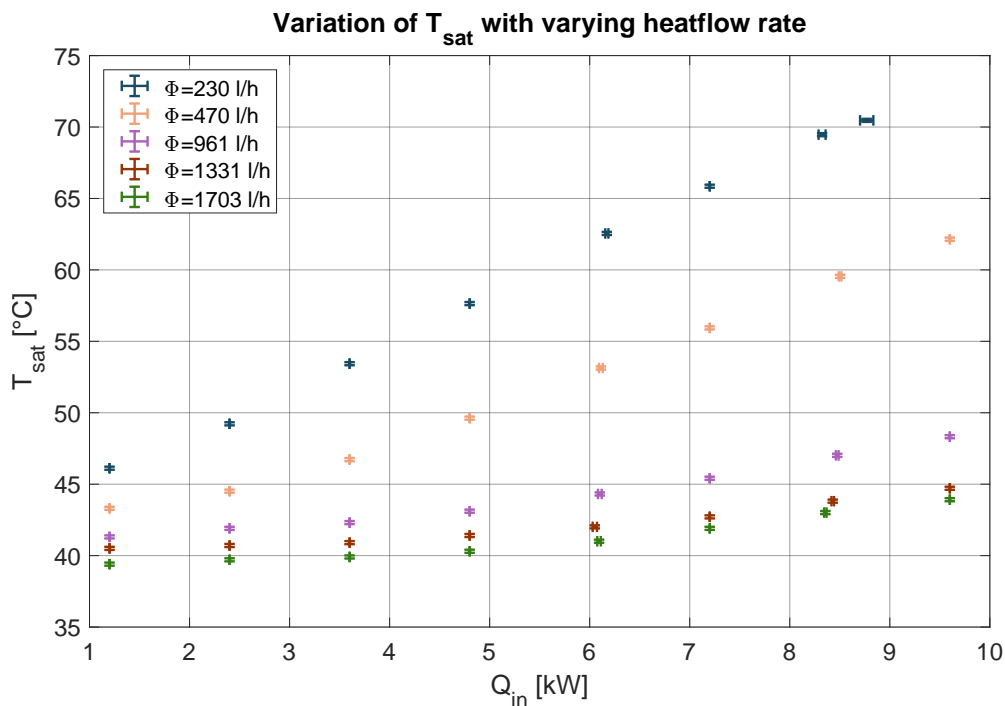


Figure 49: Heatpipe saturation temperature at varying heat flow rates, for various cooling flow rates. Data shown in figure includes 68% ($t_{v,p}=1$) confidence interval.

Figure 49 shows an increase in saturation temperature with increasing heat flow rates for any measured cooling flow rate. With increasing cooling flow rates, the saturation temperature rise decreases.

In order to condensate the vapour, the condenser wall temperature is to be kept at a temperature below the saturation temperature. As a result, the liquid film becomes subcooled. With increasing local heat transfer rates and decreasing condenser wall temperatures, the degree of subcooling increases. By increasing the coolant mass flow rate for an annulus of set width, both the coolant outflow temperature and the wall temperature will decrease.[8], [32] A fraction of the vapour annulus condensates when in contact with the subcooled film prior to reaching the condenser. As the degree of subcooling increases, the fraction of vapour condensating prior to reaching the condenser increases, decreasing the volume fraction of vapour in the heatpipe. With this, the pressure (and the saturation temperature) in the heatpipe decreases.

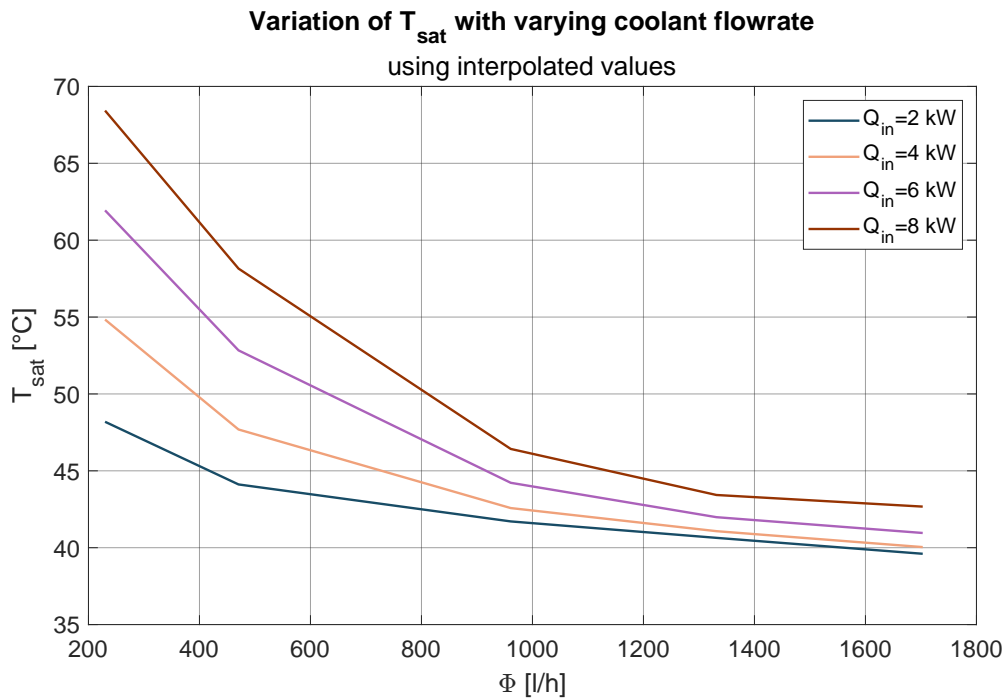


Figure 50: Heatpipe saturation temperature at varying cooling flow rates, for various heat flow rates. Data shown in figure stems from the linear interpolation of the values shown in figure 49.

During the operation of heatpipes on a geothermal scale, the coolant outflow temperature is to be maximized in order to produce heat at sufficiently high temperatures. As such, relatively low coolant flow rates are of interest. As can be seen from figure 50, the slopes of the curves are found to increase with decreasing coolant flow rates and increasing total heat flow rates. As such, the relative influence of adjustments to the coolant flow rate is significant at the relevant coolant flow rates range. In a full-scale system in which not only a single variable is varied, a decrease in the adjacent aquifer temperature would not only decrease the heat flow rate according to figure 42, but also decrease the heat transfer rate according to figure 47 as a result of the decrease in saturation temperature resulting from a decrease in the total heat flow rate (figure 49). Fortunately, as can be seen from figure 50, minor adjustments (decrease) to the coolant flow rate may further increase the total heat flow rate by increasing the saturation temperature of the system.

4.5 Heat extraction

The condenser heat extraction rate as a fraction of the evaporator heat flow rate is depicted in figure 51. Measurements have been performed with varying evaporator heat flow rates \dot{Q}_{in} , at various coolant mass flow rates.

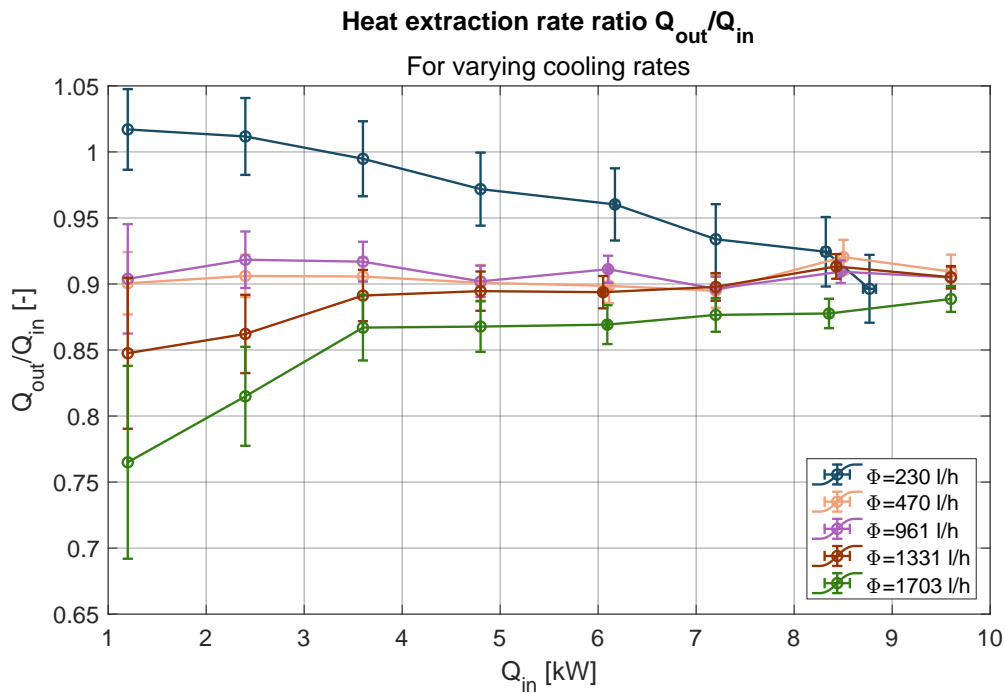


Figure 51: Heatpipe heat extraction rate with respect to the evaporator heat flow at varying evaporator heat flow rates, for various cooling flow rates. Data shown in figure includes 68% ($t_{v,p}=1$) confidence interval.

Figure 51 appears to show a decrease in the relative heat extraction rate for decreasing evaporator heat flow rates, and increasing coolant flow rates. However, owing to the large uncertainty intervals, no definite conclusions can be drawn from the data in figure 51. As the relative heat extraction rate contains uncertainty from TT_{out} , TT_{in} , the rotameter and the evaporator heat flow, its relative uncertainty interval is significantly larger than for any other discussed parameter in this study. An equivalent uncertainty interval has been found as per Appendix II: Experimental data & Error propagation. Please note that even with the large uncertainty intervals, a decrease in the relative heat extraction rate is found with increasing coolant flow rate for low values of the evaporator heat flow rate. The previous however directly contradicts the initial expectations of the author. Any heat that is not extracted in the condenser is lost to the environment through the heatpipe's insulation. With the exception of the evaporator, the interior surface temperature of the heatpipe is less than- or equal to the saturation temperature of the system. Figure 52 shows the theoretical interior wall temperature distribution of the evaporator, for a system operating at the greatest measured saturation temperature of figure 51, and at the greatest heat throughput. Here, only locally at heaters, the wall temperature exceeds the saturation temperature of the system.

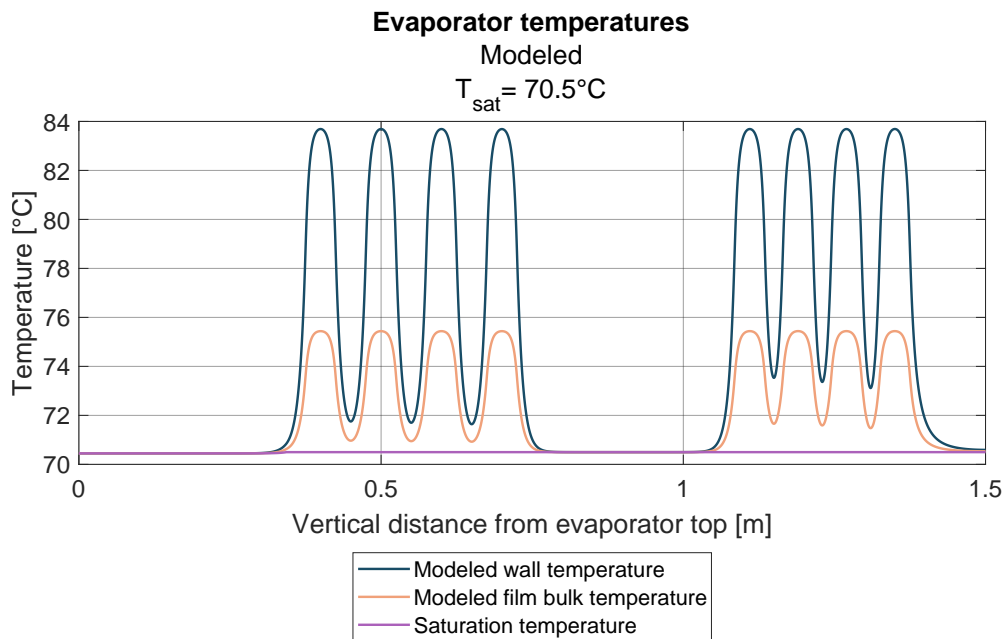


Figure 52: Modeled evaporator interior wall temperature, at maximum heat throughput.

The estimation of losses through the insulation shown in figure 35 suggests an increase in the total heat loss with an increasing saturation temperature. As shown in figure 50, the saturation temperature increases with decreasing coolant flow rates. The relative increase in heat flow rate is expected to be of greater magnitude than the relative increase of insulation losses resulting from an increase in the saturation temperature accompanied with the increase in heat flow rate. As such, a greater efficiency should be found for greater heat flow rates, and appropriate results for figure 51 should have an upward concave slope, similar to the lines with large coolant flow rates in figure 51. Furthermore, as per the approximation of figure 35, all results (with the exception of the $250 \frac{1}{h}$ measurements) are expected to be in closer proximity of unity. As per the previous, meticulous re-calibration of the rotameter should be considered in order to find the systematic error that offsets the measurements for the lines in figure 51 with flow rates greater than and equal to $470 \frac{1}{h}$. The measurement results for a coolant flow rate of $230 \frac{1}{h}$ significantly deviate from all other measurement sets, possibly as a result an oversight of the presence of any transient effects. As such, the measurement set with a flow rate of $230 \frac{1}{h}$ should be redone in future work, in order to provide a more accurate version of figure 51.

4.6 Homogenizer effectiveness

The transparent segments in the adiabatic section of the experimental setup allow for additional visual insight in the behaviour of the liquid film. As such, a visual comparison of the film behaviour in the presence or absence of homogenizer is possible. The greatest visual difference is found at a film flow rate of $\Gamma = 7.7 \cdot 10^{-3} \frac{\text{kg}}{\text{ms}}$. A visual comparison of the film at this flowrate is presented in the following paragraphs. Figure 53 shows the evolution of the film over a set time interval, as has been captured by a 240 Hz camera, at a fixed location in the transparent section of the heatpipe. In order to visualize the presence of a moving film, a sheet with equidistant lines and indicated centerpoints has been placed behind the transparent tube section. Passing interfacial waves will distort the lines of the adjacent sheet to a varying degree. The location of a single wavefront with increasing time is indicated using a red dotted line in figure 53.

In both cases, the liquid film contains interfacial waves. Directly after the homogenizer, little waves are present in the film. With increasing distance from the homogenizer, a larger number of waves becomes visually apparent. Larger, faster waves are found to reach and merge with smaller, slower waves.[9] At sufficient distance from the homogenizer, lateral interaction between separate wave fronts is found.[59]

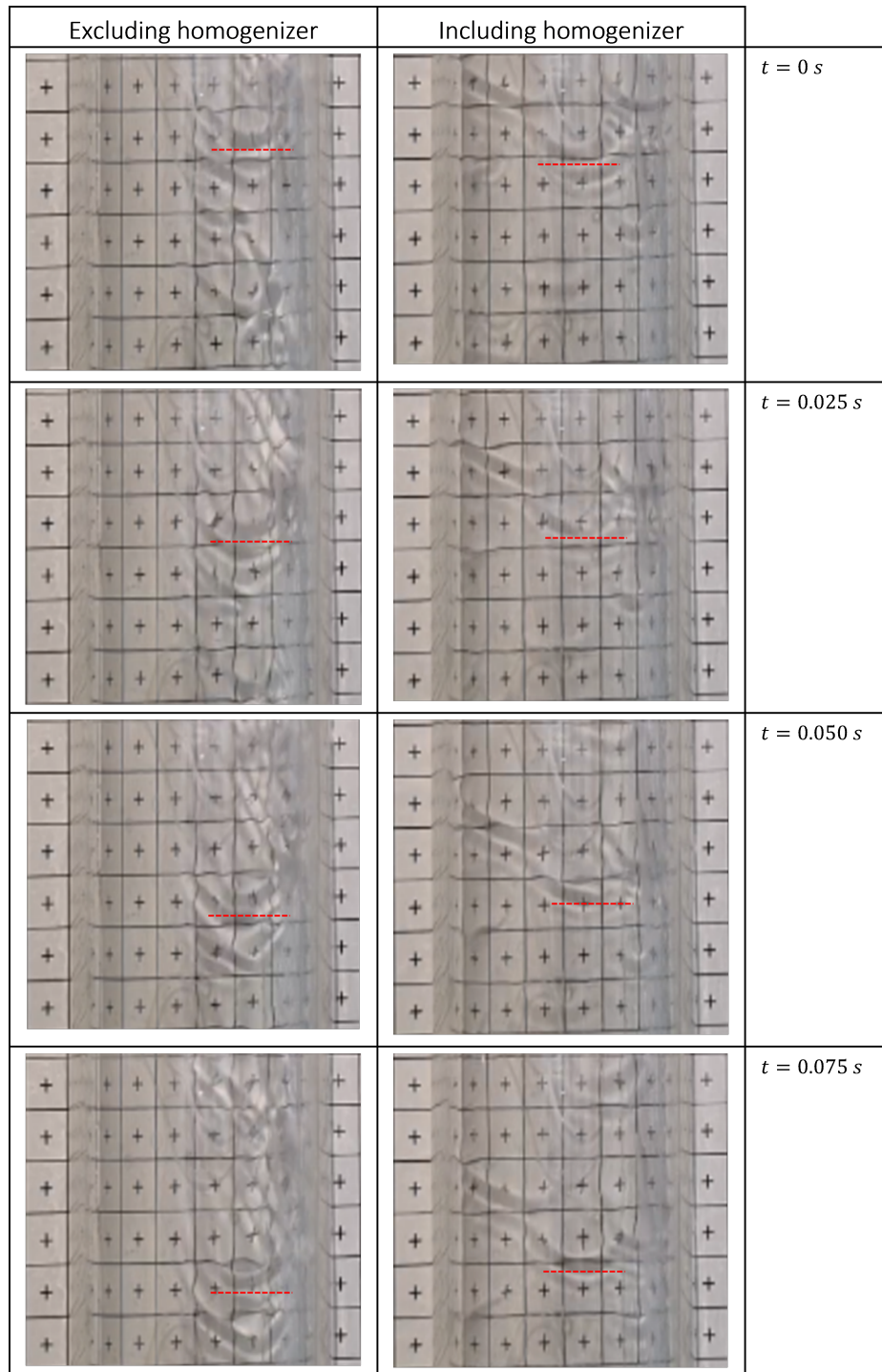


Figure 53: Visual comparison of system equipped with- (right) and without (left) homogenizer, for $\Gamma = 7.7 \cdot 10^{-3} \frac{\text{kg}}{\text{ms}}$. The position of a single interfacial wave has been indicated with the red dotted line. The interval between consecutive equidistant lines is 10.1 mm.

The images of the setup containing a homogenizer prior to the transparent section (right half of figure 53) differ from images taken of a setup in which a homogenizer is absent (left half of figure 53). In the absence of a homogenizer, the liquid appears to be distributed in a single rivulet on the right side of the

images depicted in figure 53, as little distortion is shown on the left side of the tube. All images on the right side of the figure however show distortion along the entire annulus, indicative of an entirely annular film. The homogenized film also appears to be more quiescent than the film that has not been previously distributed. A comparison of the recorded waviness furthermore suggests a larger degree of liquid spreading for a setup that includes a homogenizer. As indicated by the red line in figure 53, wave fronts (of which more are present in the left half of figure 53) travel at a larger velocity for non-homogenized liquid films, indicative of thicker film sections.[9] The previous has been found for multiple comparisons of visual wave propagation between the two setups. The rate at which waves are present in the films is also significantly greater for the non-homogenized film.

A quantitative comparison of the effectiveness of the homogenizer insert is shown in figure 54. Here, the measurements proposed in section 3.3.1 and shown in figure 42, are repeated in the absence of a homogenizer ring. Figure 54 shows the film heater heat removal rate at increasing Jakob numbers, without the presence of a homogenizer. A side-by-side comparison of figures 42 and 54 can be found in Appendix VI: Auxiliary figures.

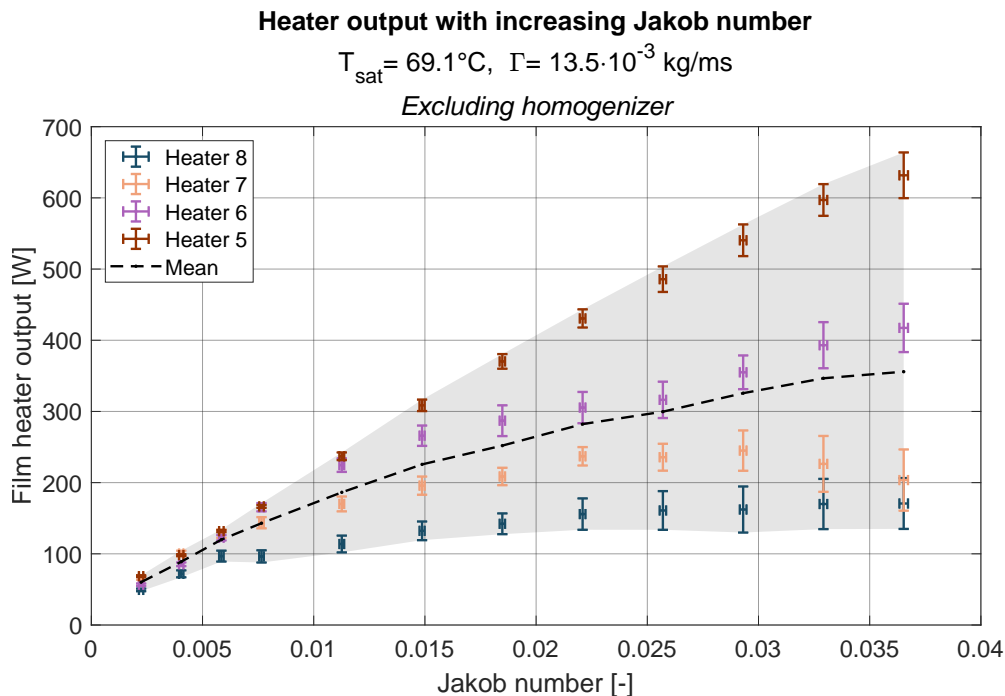


Figure 54: Heater heat removal rate for film heaters, as a function of the degree of superheating, expressed with the Jakob number (Ja [-]), excluding homogenizer. Here, $T_{\text{sat}} = 69.1^\circ\text{C}$ and $\Gamma = 13.3 \cdot 10^{-3} \frac{\text{kg}}{\text{ms}}$. The gray area indicates the degree of spreading between the greatest ($\dot{Q}_{i,\text{in}} + u_{\dot{Q}}$) and the lowest ($\dot{Q}_{i,\text{in}} - u_{\dot{Q}}$) film heater output for some value of Ja . Data shown in figure includes 68% ($t_{v,p}=1$) confidence interval

Similarly to the results of figure 42, figure 54 shows an increasing degree of spreading of the heat removal rates of the film heaters with increasing values of the Jakob number. For both cases, the heat removal rate of heater 5 (the bottom heater) is similar. The increase of the heat transfer rate of heater 8 stagnates at an earlier point for the setup in which a homogenizer has been omitted. A similar trend is found for heaters 7 and 6. The results of section 4.2 suggest that the flow rate at which dry-out is first found increases with the degree of superheating. The earlier (lower Jakob number) onset of intermittent behaviour in the measurements shown in figure 54 therefore implicates that the film thickness at heaters 8, 7, and 6 has decreased with respect to the homogenized setting. As such, a greater variation in the film thickness is found for a film that has not been re-distributed. Similarly to the results in figure 42, the heat removal rate does no longer significantly increase with increasing degree of superheating beyond the initial onset

of intermittency. As the onset of intermittency however occurs at lesser degrees of superheating for the results shown in figure 54 than for the results shown in 42, the resulting mean heat removal rate of the heatpipe evaporator is of lesser magnitude, as can be seen from figure 54.

With this, the homogenizer discussed and proposed in section 3.1.5, appears to improve the spreading of water films on copper surfaces in a water-vapour containing environment. As such, for heatpipes in which (to some degree) an inhomogeneous film is expected to be formed or in which the film is disturbed as a result of nucleate boiling, the film can be redistributed using the proposed homogenizer in order to increase the heat transfer area of the evaporator or delay the local onset of dry-out.

5 Conclusions

As passive geothermal heat extraction may not be possible in tall liquid pools in heatpipes, aquifer heat is to be removed with falling liquid films. An experimental heatpipe setup is used to study annular liquid film heat transfer in this work. The experimental setup has been made to operate within an operational envelope, bounded by the operational limits listed in section 3.1.2.1. A tendency of liquid films to break up into separate rivulets at certain flow rates, or to form dry-patches when heated may significantly limit the available area for- and rate of heat transfer. The influence of variations in operating conditions, liquid flow rates and the heating intensity on the film heat removal rate and the onset of heat transfer area limiting phenomena are studied.

In order to ensure that a homogeneous annular film is provided to the measurement sector, melamine foam homogenizer rings are placed above the heatpipe evaporator. To some degree, the homogenizer rings are found to re-distribute inhomogeneous films and reduce the variation in the film thickness. Homogenized annular films are found to exist at flow rates one order of magnitude smaller than the break-up flow rates of similar flat films. Furthermore, re-distributed films are found to transfer heat (mean heat transfer rate) at rates up to 28% greater than unhomogenized films, as a result of a delayed local onset of film dry-out. In order to remove any significant inhomogeneities resulting from irregularities in the experimental apparatus, a homogenizer is used for all film measurements in this work.

As a result of the extraction of heat, the aquifer temperature adjacent to the heatpipe may vary significantly. As such, the degree of wall superheating may also vary. At fixed operating conditions, an increase in the Jakob number (a measure of the degree of wall superheating) increases the mean heat removal rate of the evaporator. With increasingly large degrees of superheating, however, thin film sections are found to experience intermittent dry-out. A further increase of the heat transfer rate is locally suppressed, possibly as a result of the onset of film dry-out. As a result, the slope of the mean heat removal rate curve decreases with further increasing Jakob numbers.

As a large fraction of the liquid film evaporates prior to reaching the bottom of the heatpipe, a thin, low velocity film remains. Such thin films may experience film dry-out when heated. With greater degrees of superheating, the liquid flow rate at which a first onset of dry-out is found increases as a result of the increased bubble interference by vapour nuclei at greater Jakob numbers. As such, a greater area of heat transfer is lost at the bottom of the heatpipe film evaporator with greater degrees of superheating. Locally, at flow rates marginally greater than the flow rate at which intermittent dry-out is first found, a maximum in the film heat transfer rate is found.

With varying aquifer temperatures, the evaporator heat flow rate will also vary. The heatpipe saturation temperature increases as the total heat flow rate increases at a set coolant flow rate. With decreasing cooling water flow rates, the rate at which the saturation temperature increases, increases. With decreasing saturation temperatures, the heat removal rate of the liquid film decreases. A steeper decline in the heat removal rate is found for increasingly lower degrees of wall superheating. For the lowest considered degree of superheating in this work, the evaporator heat removal rate decreases substantially below a saturation temperature of $T_{\text{sat}} = 55^\circ\text{C}$.

6 Recommendations

In order to be able to approximate and model the heatpipe yield over time, changes to the experimental evaporator are desired. Ideally, one would install heating devices of which the heat flux is (more) homogeneous, and known. As such, a correction to the results depicted in figure 42 can be made. With this, more presentable data on the film heat removal rate at the correct degrees of superheating can be presented.

The increase in the intermittency of the heater heat removal rates found at either decreasing liquid film flow rates or at increasing degrees of superheating has been tied to film dry-out in this work. An additional visual analysis, found from modifications to the experimental setup, may confirm the presence of the phenomenon and confirm the onset of heat transfer rate intermittency when film dry-out is first observed.

Preliminary measurements in this work showed an increase in the heat transfer rate for heaters placed in sections with greater surface roughness. The currently used approximation for the heat transfer coefficient does however not consider the influence of surface roughness. Additional attention can therefore be brought upon the effect of surface finishing and evaporator wall materials on film heat removal and film dry-out.

As heat is to be offered at temperatures close to the saturation temperature, an additional set of measurements at varying coolant temperatures is of interest. Here, the influence of the coolant inflow temperature on the coolant outflow temperature and the saturation temperature in the heatpipe should be discussed.

Additional attention to the possibility of aquifer forcing may also be of interest, as the system may significantly benefit from increased aquifer temperature replenishment rates. Here, the heat replenishment rate should be approximated for various realistic forced and unforced scenarios. Please note however that forcing is only possible for porous layers with sufficient permeability.

With the additional knowledge found from the analyses proposed above, a transient or quasi-static model of the aquifer heat extraction system could be generated. A coupled model of both the aquifer temperature (and its heat replenishment rate) and the heatpipe heat extraction rate (including dry-out losses) may give insight in the long-term attractiveness of heatpipes in geothermal settings.

A significant amount of additional topics not directly related to the current vertical water-filled set-up can also be explored in future work. The use of alternative media, such as ammonia, can be investigated. For this, a more internal pressure resilient structure should be erected, preferably consisting of flanged pipe sections. As bore holes may not always be vertical, the heat extraction of non vertically falling films should be further investigated. A possible departure from annular film flow to a stratified liquid flow may significantly decrease the available liquid heat transfer area in the geothermal aquifer. At last, further attention can be brought upon the maximization of the heat transfer area in the aquifer with the use of possibly horizontal liquid-filled side branches in the heatpipe evaporator. An analysis of the economic feasibility of such side branches should also be considered.

A Appendix I: Purchased part-list

Appendix A will serve to provide the reader with links to manufacturer's listings of items and parts bought for the experimental apparatus.

	Part name:	Referred to in:	Info link:
A1	Rockwool pipe insulation	Section 3.1.4.2	Click here
A2	EPDM coupling	Section 3.1.4.3	Click here
A3	Radiator hose	Section 3.1.4.3	Click here
A4	Band heater	Section 3.1.3	Click here
A5	RKC RB100 controller	Section 3.1.3.3	Click here
A6	RKC MA901 controller	Section 3.1.3.3	Click here
A7	Thermal paste	Section 3.1.3	Click here
A8	Thermocouple	Section 3.1.3.4	Click here
A9	Adhesive PT100	Section C.2	Click here
A10	PT100 probe transmitter	Section C.2	Click here
A11	Transparent tube	Section 3.1.4.5	Click here
A12	Steel tube insert	Section 3.1.4.5	Click here
A13	Melamine foam/ Magic eraser	Section 3.1.5	Click here

Table 5: Overview of purchased parts for experimental setup.

B Appendix II: Experimental data & Error propagation

The following sections will aim to list any data shown in section 4. An estimation of the uncertainty in the final data points shown in the figures is given, at the confidence intervals specified with their respective confidence levels. An overview of the uncertainty analysis leading to the uncertainty intervals listed in the data is given in section B.1.

B.1 Error propagation

The reasoning of the following paragraphs follows the work of Figliola et al.[69] According to the work of Figliola et al., an estimate of the true value of some variable R' when (optimistically) assuming any systematic error has been made negligible as a result of the calibration of all sensors, is given with equation (56). The combined standard uncertainty u_R is given as a function of the t value, and the random standard uncertainty in the result s_R .

$$R' = \bar{R} \pm u_R = \bar{R} \pm t_{\nu,P} s_R \quad (P\%) \quad (56)$$

$$s_R = \left(\sum_{i=1}^L \left[\frac{\partial R}{\partial x_i} \Big|_{x=\bar{x}} s_{\bar{x}_i} \right]^2 \right)^{\frac{1}{2}}$$

Here, the random standard uncertainty of the variable $s_{\bar{x}}$ is the equivalent random standard uncertainty of variable x , found from the root sum square of any individual random standard uncertainties applicable to the relevant variable. As such, measurement uncertainties can be combined with uncertainties stemming from calibration for a single variable. The random standard uncertainty ($s_{\bar{x}}$) can be found with equation (57), if repeated measurements are made under fixed operating conditions.

$$s_{\bar{x}} = s_x / \sqrt{N} \quad (57)$$

Here, s_x is the standard deviation of the set of measurements (68%), with N being the number of independent samples.

If only a single measurement of a variable is taken as a result of the absence of data logging for the variable (e.g. flowmeter measurement), an estimation of a random error in the measurement ($s_{\bar{x}}$) is given with the truncation error, equal to the digital instrument resolution (95%).

As the heater heat flow measurements ($\dot{Q}_{i,\text{out}}$) are not repeated measurements of a single constant variable at constant operating conditions, the uncertainty interval is given as a function of the standard deviation of the set of measurements, as per equation (58).

$$\dot{Q}'_{i,\text{out}} = \bar{\dot{Q}}_{i,\text{out}} \pm t_{\nu,P} s_x \quad (58)$$

B.2 Data: Increasing ΔT

Measurement description	Increasing ΔT , including homogenizer
Discussed in	Sections 3.3.1 and 4.1
Shown in	Figure 42
Relevant sensors	$TT_{\text{sat}}, TT_{08}, TT_{07}, TT_{06}, TT_{05}$
Constant variables	$T_{\text{sat}} = 69.1^\circ\text{C}, \Gamma = 13.3 \cdot 10^{-3} \frac{\text{kg}}{\text{ms}}$
Confidence interval	95%

$T_{\text{wall}} [^\circ\text{C}]$	$T_{\text{sat}} [^\circ\text{C}]$	$\Gamma \cdot 10^3 [\frac{\text{kg}}{\text{ms}}]$	$\text{Ja} \cdot 10^3 [-]$	$\dot{Q}_{8,\text{in}} [\text{W}]$	$\dot{Q}_{7,\text{in}} [\text{W}]$	$\dot{Q}_{6,\text{in}} [\text{W}]$	$\dot{Q}_{5,\text{in}} [\text{W}]$
70.3±0.0	69.1±0.1	13.3±0.0	2.2±0.2	33.4±2.7	45.5±2.4	40.2±2.5	51.1±1.9
71.3±0.0	69.1±0.1	13.3±0.0	4.0±0.2	64.6±2.9	77.6±3.8	72.9±4.0	85.4±2.0
72.3±0.0	69.1±0.1	13.3±0.0	5.8±0.2	97.7±6.7	108.3±4.2	105.0±5.6	118.6±2.6
73.3±0.0	69.1±0.1	13.3±0.0	7.7±0.2	124.1±6.3	139.5±5.5	136.4±7.4	150.9±3.3
75.3±0.0	69.1±0.1	13.3±0.0	11.3±0.2	179.8±16.3	205.0±14.9	200.2±11.3	215.7±6.9
77.4±0.0	69.1±0.1	13.3±0.2	14.9±0.2	207.9±36.5	270.4±25.9	263.5±16.0	273.2±9.5
79.4±0.1	69.1±0.1	13.3±0.2	18.5±0.2	245.3±50.9	294.3±50.3	337.1±20.7	338.3±12.9
81.4±0.1	69.1±0.1	13.3±0.2	22.1±0.2	246.3±49.2	310.4±51.6	414.4±22.7	387.5±17.3
83.4±0.1	69.1±0.1	13.3±0.4	25.7±0.3	277.6±79.1	333.7±73.4	463.6±38.8	438.8±20.2
85.4±0.1	69.1±0.1	13.2±0.4	29.3±0.3	274.8±70.0	332.8±96.7	500.0±53.8	505.8±26.7
87.4±0.1	69.1±0.1	13.4±0.4	32.9±0.3	281.3±87.8	372.9±105.0	532.9±76.6	575.0±29.2
89.4±0.2	69.1±0.1	13.2±0.6	36.5±0.3	285.0±64.0	370.2±114.4	537.9±97.2	660.5±32.4

Table 6: Dataset: Film heater heat removal rate $\dot{Q}_{i,\text{in}}$, as a function of the degree of superheating, expressed with the Jakob number ($\text{Ja} [-]$). Experimental set-up includes homogenizer. Data from 301 measurements points.

B.3 Data: increasing initial flow rate

Measurement description	Increasing Γ , including homogenizer
Discussed in	Sections 3.3.2 and 4.2
Shown in	Figure 45a
Relevant sensors	$TT_{\text{sat}}, TT_{08}, TT_{07}, TT_{06}, TT_{05}$
Constant variables	$T_{\text{sat}} = 69.1^\circ\text{C}, T_{\text{wall}} = 71.3^\circ\text{C}, \text{Ja} = 4.0 \cdot 10^{-3} [-]$
Confidence interval	95%

$T_{\text{wall}} [^\circ\text{C}]$	$T_{\text{sat}} [^\circ\text{C}]$	$\text{Ja} \cdot 10^3 [-]$	$\Gamma \cdot 10^3 [\frac{\text{kg}}{\text{ms}}]$	$\dot{Q}_{8,\text{in}} [\text{W}]$	$\dot{Q}_{7,\text{in}} [\text{W}]$	$\dot{Q}_{6,\text{in}} [\text{W}]$	$\dot{Q}_{5,\text{in}} [\text{W}]$
71.3±0.0	69.1±0.1	4.0±0.2	6.5±0.1	44.6±9.7	32.9±13.7	63.1±19.6	121.4±13.3
71.3±0.0	69.1±0.1	4.0±0.2	7.2±0.1	49.2±9.6	47.7±16.8	74.2±17.0	119.3±5.6
71.3±0.0	69.1±0.1	4.0±0.2	7.9±0.1	47.6±9.2	62.9±19.8	103.2±19.1	110.4±4.3
71.3±0.0	69.1±0.1	4.0±0.2	8.6±0.1	51.4±10.9	79.8±15.9	114.4±16.2	104.9±3.3
71.3±0.0	69.1±0.1	4.0±0.2	9.3±0.1	55.8±9.3	93.7±18.6	117.7±9.8	104.7±4.4
71.3±0.0	69.1±0.1	4.0±0.2	10.0±0.1	61.0±11.2	108.5±17.1	112.6±9.1	105.1±3.0
71.3±0.0	69.1±0.1	4.0±0.2	10.7±0.0	70.1±8.7	118.1±9.3	101.4±7.5	104.7±1.9
71.3±0.0	69.1±0.1	4.0±0.2	11.3±0.0	76.1±10.1	112.6±7.9	96.5±5.7	103.5±2.6
71.3±0.0	69.1±0.1	4.0±0.2	11.9±0.0	78.6±10.2	102.6±6.8	91.6±6.3	103.7±3.4
71.3±0.0	69.1±0.1	4.0±0.2	12.5±0.0	76.3±7.2	96.9±5.0	90.9±4.4	105.7±2.7
71.3±0.0	69.1±0.1	4.0±0.2	13.2±0.0	75.3±4.7	94.9±5.3	91.0±7.0	107.9±3.5
71.3±0.0	69.1±0.1	4.0±0.2	13.8±0.0	70.7±3.8	92.0±3.9	90.7±4.8	108.8±2.4

 Table 7: Dataset: Film heater heat removal rate $\dot{Q}_{i,\text{in}}$ at decreasing initial liquid film flow rate. Experimental set-up includes homogenizer. Data from 241 measurements points.

Measurement description	Increasing Γ , including homogenizer
Discussed in	Sections 3.3.2 and 4.2
Shown in	Figure 45b
Relevant sensors	$TT_{\text{sat}}, TT_{08}, TT_{07}, TT_{06}, TT_{05}$
Constant variables	$T_{\text{sat}} = 69.1^\circ\text{C}, T_{\text{wall}} = 75.3^\circ\text{C}, \text{Ja} = 11.3 \cdot 10^{-3} [-]$
Confidence interval	95%

$T_{\text{wall}} [^\circ\text{C}]$	$T_{\text{sat}} [^\circ\text{C}]$	$\text{Ja} \cdot 10^3 [-]$	$\Gamma \cdot 10^3 [\frac{\text{kg}}{\text{ms}}]$	$\dot{Q}_{8,\text{in}} [\text{W}]$	$\dot{Q}_{7,\text{in}} [\text{W}]$	$\dot{Q}_{6,\text{in}} [\text{W}]$	$\dot{Q}_{5,\text{in}} [\text{W}]$
75.3±0.1	69.1±0.1	11.3±0.2	7.9±0.2	81.4±14.3	91.5±30.0	135.2±35.7	245.5±23.5
75.3±0.1	69.1±0.1	11.3±0.2	8.9±0.2	99.7±19.4	141.3±28.4	200.4±40.6	251.3±15.9
75.3±0.1	69.1±0.1	11.3±0.2	9.7±0.2	113.1±24.6	167.7±27.7	229.3±32.9	245.2±14.6
75.3±0.0	69.1±0.1	11.3±0.2	10.5±0.1	128.1±23.7	186.1±31.0	245.8±24.4	235.9±9.5
75.3±0.0	69.1±0.1	11.3±0.2	11.2±0.1	134.1±26.0	200.5±26.5	248.0±17.4	233.8±8.0
75.3±0.0	69.1±0.1	11.3±0.2	11.9±0.1	165.7±25.8	223.8±22.5	235.4±15.9	234.8±7.6
75.3±0.0	69.1±0.1	11.3±0.2	12.6±0.1	179.0±21.4	231.4±18.1	227.6±13.5	237.9±8.2
75.3±0.0	69.1±0.1	11.3±0.2	13.3±0.1	192.0±10.8	234.7±13.8	220.1±11.7	242.7±8.0
75.3±0.0	69.1±0.1	11.3±0.2	14.0±0.1	197.9±9.8	234.1±13.3	226.4±11.9	252.9±9.0
75.3±0.0	69.1±0.1	11.3±0.2	14.6±0.1	192.2±8.6	221.4±8.9	225.6±11.4	257.7±8.6
75.3±0.0	69.1±0.1	11.3±0.2	15.2±0.1	189.5±5.8	218.9±10.8	228.3±11.3	262.8±9.5

 Table 8: Dataset: Film heater heat removal rate $\dot{Q}_{i,\text{in}}$ at decreasing initial liquid film flow rate. Experimental set-up includes homogenizer. Data from 241 measurements points.

Measurement description	Increasing Γ , including homogenizer
Discussed in	Sections 3.3.2 and 4.2
Shown in	Figure 45c
Relevant sensors	$TT_{\text{sat}}, TT_{08}, TT_{07}, TT_{06}, TT_{05}$
Constant variables	$T_{\text{sat}} = 69.1^\circ\text{C}, T_{\text{wall}} = 79.4^\circ\text{C}, \text{Ja} = 18.5 \cdot 10^{-3} [-]$
Confidence interval	95%

$T_{\text{wall}} [^\circ\text{C}]$	$T_{\text{sat}} [^\circ\text{C}]$	$\text{Ja} \cdot 10^3 [-]$	$\Gamma \cdot 10^3 [\frac{\text{kg}}{\text{ms}}]$	$\dot{Q}_{8,\text{in}} [\text{W}]$	$\dot{Q}_{7,\text{in}} [\text{W}]$	$\dot{Q}_{6,\text{in}} [\text{W}]$	$\dot{Q}_{5,\text{in}} [\text{W}]$
79.4±0.1	69.1±0.1	18.5±0.2	10.4±0.3	156.2±23.3	217.2±41.6	280.1±56.6	368.7±27.9
79.4±0.1	69.1±0.1	18.5±0.2	11.4±0.2	232.5±25.5	241.8±39.6	331.1±43.6	354.2±18.4
79.4±0.1	69.1±0.1	18.5±0.2	12.2±0.2	231.9±26.4	273.2±34.8	357.3±32.3	348.7±16.9
79.4±0.0	69.1±0.1	18.5±0.2	13.0±0.1	259.5±20.0	306.9±31.4	353.3±22.2	345.8±13.8
79.4±0.0	69.1±0.1	18.5±0.2	13.7±0.1	272.2±16.5	330.3±26.9	335.1±17.9	347.1±14.5
79.4±0.0	69.1±0.1	18.5±0.2	14.4±0.1	284.4±12.3	341.4±21.3	325.6±17.0	352.7±14.3
79.4±0.0	69.1±0.1	18.5±0.2	15.0±0.1	286.7±8.5	336.3±12.8	320.2±15.9	359.0±15.7
79.4±0.0	69.1±0.1	18.5±0.2	15.7±0.1	290.3±10.8	326.6±13.5	319.2±16.0	367.7±15.0
79.4±0.0	69.1±0.1	18.5±0.2	16.3±0.1	285.7±6.9	319.9±8.7	320.6±15.2	371.4±16.9

Table 9: Dataset: Film heater heat removal rate $\dot{Q}_{i,\text{in}}$ at decreasing initial liquid film flow rate. Experimental set-up includes homogenizer. Data from 241 measurements points.

Measurement description	Increasing Γ , including homogenizer
Discussed in	Sections 3.3.2 and 4.2
Shown in	Figure 45d
Relevant sensors	$TT_{\text{sat}}, TT_{08}, TT_{07}, TT_{06}, TT_{05}$
Constant variables	$T_{\text{sat}} = 69.1^\circ\text{C}, T_{\text{wall}} = 83.4^\circ\text{C}, \text{Ja} = 25.7 \cdot 10^{-3} [-]$
Confidence interval	95%

$T_{\text{wall}} [^\circ\text{C}]$	$T_{\text{sat}} [^\circ\text{C}]$	$\text{Ja} \cdot 10^3 [-]$	$\Gamma \cdot 10^3 [\frac{\text{kg}}{\text{ms}}]$	$\dot{Q}_{8,\text{in}} [\text{W}]$	$\dot{Q}_{7,\text{in}} [\text{W}]$	$\dot{Q}_{6,\text{in}} [\text{W}]$	$\dot{Q}_{5,\text{in}} [\text{W}]$
83.4±0.1	69.1±0.1	25.7±0.3	12.1±0.3	202.3±36.0	303.2±58.7	414.6±57.4	483.7±28.9
83.4±0.1	69.1±0.1	25.7±0.3	13.0±0.3	224.6±63.3	333.6±55.9	465.8±39.9	465.2±25.4
83.4±0.1	69.1±0.1	25.7±0.3	14.0±0.3	321.9±93.5	376.7±62.5	480.4±29.2	456.3±21.7
83.4±0.1	69.1±0.1	25.7±0.2	14.8±0.3	350.8±68.0	436.0±52.4	467.5±22.3	460.6±21.7
83.4±0.1	69.1±0.1	25.7±0.2	15.5±0.3	353.6±63.4	465.7±37.1	447.0±22.3	468.4±21.0
83.4±0.0	69.1±0.1	25.7±0.2	16.3±0.1	397.6±22.2	472.1±27.3	438.4±18.8	473.4±21.8
83.4±0.0	69.1±0.1	25.7±0.2	16.9±0.1	401.8±15.2	462.1±20.3	431.0±18.7	479.3±22.5
83.4±0.0	69.1±0.1	25.7±0.2	17.5±0.1	398.6±9.2	445.0±14.8	431.6±18.1	484.8±21.1

Table 10: Dataset: Film heater heat removal rate $\dot{Q}_{i,\text{in}}$ at decreasing initial liquid film flow rate. Experimental set-up includes homogenizer. Data from 241 measurements points.

Measurement description	Increasing Γ , including homogenizer
Discussed in	Sections 3.3.2 and 4.2
Shown in	Figure 45e
Relevant sensors	$TT_{\text{sat}}, TT_{08}, TT_{07}, TT_{06}, TT_{05}$
Constant variables	$T_{\text{sat}} = 69.1^\circ\text{C}, T_{\text{wall}} = 89.4^\circ\text{C}, \text{Ja} = 36.5 \cdot 10^{-3} [-]$
Confidence interval	95%

$T_{\text{wall}} [^\circ\text{C}]$	$T_{\text{sat}} [^\circ\text{C}]$	$\text{Ja} \cdot 10^3 [-]$	$\Gamma \cdot 10^3 [\frac{\text{kg}}{\text{ms}}]$	$\dot{Q}_{8,\text{in}} [\text{W}]$	$\dot{Q}_{7,\text{in}} [\text{W}]$	$\dot{Q}_{6,\text{in}} [\text{W}]$	$\dot{Q}_{5,\text{in}} [\text{W}]$
89.4±0.1	69.1±0.1	36.5±0.3	15.6±0.4	518.6±41.1	447.7±129.8	641.3±61.4	624.1±25.3
89.4±0.1	69.1±0.1	36.5±0.3	16.4±0.3	501.3±70.7	546.1±101.5	650.8±20.5	613.0±25.1
89.4±0.1	69.1±0.1	36.5±0.3	17.3±0.2	541.8±40.3	605.2±84.2	625.4±23.7	615.9±25.7
89.4±0.1	69.1±0.1	36.5±0.2	18.0±0.2	560.5±24.6	645.3±37.5	603.7±20.6	620.2±25.8
89.4±0.1	69.1±0.1	36.5±0.2	18.7±0.1	561.3±21.5	642.4±38.5	592.1±20.4	626.8±25.8
89.4±0.0	69.1±0.1	36.5±0.2	19.2±0.2	549.3±14.9	607.9±27.6	582.1±18.6	627.3±27.9

Table 11: Dataset: Film heater heat removal rate $\dot{Q}_{i,\text{in}}$ at decreasing initial liquid film flow rate. Experimental set-up includes homogenizer. Data from 241 measurements points.

B.4 Data: Increasing saturation temperature

Measurement description	Increasing T_{sat} (film evaporation), including homogenizer
Discussed in	Sections 3.3.3 and 4.3
Shown in	Figure 47a
Relevant sensors	$TT_{\text{sat}}, TT_{08}, TT_{07}, TT_{06}, TT_{05}$
Constant variables	$\Gamma = 12.7 \cdot 10^{-3} \frac{\text{kg}}{\text{ms}}, \text{Ja} = 2.8 \cdot 10^{-3} [-]$
Confidence interval	95%

$T_{\text{wall}} [^\circ\text{C}]$	$T_{\text{sat}} [^\circ\text{C}]$	$\text{Ja} \cdot 10^3 [-]$	$\Gamma \cdot 10^3 [\frac{\text{kg}}{\text{ms}}]$	$\dot{Q}_{8,\text{in}} [\text{W}]$	$\dot{Q}_{7,\text{in}} [\text{W}]$	$\dot{Q}_{6,\text{in}} [\text{W}]$	$\dot{Q}_{5,\text{in}} [\text{W}]$
42.1±0.0	40.5±0.1	2.8±0.2	12.7±0.0	18.5±2.8	28.1±3.5	13.5±2.9	15.4±3.0
49.2±0.0	47.5±0.1	2.9±0.2	12.7±0.0	32.7±2.5	50.2±3.1	44.8±3.7	53.3±3.2
57.2±0.0	55.6±0.1	2.8±0.2	12.7±0.1	40.7±6.9	63.8±7.1	65.5±7.3	79.9±8.5
64.3±0.1	62.8±0.1	2.6±0.3	12.7±0.1	43.8±4.6	68.0±5.2	74.3±7.2	91.8±6.2
69.3±0.0	67.8±0.1	2.7±0.2	12.7±0.0	47.8±2.8	71.2±3.9	78.0±6.0	99.2±2.8
73.3±0.2	71.8±0.1	2.7±0.3	12.7±0.1	53.7±5.4	76.0±5.6	81.7±6.6	104.7±6.0
78.4±0.0	76.8±0.1	2.7±0.2	12.7±0.0	61.2±4.7	80.7±4.3	83.3±5.7	106.5±4.1
84.4±0.4	82.9±0.1	2.6±0.7	12.7±0.1	74.2±9.3	88.7±8.4	86.6±6.3	106.9±5.6

Table 12: Dataset: Film heater heat removal rate $\dot{Q}_{i,\text{in}}$ at varying saturation conditions. Experimental set-up includes homogenizer. Data from 181 measurements points.

Measurement description	Increasing T_{sat} (nucleate boiling), including homogenizer
Discussed in	Sections 3.3.3 and 4.3
Shown in	Figure 47b
Relevant sensors	$TT_{\text{sat}}, TT_{08}, TT_{07}, TT_{06}, TT_{05}$
Constant variables	$\Gamma = 14.3 \cdot 10^{-3} \frac{\text{kg}}{\text{ms}}, \text{Ja} = 11.2 \cdot 10^{-3} [-]$
Confidence interval	95%

$T_{\text{wall}} [^{\circ}\text{C}]$	$T_{\text{sat}} [^{\circ}\text{C}]$	$\text{Ja} \cdot 10^3 [-]$	$\Gamma \cdot 10^3 [\frac{\text{kg}}{\text{ms}}]$	$\dot{Q}_{8,\text{in}} [\text{W}]$	$\dot{Q}_{7,\text{in}} [\text{W}]$	$\dot{Q}_{6,\text{in}} [\text{W}]$	$\dot{Q}_{5,\text{in}} [\text{W}]$
47.2±0.7	40.7±0.1	11.2±1.3	14.3±0.1	163.3±8.8	182.3±10.8	171.2±13.5	173.5±12.1
54.2±0.6	47.8±0.1	11.1±1.1	14.3±0.1	170.6±6.9	198.2±7.4	205.6±11.7	221.1±9.2
62.3±0.7	55.9±0.1	11.0±1.1	14.3±0.1	166.9±7.2	198.6±7.2	215.7±12.7	239.1±11.0
69.3±0.7	63.1±0.1	10.9±1.2	14.3±0.1	170.1±6.5	201.1±7.0	222.7±12.3	251.8±11.3
74.3±0.8	68.1±0.1	10.9±1.4	14.3±0.1	172.6±7.2	198.7±7.7	219.2±13.4	251.4±11.3
78.4±0.7	72.2±0.1	10.8±1.2	14.3±0.1	180.3±6.8	199.6±7.1	219.1±12.6	256.8±10.2
83.4±0.8	77.2±0.1	10.8±1.5	14.3±0.1	186.4±10.1	210.7±8.9	222.1±11.7	260.3±10.8
89.4±1.4	83.3±0.1	10.7±2.4	14.3±0.1	203.7±30.1	234.7±16.7	234.1±12.7	265.4±10.0

Table 13: Dataset: Film heater heat removal rate $\dot{Q}_{i,\text{in}}$ at varying saturation conditions. Experimental set-up includes homogenizer. Data from 181 measurements points.

Measurement description	Increasing T_{sat} (nucleate boiling), including homogenizer
Discussed in	Sections 3.3.3 and 4.3
Shown in	Figure 47c
Relevant sensors	$TT_{\text{sat}}, TT_{08}, TT_{07}, TT_{06}, TT_{05}$
Constant variables	$\Gamma = 15.7 \cdot 10^{-3} \frac{\text{kg}}{\text{ms}}, \text{Ja} = 18.2 \cdot 10^{-3} [-]$
Confidence interval	95%

$T_{\text{wall}} [^{\circ}\text{C}]$	$T_{\text{sat}} [^{\circ}\text{C}]$	$\text{Ja} \cdot 10^3 [-]$	$\Gamma \cdot 10^3 [\frac{\text{kg}}{\text{ms}}]$	$\dot{Q}_{8,\text{in}} [\text{W}]$	$\dot{Q}_{7,\text{in}} [\text{W}]$	$\dot{Q}_{6,\text{in}} [\text{W}]$	$\dot{Q}_{5,\text{in}} [\text{W}]$
51.2±1.0	40.7±0.1	18.2±1.8	15.7±0.1	296.8±10.2	318.0±11.0	299.4±17.2	325.6±16.7
58.2±1.2	47.8±0.1	18.1±2.1	15.7±0.1	291.5±8.0	329.1±9.2	327.7±16.7	353.0±15.3
66.3±1.1	56.0±0.1	17.8±1.9	15.7±0.1	279.3±9.2	321.1±10.3	331.6±16.9	367.8±16.1
73.3±1.1	63.2±0.1	17.7±1.9	15.7±0.1	278.1±7.4	316.4±9.6	335.0±16.5	378.8±17.0
78.4±1.2	68.3±0.1	17.6±2.0	15.7±0.1	280.7±9.1	311.7±9.9	328.8±17.6	376.2±17.9
82.4±1.3	72.3±0.1	17.6±2.3	15.7±0.1	293.1±12.9	320.5±9.2	332.9±17.4	384.3±18.7
87.4±1.4	77.4±0.1	17.4±2.4	15.7±0.1	323.2±19.9	330.0±12.5	331.5±17.3	384.0±18.6
93.5±2.3	83.5±0.1	17.3±4.0	15.7±0.2	287.2±53.2	360.7±21.3	342.2±16.4	385.2±18.1

Table 14: Dataset: Film heater heat removal rate $\dot{Q}_{i,\text{in}}$ at varying saturation conditions. Experimental set-up includes homogenizer. Data from 181 measurements points.

B.5 Data: Increasing ΔT , excluding homogenizer

Measurement description	Increasing ΔT , excluding homogenizer
Discussed in	Sections 3.3.6 and 4.6
Shown in	Figure 54
Relevant sensors	$TT_{\text{sat}}, TT_{08}, TT_{07}, TT_{06}, TT_{05}$
Constant variables	$T_{\text{sat}} = 69.1^\circ\text{C}, \Gamma = 13.3 \cdot 10^{-3} \frac{\text{kg}}{\text{ms}}$
Confidence interval	95%

$T_{\text{wall}} [^\circ\text{C}]$	$T_{\text{sat}} [^\circ\text{C}]$	$\Gamma \cdot 10^3 [\frac{\text{kg}}{\text{ms}}]$	$Ja \cdot 10^3 [-]$	$\dot{Q}_{8,\text{out}} [\text{W}]$	$\dot{Q}_{7,\text{out}} [\text{W}]$	$\dot{Q}_{6,\text{out}} [\text{W}]$	$\dot{Q}_{5,\text{out}} [\text{W}]$
70.3±0.0	69.1±0.1	13.3±0.0	2.2±0.2	49.3±3.7	66.2±4.9	56.6±3.4	68.6±2.4
71.3±0.0	69.1±0.1	13.3±0.0	4.0±0.2	71.9±9.8	100.3±8.1	85.3±5.1	98.2±2.5
72.3±0.0	69.1±0.1	13.4±0.1	5.8±0.2	96.8±15.3	128.3±11.7	122.6±7.6	131.9±2.9
73.3±0.0	69.1±0.1	13.4±0.1	7.7±0.2	96.4±17.2	143.7±15.7	165.4±11.6	166.6±4.0
75.3±0.1	69.1±0.1	13.3±0.1	11.3±0.2	113.8±23.6	170.1±20.9	224.6±19.0	237.0±10.7
77.4±0.1	69.1±0.1	13.4±0.2	14.9±0.2	132.3±26.3	195.8±25.5	265.9±28.6	308.6±16.1
79.4±0.1	69.1±0.1	13.4±0.2	18.5±0.2	142.2±29.2	208.6±24.5	287.0±43.2	370.3±20.5
81.4±0.1	69.1±0.1	13.5±0.2	22.1±0.3	155.8±44.0	237.0±25.8	305.4±44.0	430.7±25.5
83.4±0.1	69.1±0.1	13.3±0.3	25.7±0.3	160.9±54.3	235.7±37.8	316.3±51.1	485.8±35.9
85.4±0.1	69.1±0.1	13.3±0.4	29.3±0.3	162.2±64.7	245.0±56.6	355.0±47.4	540.4±44.5
87.4±0.2	69.1±0.1	13.3±0.4	32.9±0.3	170.0±70.6	226.3±78.5	393.0±64.8	597.0±44.5
89.4±0.2	69.1±0.1	13.3±0.5	36.5±0.4	170.7±71.4	203.6±86.0	417.3±67.9	631.7±64.2

Table 15: Dataset: Film heater heat removal rate $\dot{Q}_{i,\text{in}}$, as a function of the degree of superheating, expressed with the Jakob number ($Ja [-]$). Experimental set-up does not include homogenizer. Data from 241 measurements points.

B.6 Data: Saturation temperature development

Measurement description	Increasing T_{sat}
Discussed in	Sections 3.3.4 and 4.4
Shown in	Figure 49
Relevant sensors	$TT_{\text{sat}}, \text{rotameter}$
Confidence interval	95%

$\Phi [\frac{1}{h}]$	$\dot{Q}_{\text{in}} [\text{W}]$	$T_{\text{sat}} [^\circ\text{C}]$	$T_{\text{in}} [^\circ\text{C}]$	$T_{\text{out}} [^\circ\text{C}]$	$\frac{\dot{Q}_{\text{out}}}{\dot{Q}_{\text{in}}} [\%]$
229.9±13.0	8769.1±132.9	70.5±0.2	15.5±0.0	45.1±0.1	89.6±5.1
229.9±13.0	8322.9±70	69.5±0.2	15.5±0.0	44.4±0.1	92.4±5.3
229.9±13.0	7200.0±0.0	65.9±0.2	15.5±0.0	40.8±0.1	93.4±5.3
229.9±13.0	6171.4±31.4	62.6±0.2	15.4±0.0	37.7±0.1	96.0±5.5
229.9±13.0	4800.0±0.0	57.6±0.2	15.4±0.0	32.9±0.1	97.2±5.5
229.9±13.0	3600.0±0.0	53.4±0.2	15.3±0.0	28.7±0.1	99.5±5.7
229.9±13.0	2400.0±0.0	49.2±0.2	15.2±0.0	24.3±0.1	101.2±5.8
229.9±13.0	1200.0±0.0	46.1±0.2	15.2±0.0	19.8±0.1	101.7±6.1

$\Phi \left[\frac{1}{h}\right]$	$\dot{Q}_{in} [W]$	$T_{sat} [^{\circ}C]$	$T_{in} [^{\circ}C]$	$T_{out} [^{\circ}C]$	$\frac{\dot{Q}_{out}}{\dot{Q}_{in}} [\%]$
470.4±13.0	9600.0±0.0	62.2±0.2	15.3±0.0	31.3±0.1	90.9±2.6
470.4±13.0	8503.0±25.9	59.5±0.2	15.3±0.0	29.7±0.1	92.0±2.6
470.4±13.0	7200.0±0.0	55.9±0.2	15.3±0.0	27.1±0.1	89.5±2.6
470.4±13.0	6111.6±37	53.1±0.2	15.1±0.0	25.1±0.1	89.9±2.6
470.4±13.0	4800.0±0.0	49.6±0.2	14.9±0.0	22.8±0.1	90.1±2.7
470.4±13.0	3600.0±0.0	46.7±0.2	14.9±0.0	20.8±0.1	90.6±2.9
470.4±13.0	2400.0±0.0	44.5±0.2	14.9±0.0	18.9±0.1	90.6±3.2
470.4±13.0	1200.0±0.0	43.3±0.2	14.8±0.0	16.8±0.1	90.1±4.7

$\Phi \left[\frac{1}{h}\right]$	$\dot{Q}_{in} [W]$	$T_{sat} [^{\circ}C]$	$T_{in} [^{\circ}C]$	$T_{out} [^{\circ}C]$	$\frac{\dot{Q}_{out}}{\dot{Q}_{in}} [\%]$
960.9±13.0	9600.0±0.0	48.3±0.2	14.9±0.0	22.7±0.1	90.5±1.6
960.9±13.0	8474.2±27.5	47.0±0.2	14.5±0.0	21.4±0.1	90.9±1.7
960.9±13.0	7200.0±0.0	45.4±0.2	14.4±0.0	20.2±0.1	89.6±1.8
960.9±13.0	6101.4±37.1	44.3±0.2	14.3±0.1	19.3±0.1	91.1±2.0
960.9±13.0	4800.0±0.0	43.1±0.2	14.3±0.0	18.2±0.1	90.2±2.4
960.9±13.0	3600.0±0.0	42.3±0.2	14.4±0.0	17.4±0.1	91.7±3.0
960.9±13.0	2400.0±0.0	41.9±0.2	14.5±0.0	16.5±0.1	91.8±4.3
960.9±13.0	1200.0±0.0	41.3±0.2	14.5±0.0	15.5±0.1	90.4±8.3

$\Phi \left[\frac{1}{h}\right]$	$\dot{Q}_{in} [W]$	$T_{sat} [^{\circ}C]$	$T_{in} [^{\circ}C]$	$T_{out} [^{\circ}C]$	$\frac{\dot{Q}_{out}}{\dot{Q}_{in}} [\%]$
1331.5±13.0	9600.0±0.0	44.7±0.2	14.3±0.0	19.9±0.1	90.5±1.7
1331.5±13.0	8429.7±25.6	43.8±0.2	14.4±0.0	19.4±0.1	91.3±1.9
1331.5±13.0	7200.0±0.0	42.7±0.2	14.2±0.0	18.4±0.1	89.8±2.1
1331.5±13.0	6051.3±43.2	42.0±0.2	14.3±0.0	17.8±0.1	89.4±2.4
1331.5±13.0	4800.0±0.0	41.4±0.2	14.2±0.0	17.0±0.1	89.5±3.0
1331.5±13.0	3600.0±0.0	40.9±0.2	14.2±0.0	16.3±0.1	89.1±3.9
1331.5±13.0	2400.0±0.0	40.7±0.2	14.6±0.0	15.9±0.1	86.2±5.9
1331.5±13.0	1200.0±0.0	40.5±0.2	14.8±0.0	15.5±0.1	84.8±11.4

$\Phi \left[\frac{1}{h}\right]$	$\dot{Q}_{in} [W]$	$T_{sat} [^{\circ}C]$	$T_{in} [^{\circ}C]$	$T_{out} [^{\circ}C]$	$\frac{\dot{Q}_{out}}{\dot{Q}_{in}} [\%]$
1703.2±13.0	9600.0±0.0	43.9±0.2	15.6±0.0	19.9±0.1	88.9±2.0
1703.2±13.0	8355.6±24	43.0±0.2	15.9±0.0	19.6±0.1	87.8±2.2
1703.2±13.0	7200.0±0.0	41.9±0.2	15.8±0.0	19.0±0.1	87.7±2.6
1703.2±13.0	6093.7±35.6	41.0±0.2	15.0±0.0	17.7±0.1	86.9±2.9
1703.2±13.0	4800.0±0.0	40.3±0.2	14.5±0.0	16.6±0.1	86.8±3.8
1703.2±13.0	3600.0±0.0	39.9±0.2	14.4±0.0	16.0±0.1	86.7±5.0
1703.2±13.0	2400.0±0.0	39.7±0.2	14.6±0.0	15.6±0.1	81.5±7.5
1703.2±13.0	1200.0±0.0	39.4±0.2	14.3±0.0	14.8±0.1	76.5±14.6

Table 16: Dataset: Variation of saturation conditions and measured heat extraction rate with varying heat flow rate. Experimental set-up includes homogenizer. Data from 181 measurements points.

C Appendix III: Sensor calibration

C.1 Calibration: Thermocouple temperature transmitters

Figure 55 shows the calibration of the sheath thermocouple temperature transmitters against a previously calibrated accurate resistance temperature transmitter in a dry block calibrator. Please note that the read-out resolution of the temperature probes is limited to 1.0°C .

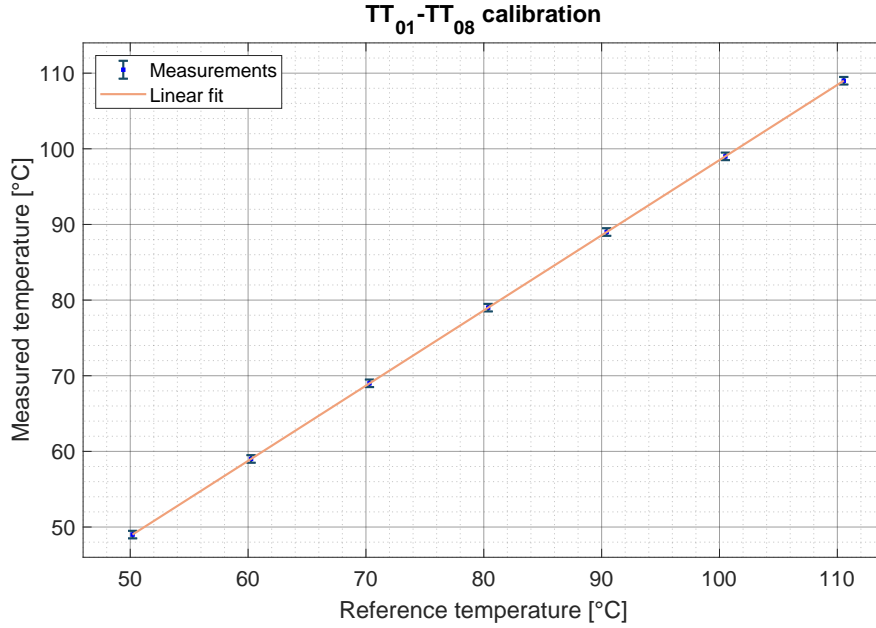


Figure 55: Calibration of $\text{TT}_{01}\text{-TT}_{08}$ against more accurate thermometer in dry block calibrator for relevant temperature range. The linear fit through the calibration results (found from equation (59)) is shown in orange.

Here, the thermocouples are found to underestimate the reference temperature continuously within the relevant domain. Using equation 59, found from the calibration depicted in figure 55, an expression for the estimated temperature T_{est} can be found with the measured temperature T_m . An estimate for the systematic standard uncertainty in the calibration correction of the temperature transmitter \bar{s}_{cal} is given in equation (60).[69]

$$T_{\text{est}} = 1.006(T_m - 80) + 81.3780 \quad (59)$$

$$\bar{s}_{\text{cal}} = \pm 6.2 \cdot 10^{-3} \text{ } ^{\circ}\text{C} \quad (95\%) \quad (60)$$

By positioning the transmitter probes in the heater hot spots, the greatest temperature at the evaporator wall is known and can be controlled. The thermocouple transmitters are placed consistently at 25mm (tangentially) from the heater center, and 25.5mm (vertically) from the heater edge, at one of the two heater hot spots (see section 3.1.3.2).

C.2 Calibration: Resistance temperature transmitters

Temperature transmitters TT_{sat} and TT_{top} [A10] are also calibrated against an accurate temperature transmitter using a dry block calibration device. Both TT_{sat} and TT_{top} are resistance temperature detectors, placed directly into the central heatpipe tube of the experimental setup.

Figure 56 shows the calibration of TT_{top} .

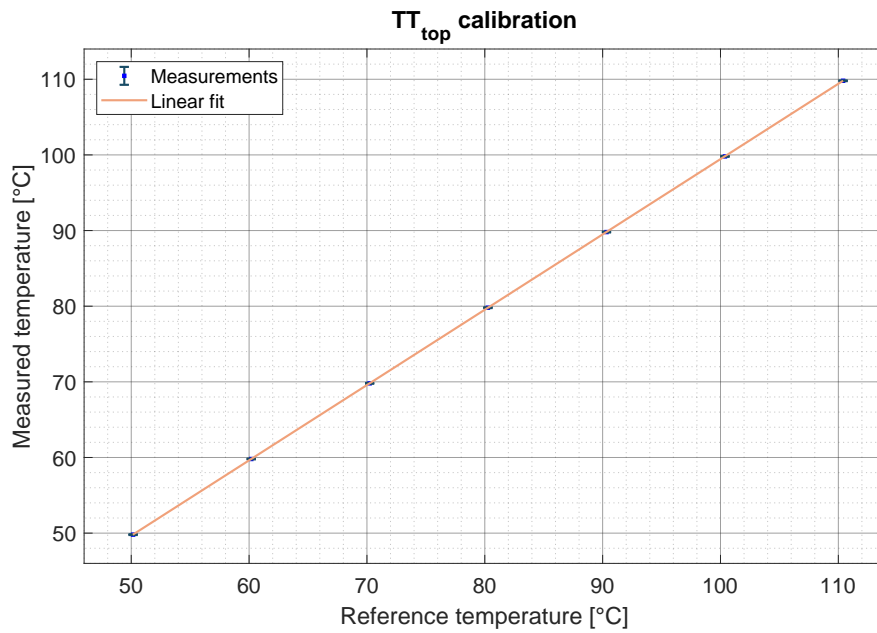


Figure 56: Calibration of TT_{top} against more accurate thermometer thermometer in dry block calibrator for relevant temperature range. The linear fit through the calibration results (found from equation (61)) is shown in orange.

A temperature measurement T_m of probe TT_{top} can be converted to a more accurate estimated temperature T_{est} with the use of equation (61). Please note that equation (61) has been found using a fit through the calibration results. An estimate for the systematic standard uncertainty in the calibration correction of the temperature transmitter \bar{s}_{cal} is given in equation (62).

$$T_{est} = 1.0044(T_m - 80) + 80.4679 \quad (61)$$

$$\bar{s}_{cal} = \pm 1.2 \cdot 10^{-2} \text{ } ^\circ\text{C} \quad (95\%) \quad (62)$$

Figure 56 shows the calibration of TT_{sat} .

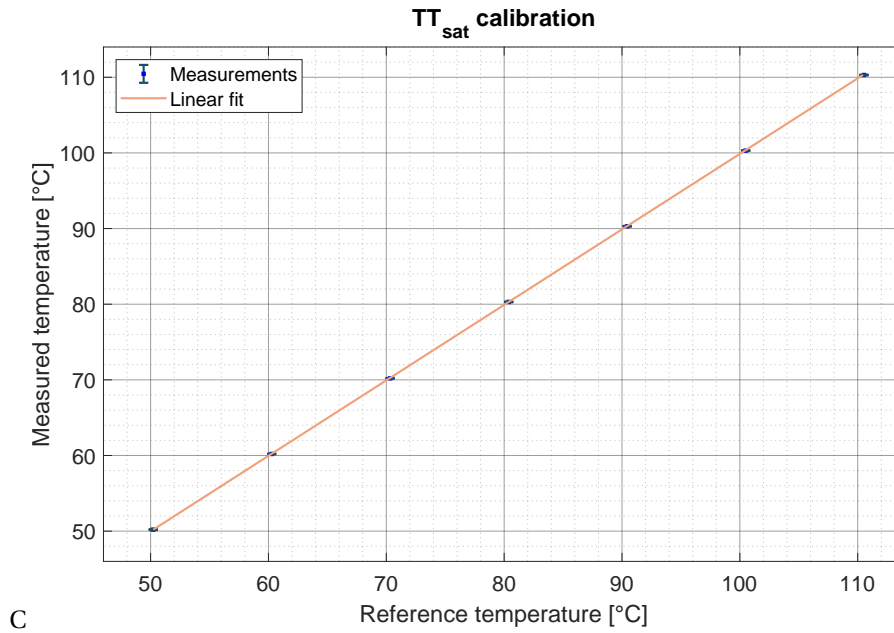


Figure 57: Calibration of TT_{sat} against more accurate thermometer thermometer in dry block calibrator for relevant temperature range. The linear fit through the calibration results (found from equation (63)) is shown in orange.

A temperature measurement T_m of probe TT_{sat} can be converted to a more accurate estimated temperature T_{est} with the use of equation (63). Please note that equation (63) has been found using a fit through the calibration results. An estimate for the systematic standard uncertainty in the calibration correction of the temperature transmitter \bar{s}_{cal} is given in equation (64).

$$T_{\text{est}} = 1.002 (T_m - 80) + 80.0864 \quad (63)$$

$$\bar{s}_{\text{cal}} = \pm 4.2 \cdot 10^{-2} \text{ } ^\circ\text{C} \text{ (95\%)} \quad (64)$$

Temperature transmitters TT_{out} and TT_{in} [A9] are, contrary to the previously discussed transmitters, used for a differential temperature measurement. It is of importance to know whether temperature readings originating from the two temperature transmitters are the same for an equal reference temperature. As such, TT_{out} and TT_{in} are calibrated by placing both transmitters on the same surface, and heating this surface within the relevant temperature range. TT_{out} is found to give greater readings than TT_{in} within the specified range, as can be seen in figure 58.

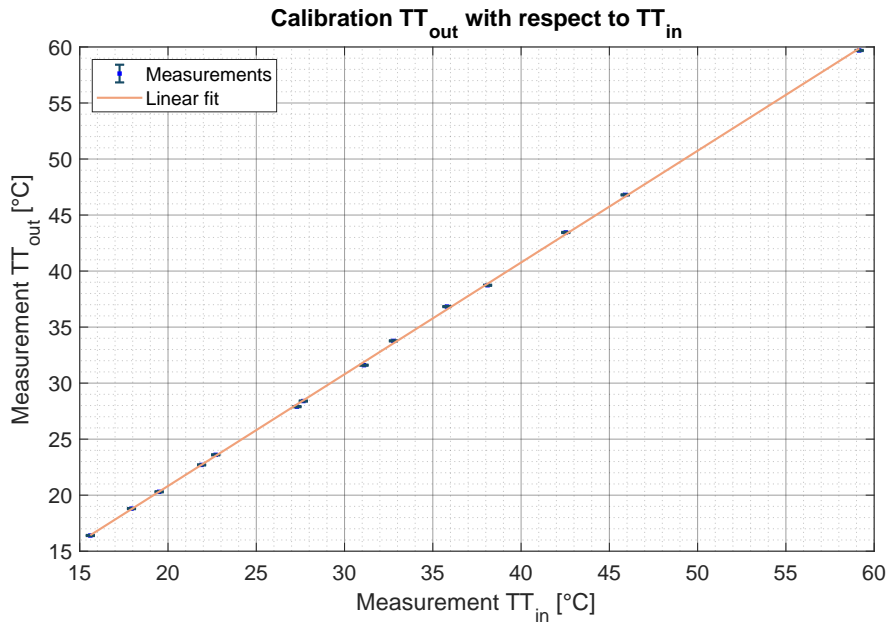


Figure 58: Calibration of TT_{out} against TT_{in} for relevant temperature range. The linear fit through the calibration results (found from equation (65)) is shown in orange.

In order to reduce the difference in temperature between TT_{out} and TT_{in} for a same reference temperature, TT_{out} can be corrected with equation (65). Equation (65) is found from a linear fit through the measurements of TT_{out} with respect to the measurements of TT_{in} . An estimate for the systematic standard uncertainty in the calibration correction of TT_{out} \bar{s}_{cal} is given in equation (66).

$$T_{est} = \frac{T_m - 0.8691}{0.9974} \quad (65)$$

$$\bar{s}_{cal} = \pm 8.8 \cdot 10^{-2} \text{ } ^\circ\text{C} \quad (95\%) \quad (66)$$

In order to find an accurate estimation of the temperature difference between the in-flowing cooling water and the out-flowing cooling water, the measurements of TT_{in} should not be corrected.

C.3 Calibration: Flowmeter

The flow rate, in liters per hour, of the cooling water stream is measured using a rotameter. By comparing the rotameter reading to a change in weight of a bucket filled with cooling water, Hogendoorn[33] was able to quantify the rotameter error. An approximation of the estimated flow rate Φ_{est} can be found from the measured flow rate Φ_m using equation (67). An estimate for the systematic standard uncertainty in the calibration correction of the rotameter \bar{s}_{cal} is given in equation (67).

$$\Phi_{est} = \Phi_m - (13.744 \cdot \ln(\Phi_m) - 55.805) \quad (67)$$

$$\bar{s}_{cal} = \pm 3.7 \cdot 10^0 \frac{\text{L}}{\text{h}} \quad (95\%) \quad (68)$$

D Appendix IV: Heatpipe materials & stress analysis

The following paragraphs will aim to defend the choice of continuing the operation of the heatpipe with the already existing setup from a heatpipe-materials perspective. A brief simplified analysis of the mechanical strength of the heatpipe tube is performed.

The existing system has been partially erected from borosilicate glass, and partially erected from copper. A copper tube was initially selected as a result of the large thermal conductivity of copper. As such, the conduction resistance (and temperature drop) through the copper evaporator- and condenser walls is small. In order to be able to visually inspect the heatpipe interior during measurements, the heatpipe was to contain several transparent glass sections. The mechanical applicability and strength of both material choices is considered. As copper is ductile and glass is brittle, the strength and failure of both material types will be discussed below.

Consider a heatpipe using water as its medium. The heatpipe material has to be able to withstand operation at external pressures resulting from operation below atmospheric pressure. Only thin-walled cylinders will be considered in the following paragraphs. A cylinder is considered thin-walled when $\frac{t}{D} < 10$. [70] At external pressures, cylinders may fail as a result of plastic failure, fracture or as a result of buckling. Operational criteria based on the former mode of failure may be formed through a comparison of some equivalent stress with the material yield stress or the ultimate stress. For pressure vessels an equivalent stress is often found from a summation of the axial stress, the bending stress, any torsional stresses and the hoop stress. A simplified analysis can be performed when only considering pressure-induced stresses on the heatpipe. The stress in tangential direction (hoop stress) can be found from a force balance on the cylinder cross section (a hemicylinder), and is denoted in equation (69). [70], [71] An additional force is exerted on the cylinder ends as a result of an external pressure, resulting in the axial stress denoted per equation (70).

$$\sigma_h = \frac{p_e D_e}{2t} \quad (69)$$

$$\sigma_a = \frac{p_e D_e}{4t} \quad (70)$$

Here D_e is the external tube diameter, and p_e is the external pressure with reference to the interior pressure in the heatpipe. Generally, ductile materials will fail after the initiation of yielding, whilst brittle materials will fail by fracture after loading. An equivalent stress can be found for the simplified case using the Von Mises theory for isotropic ductile materials. Provided equation (71) holds, the tube wall will be held from yielding. [72]

$$\sqrt{\sigma_h^2 - \sigma_h \sigma_a + \sigma_a^2} \leq \sigma_y \quad (71)$$

Here σ_y is the yield stress of a material. For brittle materials, a maximum to the stress state can be found through separate comparison of the normal stress components with the ultimate stress σ_{ult} for a material subject to either compression or tension. An isotropic brittle material is believed to refrain from fracturing if equation (72) holds.

$$|\sigma_i| \leq \sigma_{ult} \quad (72)$$

Thin-walled cylinders are however also susceptible to buckling when loaded externally, with ovalization of the cylinder being the most critical buckling form. [70] The critical external pressure at which a thin-walled cylinder will be prone to buckle is given in equation (73).

$$p_{ce} = \frac{2E}{1-\nu^2} \left(\frac{t}{D_e} \right)^3 \quad (73)$$

In equation (73) E represents the material's Young's modulus, and ν is the Poisson's ratio. The equation has been derived for infinitely long cylinders, but gives agreeable results for unsupported (no stiffening rings) sections of tube with lengths upwards of ten times the diameter. [70] Annaratone et al. argue that the failure of not perfectly circular cylinders occurs before the prediction of equations (69) and (71) suggest. [70] Formulae as functions of the average deviation from roundness of the tube are presented in their

work.

As the saturation temperature in the heatpipe increases, the pressure in the column increases accordingly. Above some temperature, the pressure inside the tube will exceed the atmospheric pressure surrounding the tube. Failure criteria can be found in similar fashion to the externally pressurized configuration, as discussed above (excluding buckling). When under tension, brittle materials tend to fail by the propagation of cracks in the material (fracture). The increased local stress as a result of a decrease in area at the crack allow for crack propagation in brittle materials, and possibly failure significantly before the yield stress is reached.[53] In order to avoid a violent rupture of a brittle heatpipe material, additional safety precautions are required. If the wall can withstand fracture in the presence of a leak (crack with length of wall thickness), the heatpipe will leak prior to rupturing entirely. As such, the consequences of failure are kept to a minimum. If equation (74) holds, a leak with length t will not result in failure of the entire solid body.[53]

$$p_i \leq \frac{2}{Y^2 \pi D_e} \left(\frac{K_{1c}^2}{\sigma_y} \right) \quad (74)$$

Here, constant Y depends on the considered geometry and has a value near unity, and K_{1c} is the fracture toughness of the considered material. p_i is the internal pressure of the tube with respect to the atmospheric pressure. Equation (74) gives an upper limit to the operating pressure of the system. In order to ensure that this pressure limit is not reached, a release valve was added to the heatpipe, preventing the build-up of pressure beyond some threshold below the maximum defined in equation (74).

Using material data from Granta EduPack[68] for the above analysis, the current materials can be assessed. In each case, the most restrictive material property combination has been considered. Both the copper and the glass sections of the heatpipe can withstand pressure differences (when loaded externally) significantly greater (more than one order of magnitude) than what they are subject to in the experimental setup. When loaded under tension, however, the internal pressure of the glass is limited by its crack propagation resistance, as per equation (74). At an over-pressure of $p_i \approx 1$ bar, a crack with a length of t will result in failure of the glass section. As such, the existing release valve (3 bar absolute pressure[33]) has been under-designed, and should be adjusted to open at an absolute pressure below 2 bar. As a result, the operating (saturation) temperature of the heatpipe has an upper limit of 120°C.[6]

As wall sections become subject to (transient) heat fluxes, or inhomogeneous heating, the material will experience stress as a result of thermal expansion and restrictions to expansion. The elongation of a cylinder in the axial direction is constant in the radial direction, i.e. $\frac{d\epsilon_a}{dr} = 0$. [70] With a centrifugal flux, a stress is induced in the material as both sides will experience the same elongation. This thermal stress scales with the temperature difference between the two sides of the wall and the thermal expansion coefficient of the wall material.[70] As a result of local tensile stress induced by a (transient) temperature gradient, cracks may suddenly propagate, resulting in failure of the brittle glass. With respect to glasses in general, borosilicate glasses have low thermal expansion coefficients.[68] As such, borosilicate glass is more suitable for use in a heatpipe than other glasses. As an additional safety precaution a polymer film is applied to the outside of any glass sections, to prevent the discharge of glass particles into the surroundings of the heatpipe during unexpected fracture as a result of thermal shock.

E Appendix V: Numerical model

The following paragraphs will serve to introduce a numerical model, used to quantify and visualize the theory of section 2. The numerical model gives an estimation of the local temperature distribution of a heatpipe evaporator wall, and is used as a comparison of theoretical approximations and experimental data originating from this work.

The rate of heat transfer in the evaporation varies with the film Reynolds number, or with the degree of overheating, as discussed in section 2.1. As heat to the evaporator is supplied in separate heated rings, the evaporator wall temperature will be inhomogeneous over the evaporator height. As both the local rate of heat removal and the local rate of film evaporation depend on the local wall temperature, the wall temperature is to be approximated. A numerical model for the temperature distribution of the heatpipe evaporator is employed, and is discussed in the following paragraphs. The rectangular domain considered in the model is depicted in figure 59.

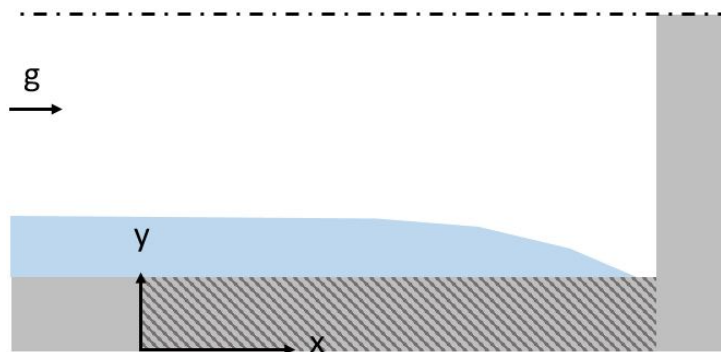


Figure 59: Schematic of numerical model domain, depicting a slice of the heatpipe evaporator. Numerical domain depicted with shaded region evaporator wall.

The model will serve as a reference for the quantification of the increase in wall temperature (at constant flux) or the decrease in heat removal (at constant temperature) as a result of film dry-out in the experimental setup. Furthermore, the model may provide insight in the influence of material- and fluid properties on heat removal, temperature distribution and film thickness in a heatpipe evaporator.

E.1 Assumptions

In the model, the temperature distribution throughout the evaporator wall for a heatpipe subject to film evaporation is approximated using a finite-difference method. The finite difference model is further explained in section E.2. In the following paragraphs, the underlying assumptions of the finite difference model are listed and briefly discussed.

The heatpipe is considered to operate in the absence of a liquid pool. The circulated fluid massflow in the evaporator is equal to the amount of evaporated liquid per unit time. A steady, one-dimensional film is considered. As such, any flow not parallel to the evaporator wall is neglected. The influence of condensation and evaporation on the interfacial shear of the liquid film, as previously discussed in section 2.1.3, is however considered when approximating the film thickness. The formation and propagation of waves at the film interface is not modeled, its effects are however included in the approximation of the heat removal at the evaporator wall. Please note that as a result the film thickness may be overestimated with 15%. [9], [10] The evaporator wall is modeled as a semi-infinite plate, neglecting its curvature and the curvature of the film. The work of Soliman et al. discusses the deviation from Nusselt's approximation for laminar condensation on curved surfaces. [73] The deviation from the average Nusselt thickness (δ_{Nu})

found per equation 4 for a shear-less interface at an inner radius r_i is expressed with equation (75).

$$\frac{\delta}{\delta_{Nu}} = \frac{\pm \left(1 - \sqrt{1 \mp 2 \frac{\delta_{Nu}}{r_i}} \right)}{\frac{\delta_{Nu}}{r_i}} \quad (75)$$

Using a film thickness of 0.2 mm (conservative estimation for expected heat flow through experimental apparatus) and a 2 inch copper tube, the film thickness is expected to deviate 0.2% from the Nusselt approximation. A greater deviation from reality is found when modeling the conduction through the evaporator wall. Using constant heatflow through the cylinder wall in radial direction, $R = \frac{\ln(D_o/D_i)}{2\pi kL}$ is found as an expression for the thermal resistance of conduction through the cylinder.[8] When approximating the heat transfer resistance using conduction through a slab, the conduction resistance is overestimated with 2.9% for the tube geometry of the experimental setup. The overestimation decreases with increasing tube radius, or with decreasing wall thickness.

For water, the turbulent transition of the liquid film, approximated through equation (10),[11] occurs only at heat flows significantly beyond the operating envelope of the experimental heatpipe (as depicted in figure 60). As such, the heat removal by film evaporation in a turbulent film is not included in the model.

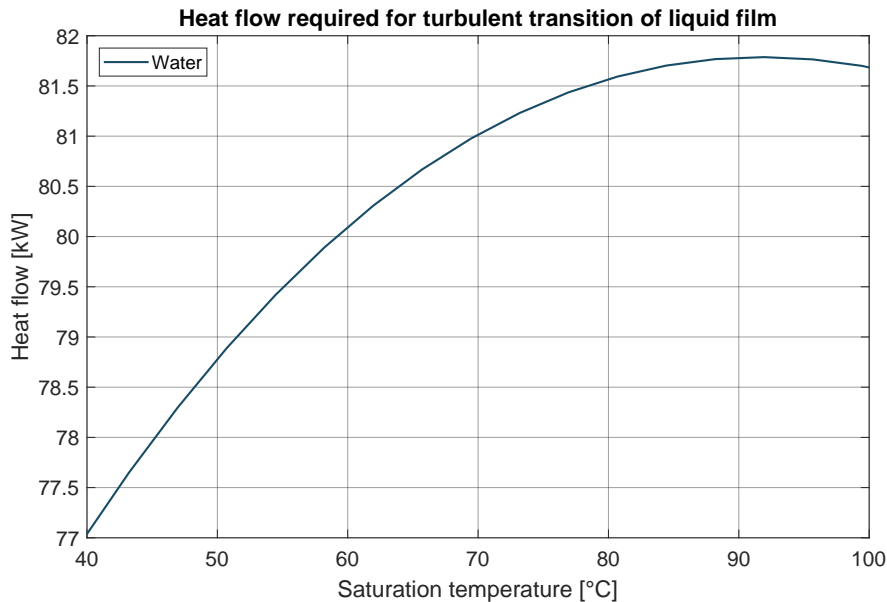


Figure 60: Evaporator heat flow at transition to turbulent film flow, as per [11]

At all times, the heat is assumed to be supplied homogeneously over the perimeter, resulting in the absence of temperature variations in the tangential direction, allowing for the possibility of two-dimensional conduction modeling. The evaporation of the liquid film is modeled to take place at the direct height at which heat is supplied to the film, neglecting the possible movement of vapour bubbles as discussed in section 2.1. Material properties are evaluated at the bulk temperature of the liquid film at a certain height along the evaporator, whilst below the saturation conditions. The bulk temperature of a liquid film can be found through equation (76).

$$T_b = \frac{\int_0^{\delta(x)} \rho_l u(y) c_{p,l} T(y) dy}{\int_0^{\delta(x)} \rho_l u(y) c_{p,l} dy} \quad (76)$$

As discussed in section 2.1.1, for thin liquid films all heat can be assumed to be transported per conduction. As such, the temperature profile across the film $T(y)$ is linear during film condensation and film

evaporation. The film-interface temperature does not rise beyond the saturation temperature. In nucleate boiling regions, however, the film temperature profile more resembles a turbulent film temperature profile as a result of mixing after bubble departure.[8] As such, the actual temperature profile $T(y)$ will deviate from the above discussed linear approximation in the nucleate boiling sections.

E.2 Finite difference & governing equations

The model is to solve a two-dimensional steady conduction equation. As no heat sources or sinks are present within the domain, equation (77) is found.

$$\frac{\partial^2 T}{\partial x^2} + \frac{\partial^2 T}{\partial y^2} = 0 \quad (77)$$

First, consider a one-dimensional conduction problem with a distance h_x between consecutive nodes. The solution at location x_i will be denoted as T_i . Assuming sufficiently smooth T , the value at nodes neighbouring T_i (at $(x_i + h_x)$ and $(x_i - h_x)$ respectively) can be found through Taylor expansion: [74]

$$T_{i+1} = T_i + h_x \frac{dT}{dx}(x_i) + \frac{h_x^2}{2!} \frac{d^2 T}{dx^2}(x_i) + \frac{h_x^3}{3!} \frac{d^3 T}{dx^3}(x_i) + O(h_x^4) \quad (78)$$

$$T_{i-1} = T_i - h_x \frac{dT}{dx}(x_i) + \frac{h_x^2}{2!} \frac{d^2 T}{dx^2}(x_i) - \frac{h_x^3}{3!} \frac{d^3 T}{dx^3}(x_i) + O(h_x^4)$$

The second derivative at x_i can be found by subtraction of the terms in equation (78), and is denoted in equation (79).

$$\frac{T_{i-1} - 2T_i + T_{i+1}}{h_x^2} = \frac{d^2 T}{dx^2}(x_i) + O(h_x^2) \quad (79)$$

The truncation error as a result of the above expansion scales with h_x^2 . The discretization of the second derivative in the y -direction is found analogously. In order to define a set of equations for the two-dimensional conduction problem, it is of importance to divide the domain in cells, and assign points at which T is determined (nodes). The grid used throughout this work is depicted in figure 61.

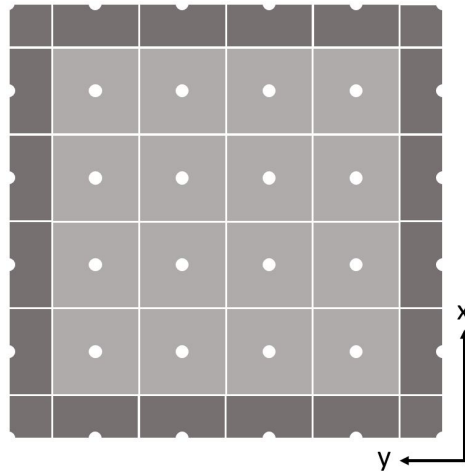


Figure 61: Simplified grid schematic, nodes depicted in white, boundary cells in dark grey, interior cells in light grey.

In figure 61, nodes are depicted in white. Any interior cells, cells not adjacent to a domain boundary, are depicted in a light(er) shade of grey. Please note that cells at the boundary (dark grey shading) deviate in size from interior cells. A set of equations can be defined if the cells are ordered lexicographically. The node index increases in the negative y -direction, with the indexing starting from the node in the bottom

left corner in figure 61. After having indexed an entire row of nodes, nodes of the row above are indexed. If the number of nodes in y -direction is equal to m and the number of nodes in x -direction is equal to n , the discretization can be denoted as per equation (80).

$$\frac{d^2 T_i}{dx^2} + \frac{d^2 T_i}{dy^2} \approx \frac{T_{i-m} - 2T_i + T_{i+m}}{h_x^2} + \frac{T_{i-1} - 2T_i + T_{i+1}}{h_y^2} \quad (80)$$

When applying the approximation of equation (80) to every node in the domain, a set of equations is found with the form of equation 81.

$$A\vec{T} \approx R\vec{H}S \quad (81)$$

All node temperatures are stored in vector \vec{T} . Any boundary conditions are stored in the right hand side vector $R\vec{H}S$. The boundary conditions for this problem are further discussed in section E.3. A solution for \vec{T} can be found through inversion of matrix A, as per equation (82).

$$\vec{T} = A^{-1}A\vec{T} \approx A^{-1}R\vec{H}S \quad (82)$$

Please note that matrix A stores a large number of coefficients. In order to reduce the required computational power for fine grids, a sparse A-matrix is used. A sparse matrix only stores nonzero coefficients.

E.3 Boundary conditions

Deviation from equation (80) is found for nodes on the boundary of the domain. The condition at the boundary however varies for different sections of the boundary. For a fraction of the outer evaporator wall (the right boundary of the grid in figure 61) a heater temperature or heat flux is imposed. The remainder of the right boundary is considered to be sufficiently insulated and therefore adiabatic, effectively translating into an imposed heat flux with zero magnitude. The adiabatic boundary condition is likewise applied to the top and bottom boundaries of the domain. A zero flux boundary condition for the bottom boundary is justified if the distance between the bottom boundary and any nodes with nonzero heat flux at the right boundary is sufficient. Heat is removed at the left boundary by the liquid film. As such, a convective boundary condition can be imposed on the boundary adjacent to the inner wall interface. Appropriate discretizations for all boundary condition types can be found from energy balances at the considered boundary nodes.[8]

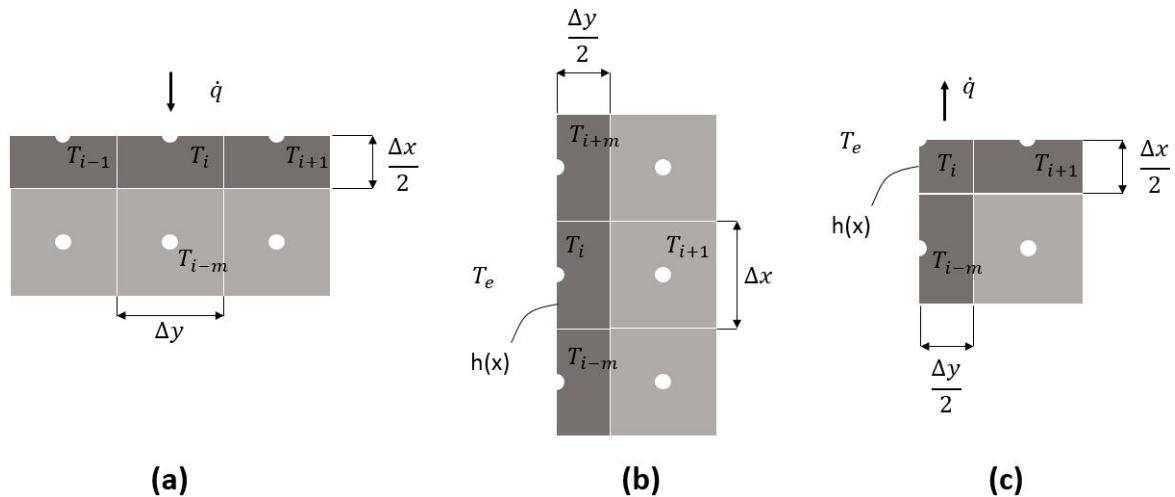


Figure 62: Schematic of three distinct boundary configurations. **(a)** top boundary, imposed heat flux \dot{q} . **(b)** left boundary, subject to convection with film at $T = T_e$. **(c)** top left corner, subject to convection with film at $T = T_e$ and imposed heat flux.

All necessary steps for finding appropriate boundary conditions can be found from the energy balances for the three distinct system boundaries depicted in figure 61. Consider the top boundary with an imposed heat flux \dot{q} as depicted in figure 62a. The energy balance from equation (83) can be rearranged to a form that can be included in matrix A and RHS, as can be seen in equation (84).

$$\begin{aligned} \dot{Q}_{\text{top,imposed}} + \dot{Q}_{\text{left,conduction}} &= \dot{Q}_{\text{right,conduction}} + \dot{Q}_{\text{bottom,conduction}} \\ \dot{q}\Delta y - k \frac{T_{i-1} - T_i}{\Delta y} \frac{\Delta x}{2} &= -k \frac{T_i - T_{i+1}}{\Delta y} \frac{\Delta x}{2} - k \frac{T_i - T_{i-m}}{\Delta x} \Delta y \end{aligned} \quad (83)$$

$$T_i \left(\frac{\Delta x}{\Delta y} + \frac{\Delta y}{\Delta x} \right) + T_{i-1} \left(\frac{-\Delta x}{2\Delta y} \right) + T_{i+1} \left(\frac{-\Delta x}{2\Delta y} \right) + T_{i-m} \left(\frac{-\Delta y}{\Delta x} \right) = \frac{\dot{q}\Delta y}{k} \quad (84)$$

Please note that for an adiabatic boundary, \dot{q} takes up a zero value. Similarly, an energy balance for the left boundary subject to convection can be found. Please note that the heat exchange at the convective boundary depends on the local heat transfer coefficient. As the heat transfer coefficient is non-constant, additional complexity is introduced. The convective boundary and the determination of the heat transfer coefficient is discussed in section E.4. The energy balance for a convective boundary in the x -direction from equation (85) (as depicted in figure 62b) reduces to the expression of equation (86).

$$-k \frac{T_{i+m} - T_i}{\Delta x} \frac{\Delta y}{2} + h_i \Delta x (T_i - T_e) = -k \frac{T_i - T_{i+1}}{\Delta y} \Delta x - k \frac{T_i - T_{i-m}}{\Delta x} \frac{\Delta y}{2} \quad (85)$$

$$T_i \left(\frac{h_i \Delta x}{k} + \frac{\Delta y}{\Delta x} + \frac{\Delta x}{\Delta y} \right) + T_{i+m} \left(\frac{-\Delta y}{2\Delta x} \right) + T_{i-m} \left(\frac{-\Delta y}{2\Delta x} \right) + T_{i+1} \left(\frac{-\Delta x}{\Delta y} \right) = \frac{h_i \Delta x}{k} T_e \quad (86)$$

The top left corner, as depicted in figure 62c, is subject to a convective boundary and an imposed heat flux $\dot{q} = 0$. The energy balance from equation (87) can be rewritten to the A-matrix coefficient form of equation (88).

$$\dot{q} \frac{\Delta y}{2} + h_i \frac{\Delta x}{2} (T_i - T_e) = -k \frac{T_i - T_{i+1}}{\Delta y} \frac{\Delta x}{2} - k \frac{T_i - T_{i-m}}{\Delta x} \frac{\Delta y}{2} \quad (87)$$

$$T_i \left(\frac{h_i \Delta x}{2k} + \frac{\Delta y}{2\Delta x} + \frac{\Delta x}{2\Delta y} \right) + T_{i+1} \left(\frac{-\Delta x}{2\Delta y} \right) + T_{i-m} \left(\frac{-\Delta y}{2\Delta x} \right) = \frac{h_i \Delta x}{2k} T_e - \frac{\dot{q}\Delta y}{2k} \quad (88)$$

With the above, all building blocks for the creation of an A-matrix and the RHS vector are present.

E.4 Convective boundary

Heat transfer coefficient h_i is non-constant along the x -direction of the mesh. Depending on the evaporation or heating regime, the value of the local heat transfer coefficient will be a function of the local Reynolds number, the local temperature difference, or the film thickness (as discussed in section 2.1). The temperature profile of the film along the evaporator wall is a function of the wall temperature and the rate of heat removal. An appropriate distribution along the evaporator wall for the heat transfer coefficient, the wall temperature and the film temperature can be found through iteration. For all even iterations, the temperature distribution of the film is updated. During uneven iterations, a new heat transfer coefficient value is found. While the relative change in total heat flow over the entire boundary remains above some user-defined threshold, the iteration process continues. An initial value is provided for the total massflow, the wall temperature and the heat transfer coefficient.

E.4.1 Temperature iteration

The film is supplied to the heated wall at some temperature $T_{e,0}$. Temperature T_e is the film temperature at the liquid-vapour interface. A value for the local T_e is stored at every node on the left boundary of the finite difference grid. In a heatpipe, as a result of interfacial heat transfer between the liquid film and the vapour annulus if a temperature gradient is present, temperature $T_{e,0}$ is close- or equal to the saturation temperature. During modeling however, any value for $T_{e,0}$ can be entered. The bulk temperature T_b is

an expression for the average film temperature, and can be found per equation (76). For this, a velocity distribution (similarly to the approach in equation (3)) is determined for every node at the left boundary using the appropriate interfacial shear at height x_i , as is discussed in section 2.1.3, and a no-slip condition at the solid-liquid interface.

The addition or removal of heat through the film can be expressed with a change in bulk temperature of the film between consecutive data points. Using the linear temperature profile assumption an expression for the local T_e can be found using the local bulk temperature and the wall temperature (the temperature at the boundary node) at local height x_i . The decision tree for finding an expression for $T_{b,i}$ along the left boundary for iteration k is depicted in figure 63.

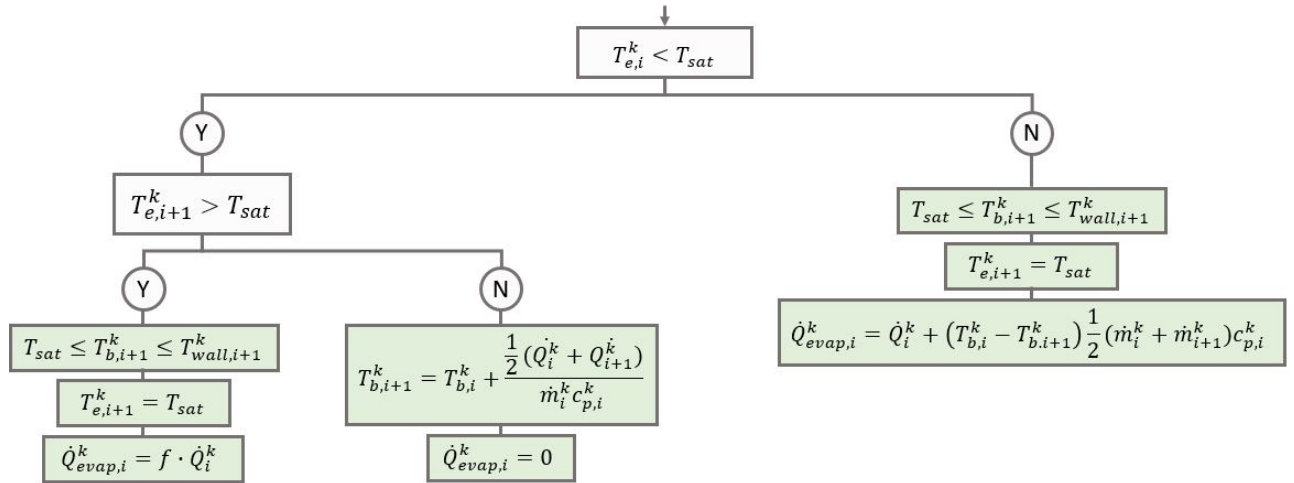
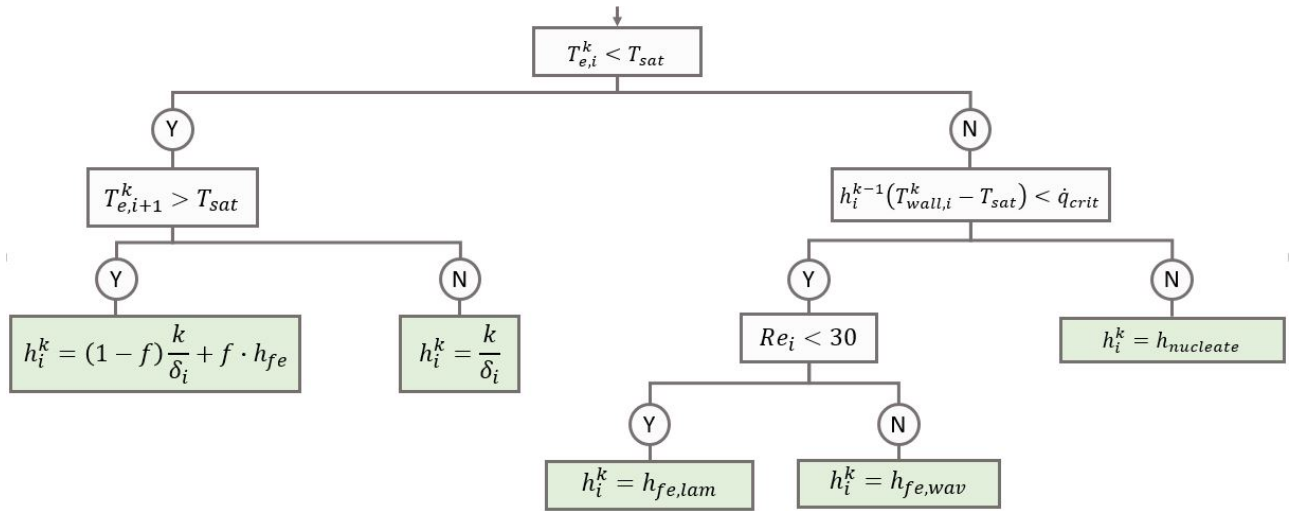


Figure 63: Expression selection for $T_{b,i}$ and $T_{e,i}$ for iteration k .

After some degree and distance of heating, T_e will attain the magnitude of the saturated temperature, and be restrained from further increasing. In the model, this is the onset node of evaporation. If the onset of evaporation is between two nodes, only some fraction f of the heat flow \dot{Q} is used to evaporate the film. The sum of evaporative heat flow \dot{Q}_{evap} can be used to determine the total massflow through the system. As liquid evaporates along the evaporator wall, the local massflow (and analogously, the Reynolds number) of both vapour and liquid decreases. The film thickness and film Reynolds number distribution along the wall can then be used to determine the heat transfer coefficient distribution in the subsequent iteration. The temperature distribution of the film is also stored and used in the following iteration of the model.

E.4.2 Heat transfer coefficient iteration

As the film temperature distribution is known from the preceding iteration, an updated expression for the heat transfer coefficients can be found using the tree depicted in figure 64.


 Figure 64: Expression selection for h_i for iteration k .

A clear distinction is made between evaporative heat transfer, and conduction to the film. As the vapour-liquid interface temperature remains at a value below the saturation temperature, heat is assumed to be added through conduction, as per equation (2). If the surface temperature is expected to surpass the saturated temperature between two respective nodes, an intermediate heat transfer coefficient (partly conduction, partly film condensation) is assumed. At nodes with saturated surface temperatures, a suitable expression for the heat transfer coefficient is chosen based on the degree of superheating. At low heat flux \dot{q} , the film condensation heat transfer coefficients discussed in section 2.1.1 will provide with agreeable results. At large heat fluxes, a nucleate boiling correlation from section 2.1.2.3 is used to approximate the heat transfer coefficient. The heat transfer coefficient distribution along the wall is stored, and used in the following iteration of the model.

E.5 Mesh sizing

An inaccurate, coarse mesh may induce errors to the solution, or prevent the model from converging. It is of importance to find a suitable minimum to the mesh fineness. A lower threshold to the resolution of nodes can be found through a mesh independence study. Here, the outcome of the model is monitored for an increasingly finer mesh. At some point, an increase in mesh refinement will no longer translate into a significant change in the outcome.

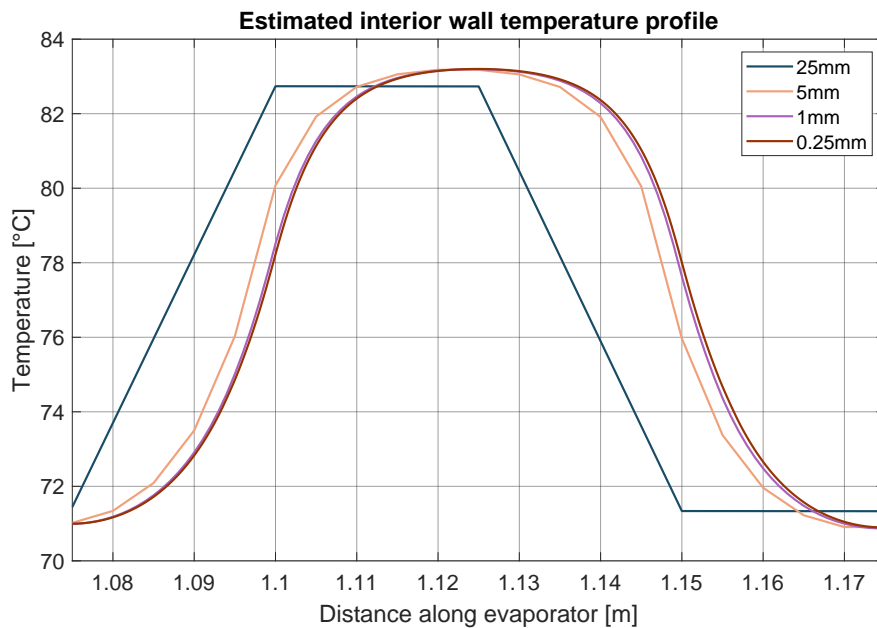
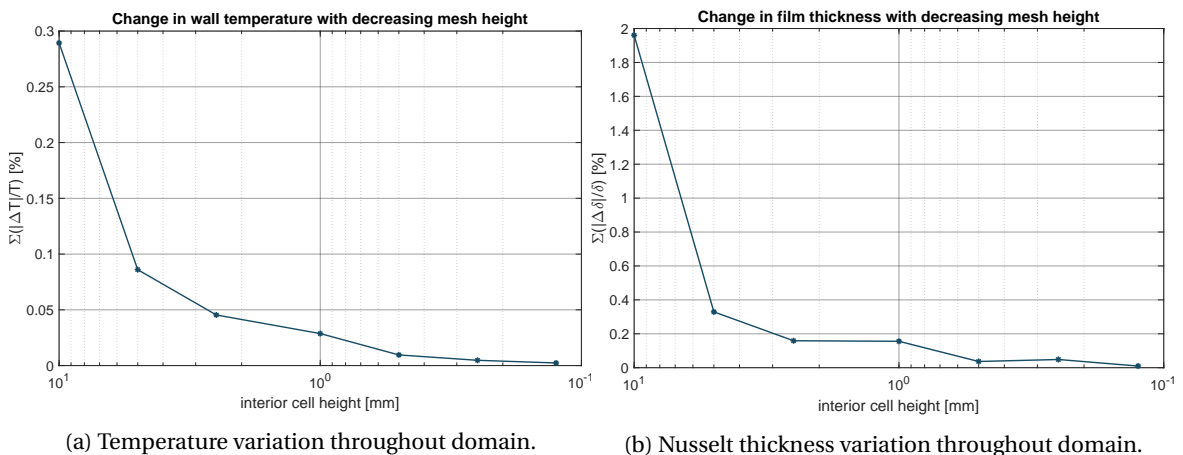


Figure 65: Estimated temperature profile at height of heater for various cell heights, $T_{\text{sat}} = 70^\circ\text{C}$, $\dot{q}_h = 1.5 \cdot 10^5 \frac{\text{W}}{\text{m}^2}$.

Figure 65 shows the estimated temperature profile at the heatpipe interior wall for a domain including a single band heater. With decreasing cell height, the temperature converges towards an increasingly true estimation. The difference between consecutive meshes however decreases with decreasing cell height. As figure 65 can solely be used for illustrative purposes, further analysis is desired. An element of comparison between respective meshes is sought after. The interior wall temperature of the heatpipe evaporator is of great importance to the heat transfer in the evaporator, and is therefore used in the comparison. The liquid film thickness along the evaporator is dependent on the temperature profile, the heat flow and the estimated heat transfer coefficient (all are variables found during modeling), and will therefore also serve as a mean of comparison between multiple meshes.



(a) Temperature variation throughout domain.

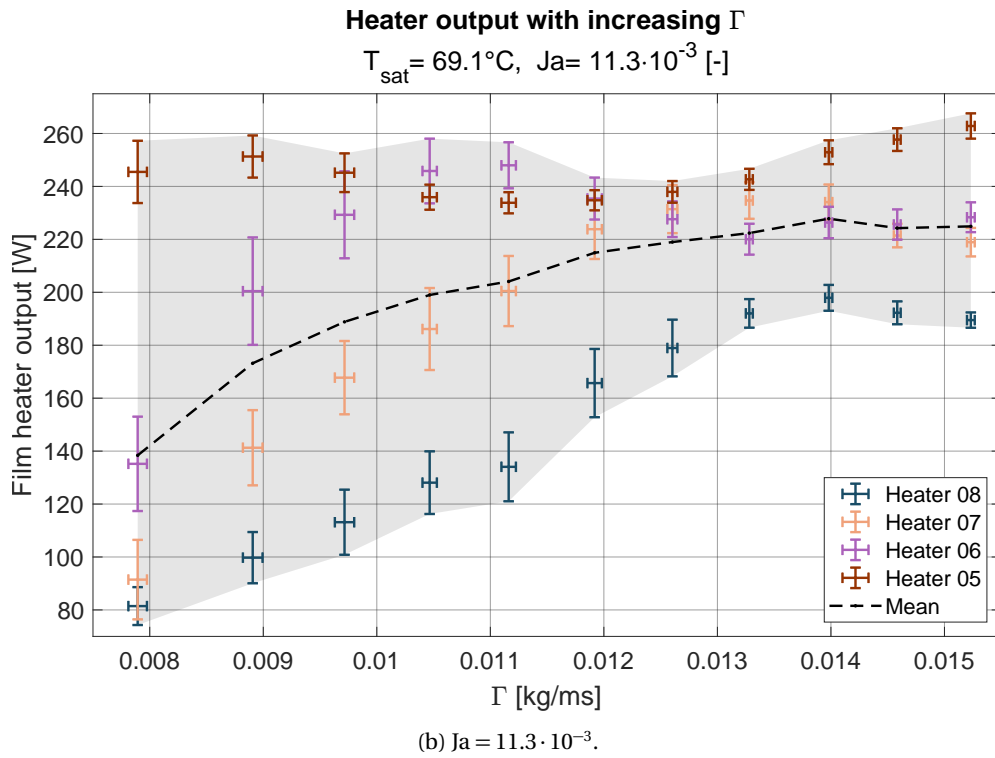
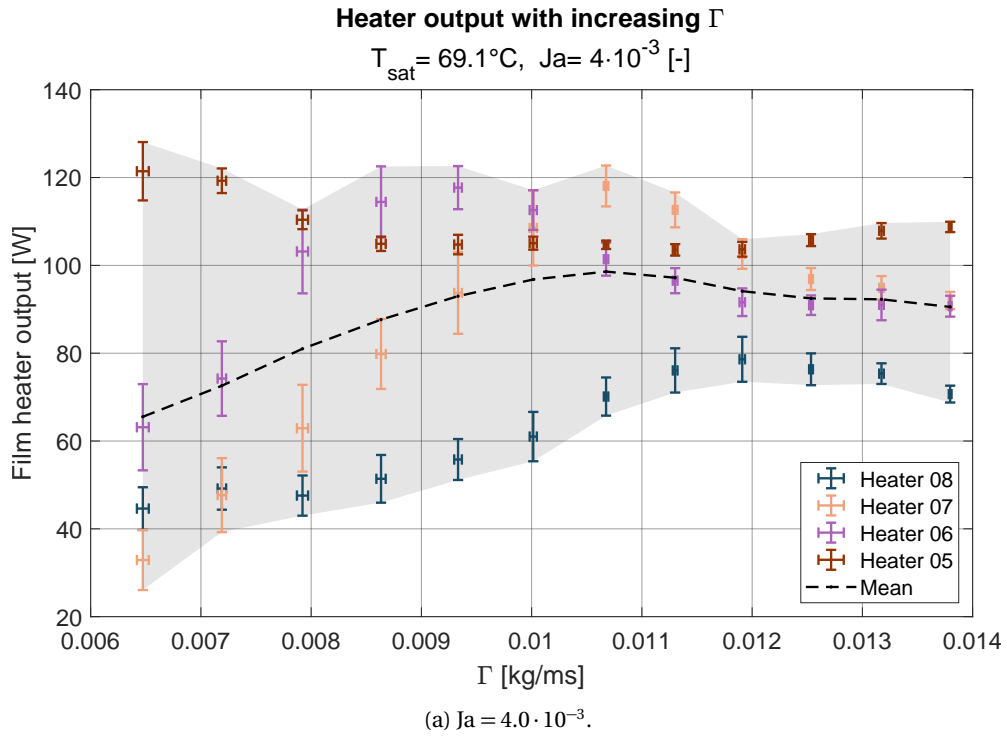
(b) Nusselt thickness variation throughout domain.

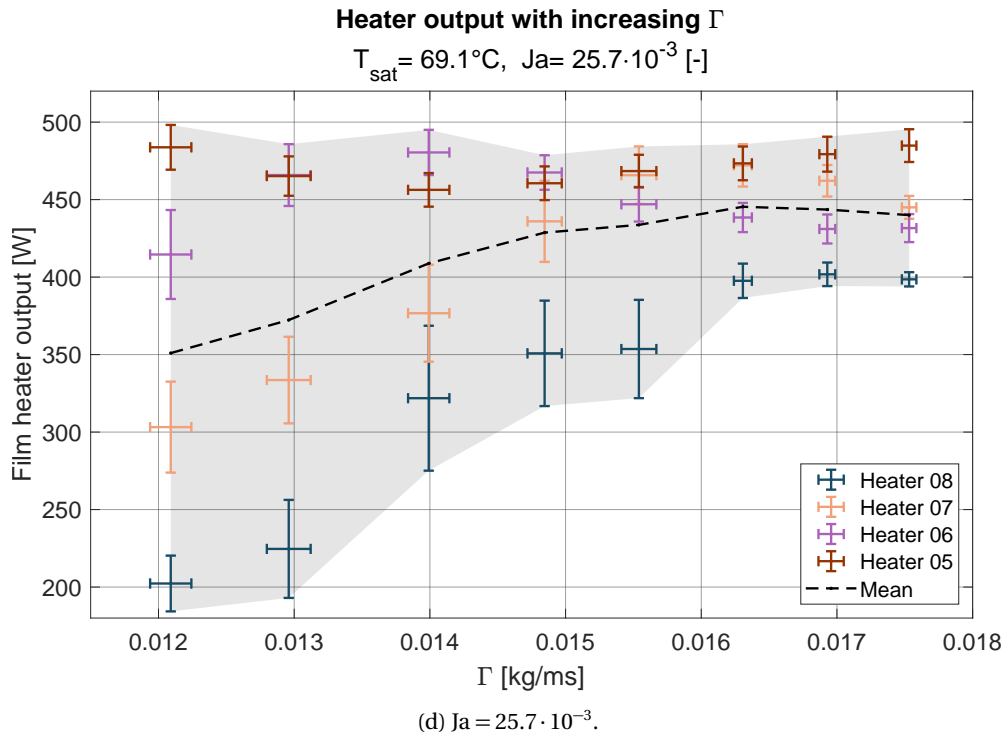
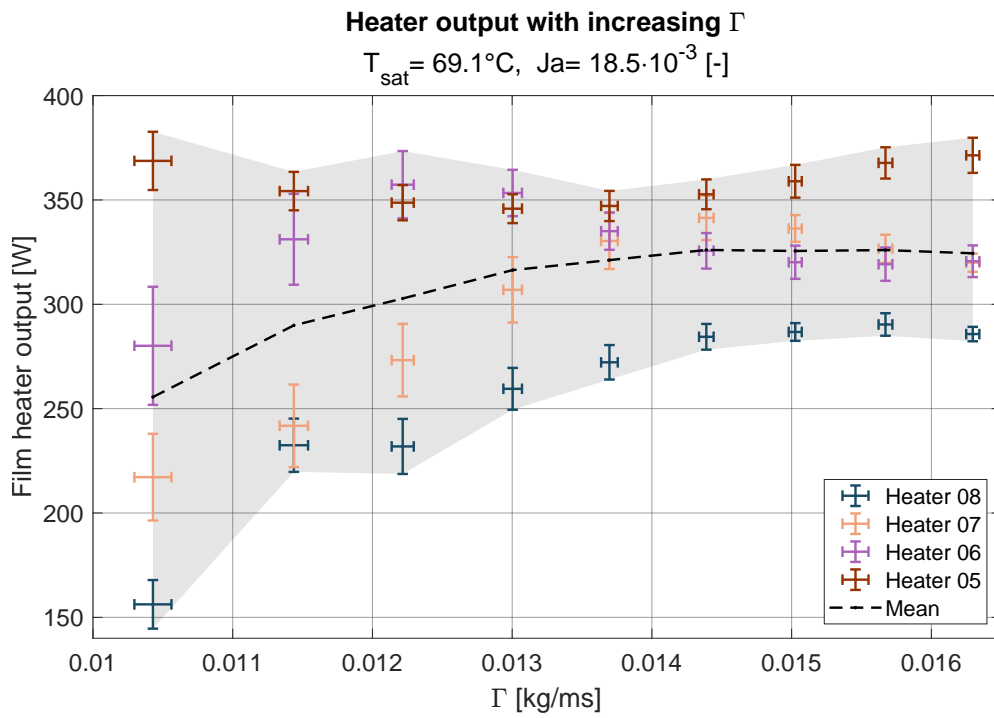
Figure 66: Evolution of variance in script output with varying mesh coarseness, with $T_{\text{sat}} = 70^\circ\text{C}$, $\dot{q}_h = 1.5 \cdot 10^5 \frac{\text{W}}{\text{m}^2}$ per heater (maximum throughput of experimental setup) and 8 heaters throughout the domain.

During the analysis, of which the results are shown in figure 66, the percentual change in temperature or thickness for all mutual data points between consecutive meshes is used to express the degree of in-

dependency of the size of the mesh. Ideally, such comparisons display asymptotic behaviour towards increasingly small meshes. With such behaviour, there is a point beyond which a further decrease in cell height yields little change in the script results. Such asymptotic trends are found and depicted in figure 66a for the temperature profile found from the script and in figure 66b for the film thickness respectively. A further decrease in cell height beyond $h_{\text{cell}} = 0.25$ mm is of little use, as the relative error found with a further increase in the mesh resolution at this cell height (0.05% for the film thickness, and 0.005% for the wall temperature) is significantly surpassed by the magnitude of any errors in the respective variables induced by modeling assumptions, as previously discussed in section E.1.

F Appendix VI: Auxiliary figures





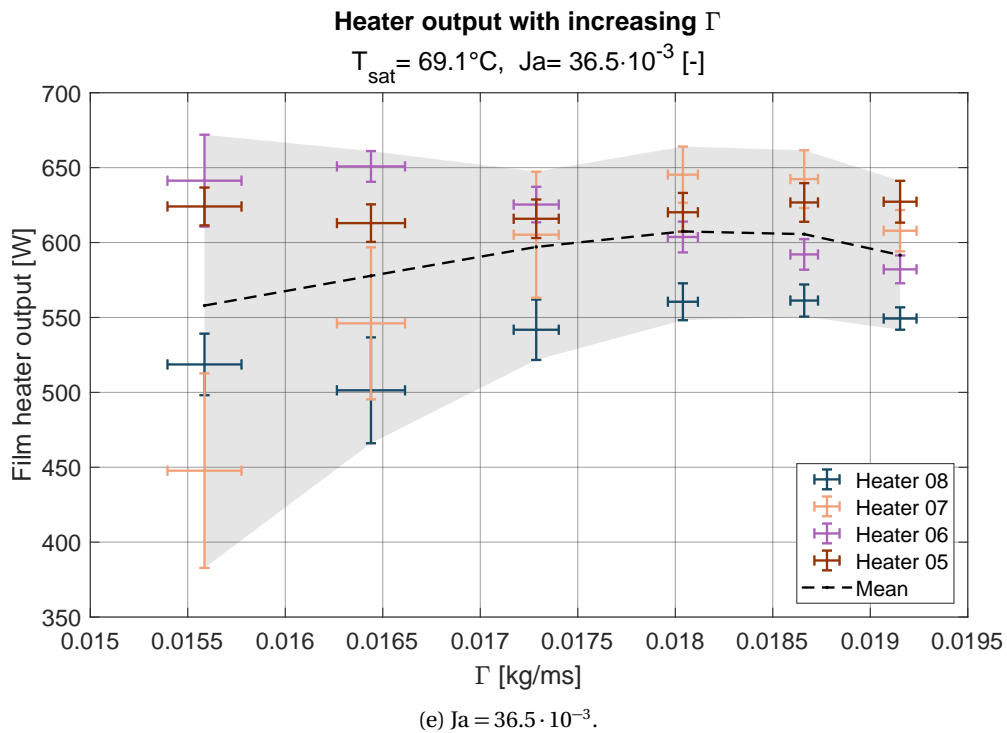


Figure 67: Film heater output at decreasing initial liquid film flow rate, for various Jakob numbers. Data shown in figure includes 68% ($t_{v,p}=1$) confidence interval. Auxiliary figure to figure 45.

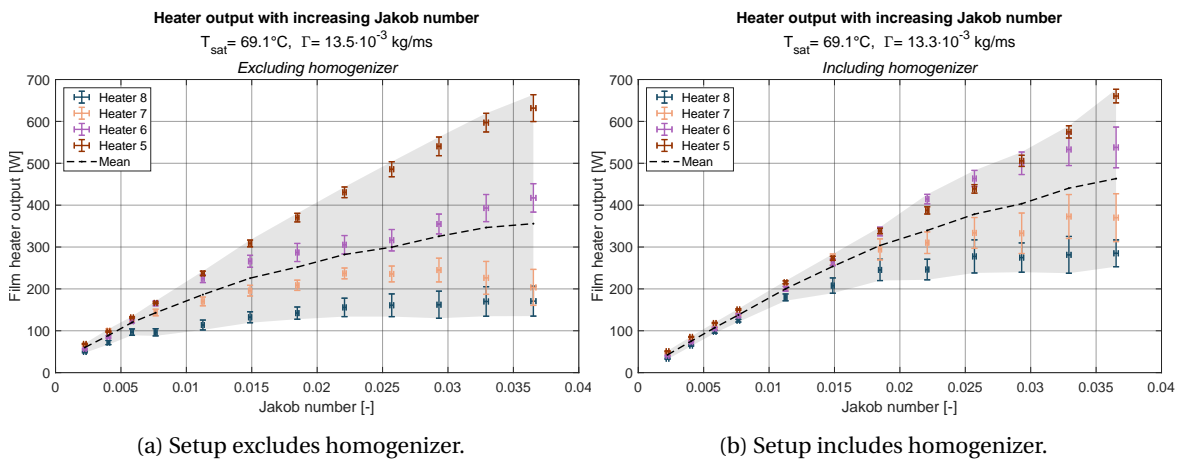


Figure 68: Comparison of heat removal rate for film heaters, as a function of the degree of superheating, expressed with the Jakob number (Ja [-]), in the absence of a homogenizer (left) with a similar set of measurements with a homogenizer (right, figure 42). Auxiliary figure to figure 54.

References

- [1] Iea, *Heat generation by source, netherlands 1990-2018*, Mar. 2020. [Online]. Available: <https://www.iea.org/data-and-statistics/?country=NETHLAND&fuel=Electricity%20and%20heat&indicator=Heat%20generation%20by%20source>.
- [2] J. Limberger, T. Boxem, M. Pluymaekers, D. Bruhn, A. Manzella, P. Calcagno, F. Beekman, S. Cloetingh, and J.-D. van Wees, “Geothermal energy in deep aquifers: A global assessment of the resource base for direct heat utilization”, *Renewable and Sustainable Energy Reviews*, vol. 82, pp. 961–975, 2018.
- [3] “Algemene voorschriften voor leidingwaterinstallaties”, Nederlands Normalisatie-instituut NEN, Nederland, Standard, 2018.
- [4] M. Pluymaekers, L. Kramers, J.-D. Van Wees, A. Kronimus, S. Nelskamp, T. Boxem, and D. Bonté, “Reservoir characterisation of aquifers for direct heat production: Methodology and screening of the potential reservoirs for the netherlands”, *Netherlands Journal of Geosciences*, vol. 91, no. 4, pp. 621–636, 2012.
- [5] D. Reay, R. McGlen, and P. Kew, *Heat pipes: theory, design and applications*. Butterworth-Heinemann, 2013.
- [6] E. W. Lemmon, I. Bell, M. L. Huber, and M. O. McLinden, *NIST Standard Reference Database 23: Reference Fluid Thermodynamic and Transport Properties-REFPROP, Version 10.0, National Institute of Standards and Technology*, 2018. DOI: <https://dx.doi.org/10.18434/T4JS3C>. [Online]. Available: <https://www.nist.gov/srd/refprop>.
- [7] M. Kind, H. Martin, P. Stephan, W. Roetzel, B. Spang, H. Müller-Steinhagen, X. Luo, M. Kleiber, R. Joh, W. Wagner, *et al.*, *VDI Heat Atlas*. Springer, 2010.
- [8] A. F. Mills, *Basic heat and mass transfer*. Prentice hall, 1999.
- [9] S. Kalliadasis, C. Ruyer-Quil, B. Scheid, and M. G. Velarde, *Falling liquid films*. Springer Science & Business Media, 2011, vol. 176.
- [10] K. Rajamani, “Interfacial profiles of wavy film flow in vertical pipe at low reynolds numbers - an experimental study”, Master’s thesis, TU Delft, Feb. 2018.
- [11] K. Chun and R. Seban, “Heat transfer to evaporating liquid films”, *Journal of heat transfer*, vol. 93, no. 4, pp. 391–396, 1971.
- [12] F. Toshihiko and U. Tatsuhiro, “Heat transfer to falling liquid films and film breakdown—ii: Saturated liquid films with nucleate boiling”, *International Journal of Heat and Mass Transfer*, vol. 21, no. 2, pp. 109–118, 1978.
- [13] F. T. Nieuwstadt, J. Westerweel, and B. J. Boersma, *Turbulence: introduction to theory and applications of turbulent flows*. Springer, 2016.
- [14] L. S. Tong, *Boiling heat transfer and two-phase flow*. Routledge, 2018.
- [15] Y. Chang, “An analysis of the critical conditions and burnout in boiling heat transfer”, *USAEC Rep. TID-14004, Washington, DC*, 1961.
- [16] P. Griffith and J. D. Wallis, “The role of surface conditions in nucleate boiling”, Cambridge, Mass.: Massachusetts Institute of Technology, Division of Industrial Cooperation, Tech. Rep., 1958.
- [17] G. Tomar, G. Biswas, A. Sharma, and A. Agrawal, “Numerical simulation of bubble growth in film boiling using a coupled level-set and volume-of-fluid method”, *Physics of Fluids*, vol. 17, no. 11, pp. 103–112, 2005.
- [18] W. Fritz and W. Ende, “Über den verdampfungsvorgang nach kinematographischen aufnahmen an dampfblasen”, *Phys. Z*, vol. 37, pp. 391–401, 1936.
- [19] K. Stephan, *Heat transfer in condensation and boiling*. Springer, 1992.

-
- [20] R. Cole and W. Rohsenow, "Correlation of bubble departure diameters for boiling of saturated liquids", in *Chem. Eng. Prog. Symp. Ser.*, 211–213, vol. 65, 1969, pp. 211–213.
- [21] N. I. Kolev, "The influence of mutual bubble interaction on the bubble departure diameter", *Experimental thermal and fluid science*, vol. 8, no. 2, pp. 167–174, 1994.
- [22] S. Hamzekhani, M. M. Falahieh, and A. Akbari, "Bubble departure diameter in nucleate pool boiling at saturation: Pure liquids and binary mixtures", *International journal of refrigeration*, vol. 46, pp. 50–58, 2014.
- [23] W. Van Helden, C. Van Der Geld, and P. Boot, "Forces on bubbles growing and detaching in flow along a vertical wall", *International journal of heat and mass transfer*, vol. 38, no. 11, pp. 2075–2088, 1995.
- [24] G. Thorncroft, J. Klausner, and R. Mei, "An experimental investigation of bubble growth and detachment in vertical upflow and downflow boiling", *International Journal of Heat and Mass Transfer*, vol. 41, no. 23, pp. 3857–3871, 1998.
- [25] J. Boulton-Stone and J. Blake, "Gas bubbles bursting at a free surface", *Journal of Fluid Mechanics*, vol. 254, pp. 437–466, 1993.
- [26] B. P. Radoev, A. D. Scheludko, and E. D. Manev, "Critical thickness of thin liquid films: Theory and experiment", *Journal of colloid and interface science*, vol. 95, no. 1, pp. 254–265, 1983.
- [27] W. M. Rohsenow, "A method of correlating heat transfer data for surface boiling of liquids", Cambridge, Mass.: MIT Division of Industrial Cooperation, [1951], Tech. Rep., 1951.
- [28] H. KUSUDA and H. IMURA, "Boiling heat transfer in an open thermosyphon: Report 1, an experiment with water", *Bulletin of JSME*, vol. 16, no. 101, pp. 1723–1733, 1973.
- [29] M. Shiraishi, K. Kikuchi, and T. Yamanishi, "Investigation of heat transfer characteristics of a two-phase closed thermosyphon", in *Advances in Heat Pipe Technology*, Elsevier, 1982, pp. 95–104.
- [30] D. Jafari, P. Di Marco, S. Filippeschi, and A. Franco, "An experimental investigation on the evaporation and condensation heat transfer of two-phase closed thermosyphons", *Experimental thermal and fluid science*, vol. 88, pp. 111–123, 2017.
- [31] P. Eisenklam, S. Arunachalam, and J. Weston, "Evaporation rates and drag resistance of burning drops", in *Symposium (International) on combustion*, Elsevier, vol. 11, 1967, pp. 715–728.
- [32] W. M. Rohsenow, J. P. Hartnett, Y. I. Cho, *et al.*, *Handbook of heat transfer*. McGraw-Hill New York, 1998, vol. 3.
- [33] P.-J. Hogendoorn, "Design and test of a heat pipe for geothermal applications", Master's thesis, TU Delft, Sep. 2019.
- [34] T. Fujita and T. Ueda, "Heat transfer to falling liquid films and film breakdown—i: Subcooled liquid films", *International Journal of Heat and Mass Transfer*, vol. 21, no. 2, pp. 97–108, 1978.
- [35] M. S. El-Genk and H. H. Saber, "Minimum thickness of a flowing down liquid film on a vertical surface", *International Journal of Heat and Mass Transfer*, vol. 44, no. 15, pp. 2809–2825, 2001.
- [36] A. Ponter, G. Davies, T. Ross, and P. Thornley, "The influence of mass transfer on liquid film breakdown", *International Journal of Heat and Mass Transfer*, vol. 10, no. 3, pp. 349–352, 1967.
- [37] S. G. Bankoff, "Minimum thickness of a draining liquid film.", Argonne National Lab., Ill., Tech. Rep., 1971.
- [38] H. H. Saber and M. S. El-Genk, "On the breakup of a thin liquid film subject to interfacial shear", *Journal of Fluid Mechanics*, vol. 500, pp. 113–133, 2004.
- [39] D. V. Zaitsev, O. A. Kabov, V. V. Cheverda, and N. S. Bufetov, "The effect of wave formation and wetting angle on the thermocapillary breakdown of a falling liquid film", *High temperature*, vol. 42, no. 3, pp. 450–456, 2004.
- [40] M. S. El-Genk and H. H. Saber, "An investigation of the breakup of an evaporating liquid film, falling down a vertical, uniformly heated wall", *J. Heat Transfer*, vol. 124, no. 1, pp. 39–50, 2002.

- [41] T. Young, "iii. an essay on the cohesion of fluids", *Philosophical transactions of the royal society of London*, no. 95, pp. 65–87, 1805.
- [42] A. Marmur, "Equilibrium contact angles: Theory and measurement", *Colloids and Surfaces A: Physicochemical and Engineering Aspects*, vol. 116, no. 1-2, pp. 55–61, 1996.
- [43] R. N. Wenzel, "Surface roughness and contact angle.", *The Journal of Physical Chemistry*, vol. 53, no. 9, pp. 1466–1467, 1949.
- [44] A. Cassie and S. Baxter, "Wettability of porous surfaces", *Transactions of the Faraday society*, vol. 40, pp. 546–551, 1944.
- [45] K. Kubiak, M. Wilson, T. Mathia, and P. Carval, "Wettability versus roughness of engineering surfaces", *Wear*, vol. 271, no. 3-4, pp. 523–528, 2011.
- [46] H. Eral, J. Oh, *et al.*, "Contact angle hysteresis: A review of fundamentals and applications", *Colloid and polymer science*, vol. 291, no. 2, pp. 247–260, 2013.
- [47] M. J. Rosen and J. T. Kunjappu, *Surfactants and interfacial phenomena*. John Wiley & Sons, 2012.
- [48] D. Brutin, *Droplet wetting and evaporation: from pure to complex fluids*. Academic Press, 2015.
- [49] G. Hewitt, "The breakdown of the liquid film in annular two-phase flow", *International Journal of Heat and Mass Transfer*, vol. 8, no. 5, pp. 781–791, 1965.
- [50] S. Whitaker, "Flow in porous media i: A theoretical derivation of darcy's law", *Transport in porous media*, vol. 1, no. 1, pp. 3–25, 1986.
- [51] D. Harleman and R. Rumer, "Longitudinal and lateral dispersion in an isotropic porous medium", *Journal of Fluid Mechanics*, vol. 16, no. 3, pp. 385–394, 1963.
- [52] A. Szymkiewicz, *Modelling water flow in unsaturated porous media: accounting for nonlinear permeability and material heterogeneity*. Springer Science & Business Media, 2012.
- [53] M. F. Ashby, H. Shercliff, and D. Cebon, *Materials: engineering, science, processing and design*. Butterworth-Heinemann, 2018.
- [54] P. Zijm, "A geothermal heatpipe prototype", Master's thesis, TU Delft, Jan. 2019.
- [55] S. G. Bankoff and S. C. Lee, "A critical review of the flooding literature", in *Multiphase Science and Technology*, Springer, 1986, pp. 95–180.
- [56] B. Azzopardi, "Drops in annular two-phase flow", *International Journal of Multiphase Flow*, vol. 23, no. 7, pp. 1–53, 1997.
- [57] T. Crawford, C. Weinberger, and J. Weisman, "Two-phase flow patterns and void fractions in downward flow part i: Steady-state flow patterns", *International journal of multiphase flow*, vol. 11, no. 6, pp. 761–782, 1985.
- [58] C. E. Brennen, *Fundamentals of multiphase flow*. Cambridge university press, 2005.
- [59] C. Park and T. Nosoko, "Three-dimensional wave dynamics on a falling film and associated mass transfer", *AIChE Journal*, vol. 49, no. 11, pp. 2715–2727, 2003.
- [60] M. Ishii and M. Grolmes, "Inception criteria for droplet entrainment in two-phase concurrent film flow", *AIChE Journal*, vol. 21, no. 2, pp. 308–318, 1975.
- [61] C. Berna, A. Escrivá, J. Muñoz-Cobo, and L. Herranz, "Review of droplet entrainment in annular flow: Interfacial waves and onset of entrainment", *Progress in Nuclear Energy*, vol. 74, pp. 14–43, 2014.
- [62] P. Nemeč, A. Čaja, and M. Malcho, "Mathematical model for heat transfer limitations of heat pipe", *Mathematical and Computer Modelling*, vol. 57, no. 1-2, pp. 126–136, 2013.
- [63] C. Busse, "Theory of the ultimate heat transfer limit of cylindrical heat pipes", *International Journal of Heat and Mass Transfer*, vol. 16, no. 1, pp. 169–186, 1973.
- [64] P. K. Kundu and I. M. Cohen, *Fluid mechanics*. Elsevier, 2001.
- [65] F. M. White, *Fluid mechanics*. Tata McGraw-Hill Education, 2010.

- [66] SpecView Ltd, *Specview version 3*, version V3, Dec. 2018. [Online]. Available: <https://www.specview.com/index.html>.
- [67] S. W. Churchill and H. H. Chu, “Correlating equations for laminar and turbulent free convection from a vertical plate”, *International journal of heat and mass transfer*, vol. 18, no. 11, pp. 1323–1329, 1975.
- [68] Ansys Granta, *Granta edupack 2019*, version 2019, Feb. 2019. [Online]. Available: <https://grantadesign.com/education/ces-edupack/>.
- [69] R. S. Figliola and D. E. Beasley, *Theory and design for mechanical measurements*. John Wiley & Sons, 2020.
- [70] D. Annaratone, *Pressure vessel design*. Springer, 2007.
- [71] D. Roylance, “Pressure vessels”, *Department of Materials Science and Engineering, Massachusetts Institute of Technology, Cambridge*, 2001.
- [72] R. Hibbeler and V. Sekar, *Mechanics of Materials*. Oct. 2013, ISBN: 9780133254426.
- [73] Q. Le, S. Ormiston, and H. Soliman, “A closed-form solution for laminar film condensation from quiescent pure vapours on curved vertical walls”, *International Journal of Heat and Mass Transfer*, vol. 73, pp. 834–838, 2014.
- [74] J. Van Kan, A. Segal, and F. Vermolen, “Numerical methods in scientific computing. department of applied mathematics”, *Delft University of Technology, The Netherlands*, 2008.